

Experimental Determination of the Free Stream
Disturbance Field in the Short Duration
Supersonic Wind Tunnel of Stuttgart University

Von der Fakultät Luft- und Raumfahrttechnik
der Universität Stuttgart
zur Erlangung der Würde eines Doktors der
Ingenieurwissenschaften (Dr.–Ing.) genehmigte Abhandlung

Vorgelegt von

Julien Weiss

geboren in Strasbourg (Frankreich)

Hauptberichter:	Prof. Dr.–Ing. S. Wagner
Mitberichter:	Prof. Dr. (Emérite) G. Comte-Bellot
Tag der mündlichen Prüfung:	21.10.2002

Institut für Aerodynamik und Gasdynamik der Universität Stuttgart
2002

Remerciements

Je remercie très sincèrement Madame Geneviève Comte-Bellot, professeur émérite à l'Ecole Centrale de Lyon, d'avoir montré un si grand intérêt pour mon travail ainsi que de m'avoir fait l'honneur de participer à mon jury de thèse.

Je remercie aussi de tout coeur mes parents, Jacqueline et Raymond Weiss, pour m'avoir encouragé à commencer ce travail de recherche, et plus généralement pour m'avoir toujours laissé la liberté de faire ce que je veux.

Danksagung

Diese Arbeit entstand am Institut für Aerodynamik und Gasdynamik der Universität Stuttgart im Rahmen des von der Deutschen Forschungsgemeinschaft geförderten Sonderforschungsbereichs 259 "Hochtemperaturprobleme rückkehrfähiger Raumtransportsysteme" im Teilprojekt C5 "Experimentelle Untersuchungen an Verdichtungsflächen und Triebwerkseinläufen für Hyperschallflugkörper".

An erster Stelle gebührt mein Dank meinem verehrten Doktorvater, Herrn Prof. Dr.-Ing. Siegfried Wagner, Leiter des Instituts für Aerodynamik und Gasdynamik der Universität Stuttgart. Am IAG hatte ich die Möglichkeit in akademischer Freiheit meine Forschungen durchzuführen. Ohne die vorgefundenen Möglichkeiten wäre meine Arbeit nicht so vielfältig und ausführlich ausgefallen.

Bei Herrn Prof. Dr.-Ing. Bernhard Weigand möchte ich mich recht herzlich für die Übernahme des Vorsitzes der mündlichen Prüfung bedanken.

Mein herzlicher Dank gilt auch Herrn Dr.-Ing. Helmut Knauss, Leiter der Abteilung Experimentelle Gasdynamik, für sein mir entgegengebrachtes Vertrauen und seine Unterstützung meiner Forschungsarbeiten.

Herrn Dr.-Ing Rudolf Riedel, meinem Vorgänger am Institut, möchte ich ganz besonders danken, für seine Hilfe zu Beginn meiner Tätigkeit und für seine konstruktiven Kommentare, die meine Arbeit erleichtert haben.

Ausserdem möchte ich mich recht herzlich bei Herrn Karl-Heinz Laicher und Herrn Manfred Giess für Ihre grosse Hilfe bedanken. Ohne Ihre Unterstützung wäre diese Arbeit nie zustande gekommen.

Herr Prof. Dr. Alexander D. Kosinov, vom ITAM in Novosibirsk, hat mich in die Geheimnisse der Hitzdrahtanemometrie eingeführt. Dafür, ebenso wie für die unzähligen Ratschläge und Hilfestellungen die er mir im Laufe der Jahre geleistet hat, möchte ich ihm danken.

Kai Augustin gilt mein besonderer Dank für seine stets freundliche Hilfe im Bereich der EDV. Durch seine Hilfsbereitschaft hat er mir diese Arbeit sehr erleichtert.

Ein herzliches Dankeschön richte ich auch an meine Kollegen aus den Abteilungen Gasdynamik und Gebäudeaerodynamik, Uwe Gaisbauer, Uwe Kaiser und Detlef Bergmann, die mich stets freundschaftlich bei meiner Arbeit unterstützten.

Für Ihre freundliche Hilfsbereitschaft und für psychologische Unterstützungen aller Art möchte ich mich auch recht herzlich bei Stanka Kokanović, Stefan Herr und Matthias Lang bedanken. Durch Ihrer Dasein war das alltägliche Leben am Institut einfach schöner, besonders Donnerstags nach Feierabend...

Schliesslich möchte ich mich bei Herrn Roland Adamek für seine Hilfe bei der Korrektur dieser Arbeit bedanken, als auch bei allen die mir während meiner Zeit am IAG behilflich waren.

Stuttgart, den 21. Oktober 2002

Julien Weiss

Contents

List of figures	5
List of tables	6
Nomenclature	7
Zusammenfassung	13
Abstract	15
1 Introduction	17
1.1 Free stream disturbances in supersonic wind tunnels	18
1.2 Measurement techniques	22
1.3 Purpose of the present work	24
2 The Shock Wind Tunnel	25
2.1 Presentation	25
2.2 Expected free stream disturbances in the SWK	30
2.2.1 Steady pressure gradients and shivering Mach waves	30
2.2.2 Vorticity and entropy mode	30
2.2.3 Fluctuating Mach waves	31
3 Experimental method	35
3.1 Introduction	35
3.2 Data reduction : the fluctuation diagram technique	37
3.2.1 Special case I: dominant acoustic mode	39

3.2.2	Special case II: uncorrelated modes	40
3.3	The Cosytec CTA Scanning System	41
3.3.1	Presentation	41
3.3.2	Overheat determination	44
3.3.3	Dynamic behaviour	47
3.3.4	Signal to noise ratio	54
3.4	Hot-wire sensor	55
3.4.1	Generalities	55
3.4.2	End-conduction effects	56
3.5	Calibration	58
3.5.1	Generalities	58
3.5.2	Accuracy	61
3.5.3	Non-linearity at low overheat ratio	64
4	Free stream disturbances in the SWK	67
4.1	Introduction	67
4.1.1	Coordinate system	67
4.1.2	Overheat steps	68
4.1.3	Usable frequency range	70
4.1.4	Measurement accuracy	72
4.2	Disturbance modes in the SWK	74
4.2.1	Experimental results	74
4.2.2	Accuracy and repeatability	76
4.2.3	Acoustic field properties	76
4.2.4	Necessary waiting time after the filling process	78
4.3	Disturbance level along the nozzle centerline	81
4.4	Power spectra	85
4.5	Possible improvement of the test section flow	87
5	Conclusion	91

<i>CONTENTS</i>	3
Bibliography	93
A Fluctuation diagram for uncorrelated modes	103
B CTA DC analysis	105

List of Figures

- 2.1 Side view of the SWK 26
- 2.2 Pressure time traces in the SWK’s test section for $Ma = 2.54$ and $R \simeq 10 \cdot 10^6/m$; (1) stagnation pressure in driver tube, (2) Pitot pressure in test section, (3) pressure in low pressure tube 27
- 2.3 Mach 2.54 nozzle contour 29
- 2.4 SWK test section, Mach 2.54 29
- 2.5 Non-dimensional power spectrum of eddy Mach wave radiation, taken from reference [57] 32
- 3.1 Cosytec CTA Scanning System (schematic) 42
- 3.2 Typical time trace of the CTA scanning system: sequence of 6 wire temperatures 43
- 3.3 CTA operating point 45
- 3.4 Underestimation of wire overheat for different offset currents; W&B refers to reference [100]. 46
- 3.5 Frequency response determination: (a) AC output voltage with electrical square-wave input; (b) AC response to one square-wave period (phase averaged from (a)); (c) bridge frequency response (FFT from (b)), inset: conventional square-wave response 50
- 3.6 Comparison between a sine wave test and the present method of frequency response determination 52
- 3.7 (a), (b) free stream disturbance power spectra for two different bridge adjustments; (c), (d) corresponding corrected spectra; inset: bridge frequency response corresponding to the adjustments in (a) and (b) . 54
- 3.8 Estimate of the signal to noise ratio (SNR) 55

3.9	Hot-wire sensor	56
3.10	Calibration in the SWK: plot of Nu versus Re^n	60
3.11	Calibration in the SWK: plots of $f(\tau)$ and $g(\tau)$	61
3.12	Calibration in the SWK: plots of F and G upon τ (Reynolds number based on wire diameter and free stream conditions)	62
3.13	Relative uncertainty of calibration coefficients F and G	63
3.14	Plot of $D(\tau)$	66
4.1	Coordinate system, $Ma = 2.54$ nozzle	68
4.2	$r = -F/G$ as a function of τ	69
4.3	Fluctuating compression waves near Mach rhombus tip	71
4.4	Fluctuation diagrams, $0.05 < \tau < 0.5$	75
4.5	Acoustic fluctuations: (a) level, (b) source velocity	77
4.6	Normalized anemometer output voltage fluctuation ($t = 0$ corresponds to the end of the filling process)	79
4.7	Time trace of the anemometer DC output voltage (t_1 : beginning of first quasi-steady state, t_2 : end of first quasi-steady state)	80
4.8	Fluctuation diagrams, $0.4 < \tau < 0.9$	82
4.9	Normalized effective static pressure fluctuation in the SWK's test section, $Ma = 2.54$; filled symbols: Cosytec bridge with scanning, $0.4 < \tau < 0.9$; open symbols: Cosytec bridge without scanning, $\tau \sim 0.9$; dotted line: see text	83
4.10	Mean static pressure disturbances in the SWK test section, taken from Riedel [78]. The numbers without prime correspond to the peaks from figure 4.9.	84
4.11	Representative power spectra, SWK's nozzle centerline	86
4.12	Estimation of the proportion of eddy Mach waves in the disturbance field	88
B.1	CTA circuit with offset current	105

List of Tables

2.1	Contraction ratio for different Mach numbers, and relation between stagnation and loading conditions for the two quasi steady states [78]	28
4.1	Summary of the fluctuation diagram's results, acoustic mode	75

Nomenclature

Latin letters

a	overheat ratio: $a = \frac{R_w - R_{20}}{R_{20}}$
$a_{balance}$	”balanced” overheat ratio: $a_{balance} = \frac{(R_w)_{balance} - R_{20}}{R_{20}}$
$a_{effective}$	effective overheat ratio
A, B	constants in the non-dimensional heat transfer law (equation 3.26)
a_0, a_1, a_2	parameters of the hyperbolic fit (section 3.2.2)
a_k	constant in the power law of $k_g(T)$
b_μ	constant in the power law of $\mu_g(T)$
B_i	Biot number
$B_e = [f_{min}, f_{max}]$	usable bandwidth
c_p	specific heat at constant pressure
c_v	specific heat at constant volume
d	hot-wire diameter
D	function of τ (equation 3.37)
D_w	thermal diffusivity of the wire material
e	anemometer output voltage
$E[...]$	mathematical expectation
f	frequency
$f_{cut-off}$	anemometer cut-off frequency
f_l	transition frequency of dynamic end-loss effects
f_1	normalized frequency (figure 2.5)
$f(\tau), g(\tau)$	parameters in the non-dimensional heat transfer law (equation 3.26)
F, G	non-dimensional anemometer calibration coefficients
F_{AC}, G_{AC}	anemometer dynamic calibration coefficients
$F[...]$	Fourier transform operator
$G_{e'}(f)$	power spectral density of $e'(t)$

$\hat{G}_{e'}(f)$	statistical estimate of $G_{e'}(f)$
h	wire heat transfer coefficient
H_B	anemometer transfer function to heat transfer input
H_E	anemometer transfer function to electrical input
j	imaginary unit
k_w	thermal conductivity of the wire material
k_g	thermal conductivity of air
k_θ	anemometer dimensional total temperature sensitivity
K_1	constant in H_B
l	hot-wire length
L, N	parameters in the dimensional wire heat transfer law
$L[\dots]$	Laplace transform operator
L_1, L_2	functions of the source velocity (Appendix A)
Ma	Mach number
n	parameter in the wire heat transfer law (equation 3.26)
Nu	Nusselt number
p	static pressure
r	$-F/G$
R	unit Reynolds number
$R_{\rho u, T_0}$	correlation coefficient between mass flow and total temperature fluctuations
Re	Reynolds number
s	Laplace variable
$S_{e'}$	finite Fourier transform of $e'(t)$
$\hat{S}_{e'}$	discrete Fourier transform of $e'(t)$
t	time
T	time span, integration time
T_L	loading temperature
T_r	hot-wire recovery temperature
T_w	hot-wire temperature
T_0	stagnation temperature
\mathbf{u}	velocity vector
u	velocity component parallel to the probe axis (x-component)
u_s	source velocity
(x, y, z)	coordinate system
x_c	x-position of the Mach rhombus tip
Z1, Z2	first and second supersonic quasi-steady states

Greek letters

α	$(1 + \frac{\gamma-1}{2}Ma^2)^{-1}$
α_R	wire temperature coefficient of resistivity
β	$\alpha(\gamma - 1)Ma^2$
χ_n^2	chi-square variable with n degrees of freedom
δ	boundary layer thickness
η	recovery factor
$\epsilon(X)$	relative uncertainty of a random variable X : $\epsilon(X) = \sigma(X)/X$
ϵ'	attenuation factor
ϵ_F	dynamic end-loss attenuation of mass flow sensitivity
ϵ_G	dynamic end-loss attenuation of total temperature sensitivity
θ	acoustic wave orientation regarding the mean flow direction (equation 3.9)
γ	c_p/c_v
μ_g	dynamic viscosity of air
ω	circular frequency
Π	$(R_a + R_w)(R_c + R_b)$
ρ	density
$\sigma(X)$	standard deviation of a random variable X
Σ	$R_a + R_b + R_c + R_w$
τ	overheat parameter: $\tau = \frac{T_w - \eta T_0}{T_0}$
τ_w	hot-wire time constant
Θ	$-\langle e \rangle / G$

Electrical parameters

D_{be}	voltage drop in the current booster
e	anemometer output voltage
e_{DC}	anemometer DC output voltage
e_{AC}	anemometer AC output voltage
e_g	input voltage perturbation for anemometer electrical test
E_{qi}	anemometer offset voltage

$G(s)$	feedback amplifier transfer function
I_{offset}, I_{off}	anemometer offset current
I_1	current flowing through the hot-wire
K	feedback amplifier DC gain
R_a, R_b, R_c	resistances in the Wheatstone bridge
R_r	hot-wire resistance at recovery temperature
R_s	input resistance for anemometer electrical test
R_T	total Wheatstone bridge resistance: $R_T = \Pi/\Sigma$
R_w	hot-wire resistance at operating point
$(R_w)_{balance}$	hot-wire resistance corresponding to a perfectly balanced Wheatstone bridge
R_{20}	hot-wire resistance at ambient temperature
\hat{R}	$R_w R_c - R_a R_b$
Z_b	compensating impedance
Z_w	impedance of hot-wire and cable

Subscripts

∞	inviscid flow
c	calibration conditions
exp	experimental
L	loading conditions
0	stagnation conditions
rot	rotational
irr	irrotational
is	isentropic
s	non-isentropic
r	recovery conditions
rms	root mean square
w	hot-wire
1, 2	first, second quasi-steady state of supersonic flow

Symbols & Superscripts

\bar{x}	temporal mean value of a fluctuating quantity x
x'	fluctuating part of x : $x' = x - \bar{x}$
$\langle x \rangle$	normalized effective value of x : $\langle x \rangle = \frac{x'_{rms}}{\bar{x}}$

Acronyms

<i>CCA</i>	constant current anemometry
<i>CTA</i>	constant temperature anemometry
<i>CVA</i>	constant voltage anemometry
<i>DFG</i>	German research foundation (German: <u>D</u> eutsche <u>F</u> orschungs <u>g</u> emeinschaft)
<i>DFT</i>	discrete Fourier transform
<i>EMS</i>	small supersonic wind tunnel at IAG (German: <u>E</u> ich <u>m</u> ess <u>s</u> trecke)
<i>EMW</i>	eddy Mach waves
<i>FFT</i>	fast Fourier transform
<i>IAG</i>	Institut für Aerodynamik und Gasdynamik, University of Stuttgart
<i>ITAM</i>	Institute of Theoretical and Applied Mechanics, Novosibirsk, Russia
<i>MSE</i>	mean square error
<i>SMW</i>	shivering Mach waves
<i>SNR</i>	signal to noise ratio
<i>SWK</i>	Shock Wind Tunnel (German: <u>S</u> toß <u>w</u> ind <u>k</u> anal)

Zusammenfassung

In der vorliegenden Arbeit wird das Störfeld in der Messkammerströmung des großen Stoßwindkanals des Instituts für Aerodynamik und Gasdynamik der Universität Stuttgart experimentell ermittelt. Das langfristige Ziel ist hierbei die Durchführung realistischer laminar-turbulenter Transitionsexperimente im Stoßwindkanal.

Diese Arbeit wurde im Rahmen des Teilprojekts C5 "Experimentelle Untersuchungen an Verdichtungsflächen und Triebwerkseinläufen für Hyperschallflugkörper" des Sonderforschungsbereiches 259 "Hochtemperaturprobleme rückkehrfähiger Raumtransportsysteme" der Deutschen Forschungsgemeinschaft durchgeführt.

Messungen werden bei einer Nenn-Machzahl von $Ma = 2.5$ mit Hilfe eines speziell entwickelten Konstant-Temperatur-Hitzdraht-Anemometers durchgeführt. Mit diesem neuen Anemometer ist eine stufenweise Änderung des Überhitzungsverhältnisses des Drahtes innerhalb einer sehr kurzen Zeit möglich, sodass die Datenauswertung mit der Modalanalyse nach Kovásnay innerhalb einer typischen Stoßwindkanal-Messzeit von $120ms$ ermöglicht wird.

Im Rahmen dieser Arbeit wird ein neues Verfahren entwickelt, um die Transferfunktion des Anemometers innerhalb sehr kurzer Zeit zu bestimmen. Die Erfassung der Transferfunktion erfolgt durch digitale Verarbeitung der Antwort des Anemometers auf ein elektrisches Signal, welches parallel zum Hitzdraht eingespeist wird. Mit Hilfe dieser Funktion wird nach dem Windkanalversuch die gemessene Anemometer-Ausgangsspannung in der Frequenzebene korrigiert, sodass eine genaue Datenauswertung fluktuierender Größen bis zur hohen Frequenzen ermöglicht wird.

Da die Empfindlichkeit des Anemometers auf Kesseltemperaturschwankungen stark von dem Überhitzungsverhältnis des Drahtes abhängig ist, wird im Rahmen dieser Arbeit der Einfluss der Anemometer Offset Spannung auf die Temperatur des Drahtes während der Auswertung berücksichtigt. Darüberhinaus zeigt eine innerhalb dieser Arbeit durchgeführte Reihenentwicklung 2. Ordnung der Kesseltemperatur-Empfindlichkeit, daß die Modalanalyse nach Kovásnay in dieser Messkammerströmung bis zu einem sehr niedrigen Überhitzungsverhältnis erlaubt ist, was die

Genauigkeit der Auswertung erhöht.

Die mit Hilfe dieses neuen und exakteren Messverfahrens gewonnene Ergebnisse zeigen, daß akustische Wellen das Fluktuationfeld in der Messkammer des Stoßwindkanals dominieren, und daß andere Fluktuationsmoden im Normalbetrieb des Windkanals vernachlässigbar sind. Diese akustischen Wellen werden von der turbulenten Grenzschicht auf die Düsenkontur und die Seitenwände des Kanals in Machscher Richtung abgestrahlt, wobei die entsprechende Schallproduktion in der Grenzschicht durch akustische Quadrupole verursacht wird. Der Verlauf der akustischen Intensität entlang der Längsachse des Kanals zeigt, daß die Grenzschicht an der Düsenkontur und an den Seitenwänden des Kanals im ganzen Bereich turbulent ist.

In Rahmen dieser Arbeit wird gezeigt, daß die Fluktuationsintensität in der Messkammer des Stoßwindkanals relativ gering im Vergleich mit anderen Überschallwindkanälen ist, und eine sehr gute Reproduzierbarkeit aufweist. Deswegen ist der Stoßwindkanal, trotz seine turbulente Düsen- und die Seitenwandgrenzschicht, eine sehr geeignetes Werkzeug, um laminar-turbulente Experimente in Überschallströmungen durchzuführen.

Abstract

The present work investigates the free stream disturbance field in the Shock Wind Tunnel (SWK), a short duration supersonic facility of the *Institut für Aerodynamik und Gasdynamik* at Stuttgart University. It takes place in the framework of the Partial Project TPC5 from the Special Research Group 259 (SFB259), established at Stuttgart University and financed by the German Research Foundation (DFG).

Measurements are performed at a nominal Mach number $Ma = 2.5$ using a specially designed constant-temperature hot-wire anemometer which enables an automatic scanning of the wire temperature in order to perform a complete modal analysis within one wind tunnel run. A new experimental procedure is developed to operate this anemometer in the SWK and, more generally, to extend the usual CTA operation in facilities with limited testing time. It is based on the post-processing of hot-wire results that are obtained with a non-optimized anemometer.

It is shown that the disturbance field is largely dominated by acoustic waves like in conventional supersonic facilities. The acoustic level is therefore repeatable from run to run, but depends on the position in the test section. Besides eddy Mach waves radiated by the turbulent boundary layer on the nozzle and the sidewalls, the disturbance field is characterized by highly localized shivering Mach waves caused by mean flow non-uniformities.

Nevertheless, due to its large size, its relative low disturbance character, and its economic mode of operation, the SWK should be remarkably advantageous for laminar-turbulent transition experiments.

Chapter 1

Introduction

Laminar-turbulent transition in high speed boundary layers remains a critical issue for the design of supersonic and hypersonic vehicles. Beside its influence on aerodynamic drag, transition plays a determinant role in heat loads and shock boundary layer interactions, which are key parameters for a successful design [96]. According to Wendt [104], the uncertainty in transition location for some classes of vehicles can lead to an uncertainty of 20% in total vehicle weight.

Despite recent progress in numerical transition prediction methods, experiments are still needed to improve and validate theoretical approaches [76]. Unfortunately, transition experiments in ground-test facilities are hindered by the high level of noise usually present in the test section, and can lead to ambiguous results when compared to free flight or numerical data [84]. It appears therefore necessary to enhance transition experiments with an experimental determination of free stream disturbances in the considered high speed facility [41].

Laminar-turbulent transition experiments are performed in the Shock Wind Tunnel (SWK) of the *Institut für Aerodynamik und Gasdynamik* (IAG) at Stuttgart University, for Mach numbers ranging from 1.7 to 4.5 [42]. Riedel [78] showed that this wind tunnel is particularly suited for such experiments, due to its good flow quality. His measurements were however restricted to the distribution of mean static pressure and dynamic Pitot pressure fluctuations on the test section centerline.

Free stream disturbances in supersonic wind tunnels consist of a superposition of three independent "modes", which can only be investigated with the help of hot-wire anemometry [65]. Moreover, the hot-wire has to be used successively at different wire temperatures in order to separate the contribution of each mode, thus making the experimental procedure rather time consuming. Until now, this prevented a thorough investigation of the disturbance field in the SWK, since its design results

in a very short testing time ($\sim 120ms$) which doesn't allow manual adjustments of commercial anemometers.

To allow full hot-wire measurements in the SWK, the design of a new constant-temperature anemometer enabling automatic rapid scanning of wire temperature has been initiated in 1997 by Knauss *et al.* [50] and a first prototype was recently manufactured in a cooperation between IAG, the company *Cosytec Elektronik GmbH* and the Institute for Theoretical and Applied Mechanics in Novosibirsk (ITAM).

The purpose of the present work is the experimental investigation of free stream disturbances in the SWK's test section using this new anemometer. This includes the development of an appropriate experimental method.

1.1 Free stream disturbances in supersonic wind tunnels

The investigation of fluctuating flows is usually made using the so-called Reynolds decomposition, which consists in separating every instantaneous basic flow variable \mathbf{u} , p , ρ , and T_0 , into a mean and a fluctuating value:

$$\begin{aligned}\mathbf{u} &= \bar{\mathbf{u}} + \mathbf{u}', \\ p &= \bar{p} + p', \\ \rho &= \bar{\rho} + \rho', \\ T_0 &= \bar{T}_0 + T_0'.\end{aligned}\tag{1.1}$$

Furthermore, the velocity fluctuations \mathbf{u}' can be split into a "rotational" part $(\mathbf{u}')_{rot}$ and an "irrotational" part $(\mathbf{u}')_{irr}$ where $rot((\mathbf{u}')_{rot}) \neq 0$ and $rot((\mathbf{u}')_{irr}) = 0$. Similarly, the stagnation temperature fluctuation T_0' can be separated into an isentropic part $(T_0')_{is}$, related to pressure fluctuations, and a non-isentropic part $(T_0')_s$.

The pioneering work of Kovásznyai [55] and Morkovin [65] showed that a turbulent field in compressible flows is composed of three fluctuating "modes" which are independent of each other when their amplitude is small. This result stems from a linearization of the Navier-Stokes equations for a compressible, viscous and heat-conductive gas, which yields the three following differential equations:

$$\begin{aligned}D(\mathbf{u}')_{rot}/Dt &= 0, \\ D(T_0')_s/Dt &= 0, \\ \frac{1}{a} \frac{D^2 p'}{Dt^2} - \nabla^2 p' &= 0.\end{aligned}\tag{1.2}$$

Since these equations are independent, they define three independent modes of fluctuations, as far as the corresponding amplitudes are small enough to allow a first order theory.

The first equation refers to the "vorticity mode", which is a variation of the rotational component of the velocity field, whereas the second one describes the "entropy mode" (also mentioned as "entropy or temperature spottiness") and refers to a variation of entropy, density and temperature at constant pressure. These two first modes can be considered as "frozen pattern" convected by the free stream ¹. The third equation is the wave equation and describes sound waves traveling within the flow (isentropic variation of pressure, density, temperature, and the irrotational part of the velocity). It corresponds to the "acoustic mode".

The amplitude of the different modes is defined as follows [43]:

- vorticity mode : $\langle |(\mathbf{u}')_{rot}| \rangle = \frac{(|(\mathbf{u}')_{rot}|)_{rms}}{|\bar{\mathbf{u}}|} = \frac{\sqrt{(\mathbf{u}')_{rot}^2}}{|\bar{\mathbf{u}}|}$,
- entropy mode : $\langle (T_0)_s \rangle = \frac{((T_0)_s)_{rms}}{\bar{T}_0} = \frac{\sqrt{(T_0)_s^2}}{\bar{T}_0}$,
- acoustic mode : $\langle p \rangle = \frac{(p')_{rms}}{\bar{p}} = \frac{\sqrt{p'^2}}{\bar{p}}$.

The free stream disturbance field in a supersonic wind tunnel consists of a contribution from each of these three modes. Since propagation mechanisms of the modes are different, the disturbances origin is different either [66, 67]: vorticity and entropy modes are convected along streamlines and must therefore be present in the flow upstream of the nozzle, whereas sound waves can spread across the streamlines and can come either from the flow upstream of the nozzle, or from the test section boundaries. Accordingly, the three turbulent modes are usually assumed to be uncorrelated in the test section of supersonic wind tunnels [55].

Vorticity and entropy modes are generally traceable to the settling chamber of conventional supersonic wind tunnels and even farther upstream. Vorticity-type disturbance modes can be minimized by a careful design of the settling chamber as well as the use of screens and meshes. Entropy fluctuations are usually minimized by a thorough design of the flow circuit and the heat exchangers. According to Schneider & Haven [83], short duration facilities have a natural low disturbance flow, due to the

¹In this simplified analysis, the diffusion time of the perturbations is supposed to be greater than the time of observation of the eddies [55].

smooth acceleration from inherently constant loading conditions. Vorticity and entropy disturbances are reminiscent of the filling process of the driver tube and should therefore be small if the air is allowed to equilibrate before each wind tunnel run. Indeed, both Wagner [94] and Bergstrom & Raghunathan [10] report a dominance of acoustic disturbances in two short duration hypersonic facilities. These results were however obtained by constructing a fluctuation diagram from data taken from different runs and can therefore be put in question, as pointed out in [10]. Indeed, residual disturbances from the filling process are unique and stochastic by nature, so that their amplitude are supposed to change slightly from run to run. Up to now, there isn't any investigation taking this effect into account.

The amplitude of acoustic disturbances in the free stream of conventional supersonic wind tunnels is usually by far the highest. Sound waves are produced by transitional and turbulent boundary layers on the nozzle and the sidewalls of the tunnel and radiated in the free stream in the form of fluctuating Mach waves. This includes the truly aerodynamic sound in the sense of Lighthill [62] produced by a distribution of quadrupoles over the turbulent boundary layer volume and referred to as "eddy Mach waves", as well as the so-called "shivering Mach waves" produced by reflection or diffraction of normally steady pressure gradients by the turbulent boundary layer.

A comprehensive study of acoustic noise in supersonic wind tunnels was made in 1961 by Laufer [56], who showed experimentally that the disturbance field in the 18×20 in. supersonic wind tunnel of the Jet Propulsion Laboratory (California Institute of Technology) was dominated by sound waves having an orientation slightly different of the Mach angle. Moreover, he showed that the turbulent boundary layers along the nozzle and the tunnel walls were responsible for this sound field. These measurements were completed afterwards by a statistical analysis of the fluctuations [58] and an attempt to compare the results with the fluctuating eddy Mach wave theory of Phillips [57, 73].

On the theoretical side, a great amount of work was published on the subject since the pioneering work of Lighthill [62, 63]. Since Lighthill's acoustic analogy was restricted to Mach numbers lower than 1, it was Phillips who first advanced a completely new formulation of the problem by deriving a wave equation in a compressible shear layer [73]. Although the solution could only be obtained for the asymptotic case of $Ma \rightarrow \infty$, this approach enabled the introduction of the important concept of "eddy Mach waves". Lighthill's acoustic analogy was somewhat later extended to high speed flows by Ffowcs Williams [26], who proved the compatibility of the concept of eddy Mach waves with Lighthill's approach. A comparison with Laufer's experimental results was then published by Ffowcs Williams & Maidanik in 1965

[27]. More information on the subject can be found in the AGARDograph 90 dedicated to the mechanisms of noise generation in the turbulent boundary layer [60] and in the bulk of published papers concerning jet noise.

Lighthill's acoustic analogy allows to identify the density fluctuations radiated by a bounded turbulent flow to those produced by a volume of acoustic quadrupoles in a uniform acoustic medium at rest [62]. It means that the acoustic field in the test section of a wind tunnel is directly related to the turbulent velocity field in the boundary layers on the nozzle and the sidewalls. The quadrupole nature of the radiation is acoustically rather inefficient due to a mutual (although not perfect) cancellation of the sources constituting it and the radiated pressure fluctuations are negligibly small in the subsonic case [72]. This situation changes dramatically at supersonic speeds, where the relative velocity of the quadrupoles with respect to the free stream is greater than the speed of sound. In this case, the mutual cancellation of waves cannot take place in the Mach direction since the waves emitted by one constituting source cannot overtake those emitted by others [26]. The radiation strength in the direction of Mach waves is thus of monopole nature and accordingly much higher than in the other directions.

The disturbance field in the tunnel free stream is therefore polluted by a strong field of eddy Mach waves produced by the turbulent boundary layer on the nozzle and the sidewalls. The wave direction is slightly different than the Mach angle in the free stream since eddies in the boundary layer are also moving with respect to the tunnel walls (that is, their velocity relative to the potential flow is smaller than the local inviscid velocity). For a free stream Mach number of $Ma = 2.5$, Laufer measured a ratio between source velocity and free stream velocity of $\overline{u_s}/\overline{u_\infty} = 0.36$ [56]².

Eddy Mach wave production is a strong function of the Mach number: Laufer experimentally found a Ma^4 variation for the acoustic intensity ($\langle p \rangle^2 \propto Ma^4$) in his wind tunnel. According to the theoretical work Phillips [73], this result reflects more precisely a Mach number effect and a boundary layer thickness effect (in the experiments of Laufer, a change of Mach number implied also a change of the nozzle boundary layer thickness). Measurements of Anders *et al.* [2] showed additionally that an increase in unit Reynolds number reduces the eddy Mach wave radiation by reducing the nozzle boundary layer thickness.

Beside eddy Mach waves, the acoustic disturbance field usually contains an important part of so-called "shivering Mach waves", which are produced by diffraction,

²It should be noted that the important parameter influencing eddy Mach wave radiation is the inviscid Mach number at the acoustic origin of the waves and not the free stream Mach number [3]. In Laufer's experiment, these two Mach numbers were very close [2].

scattering, and reflection of normally steady pressure gradients by the wall boundary layer. These mean pressure gradients can be caused by small imperfections of the nozzle contour or an insufficient surface quality. Anders *et al.* [2] indeed report a strong degree of correlation between the mean and fluctuating acoustic disturbances in two Mach 5 test sections. According to Morkovin [67], shivering Mach waves dominate in many wind tunnels and result in lower frequency fluctuations than in the case of eddy Mach waves.

Since the free stream of supersonic wind tunnels is usually polluted by a strong acoustic field, researchers have tried since the beginning of the 70-ties to build so-called "quiet wind tunnels" to be able to perform more realistic transition experiments [77, 5]. In these quiet tunnels the boundary layer on the nozzle and the sidewalls is maintained laminar as far downstream as possible to eliminate any type of fluctuating Mach wave radiation. This can however only be achieved at the expense of a relative complicated design involving boundary layer suction, straight supersonic contour, extremely high surface quality, and position dependent wall heating [5, 22, 23, 24, 18, 105, 6, 1]. A wind tunnel is considered "quiet" when the normalized RMS pressure fluctuations $\langle p \rangle$ in the test section is lower than 0.1%. This is in practice only achieved in a portion of the test section (the so-called "quiet core") which is bounded upstream by the limiting characteristic line defining the Mach rhombus and downstream by the region polluted by the turbulent nozzle boundary layer.

1.2 Measurement techniques

Development of experimental methods to determine the magnitude of the three turbulence modes was done parallel to their identification by Kovásznay [55] and Morkovin [65]. In particular, the so-called "modal analysis" or "fluctuation diagram technique", which enables the identification of different modes with a single hot-wire, was developed. This was made possible by the determination of heat loss laws in supersonic flows, as well as recent progress in electronic amplifiers which allowed measurements at high frequency [54]. An extensive investigation of free stream disturbances in the continuous supersonic wind tunnel at John Hopkins University was performed by Morkovin [66, 67], who showed, in particular, the importance of the acoustic mode and its influence on laminar-turbulent transition experiments. This dominance of acoustic disturbances was verified several years later by Laufer [56], who extended the experimental method to be able to determine the mean orientation of the waves as well as their source velocity.

As it appeared that acoustic waves form the bulk of free stream disturbances in supersonic wind tunnels, researchers began to investigate wind tunnel performance using pitot pressure probes, mainly because of their much simpler mode of operation³. Indeed, the fluctuation diagram technique requires the use of different wire temperatures to be able to separate the contribution from different modes. Moreover, the calibration procedure is rather complicated and the fragile sensor can result in a high rate of wire breakage, especially at high stagnation temperature or when dust is present in the flow. Flush mounted pressure transducers, on the contrary, are solid, easy to calibrate and operate, and benefit from a better signal to noise ratio than hot-wires. These advantages were used in a lot of quiet tunnel experiments to localize transition on the nozzle and estimate the magnitude of the acoustic disturbances [7, 6, 25, 83, 93].

Dynamic Pitot pressure measurements are however not free of drawbacks. First of all, Pitot probes are much larger than hot-wires, so that their spatial resolution is inferior. Second, although piezoresistive pressure transducers benefit from a large bandwidth, their transfer function is probe-dependent [45, 78], far from being flat, and its shape cannot be simply determined with an electrical test, as for hot-wire anemometers. Third, the relation between Pitot pressure fluctuations $\langle p_t \rangle$ and static pressure fluctuations $\langle p \rangle$ cannot be derived unless certain assumptions about the character of the flow itself are made [93, 41], so that an investigation of acoustic properties is limited. It is believed that all these drawbacks led to the probe-dependent results reported by Wolf & Laub [105] in the NASA-Ames Mach 1.6 quiet tunnel and by Knauss *et al.* [51] in the SWK at Mach 2.5. As pointed out by Stainback & Wagner [93], dynamic Pitot pressure measurements appear to be limited to qualitative indications of the acoustic disturbance level and trend in a given facility.

When an investigation of the different turbulence modes is needed, hot-wire anemometry is presently the only reliable procedure. It has to be used in combination with the fluctuation diagram technique, which enables a separation of the anemometer output voltage in different modes, provided that the hot-wire is used successively at different temperatures. In a short duration wind tunnel like the SWK, this is a rather demanding requirement since the testing time is limited to 120ms. Indeed, a full modal analysis has to be made within one wind tunnel run in order to account for the stochastic nature of the residual fluctuations in the driver tube, which are supposed to be slightly different for each run. As a consequence, measurements have to be performed with a specially designed hot-wire anemometer enabling auto-

³Dynamic Pitot probe measurements were also performed in the SWK, see Knauss *et al.* [51]

matic rapid scanning of the wire temperature, since manual adjustment is impossible within the short testing time. Although such a system has already been successfully tested by Walker *et al.* [97] in a blow-down wind tunnel (approximately 10s testing time), there is up to now no example of modal analysis performed within one run of a short duration facility.

Automatic rapid scanning of wire overheat yields new problems in the experimental procedure, the most challenging being certainly the optimization of the anemometer's frequency response. Indeed, the usual procedure is rather time consuming and particularly inadapted in short duration facilities. As will be shown in the next chapters, the philosophy adopted within this work is to work with a non-optimized anemometer, and to measure the actual frequency response in order to correct the data.

In addition, since the response of constant-temperature hot-wire anemometers to temperature fluctuations is inherently non-linear at low overheat ratios [87], particular attention will be paid to validate the results of the linear-based modal analysis.

1.3 Purpose of the present work

The present work deals with the experimental determination of the free stream disturbance field in the SWK's test section for $Ma = 2.5$ and $10 \cdot 10^6/m < R < 25 \cdot 10^6/m$ ⁴. This is made using a specially designed constant-temperature hot-wire anemometer enabling automatic rapid scanning of the wire temperature within one wind tunnel run. The two main issues are:

1. Development of a reliable procedure for a successful use of the anemometer in the SWK. In particular, a method to deal with the non-optimized frequency response and an analysis of the anemometer's linearity for temperature fluctuations are needed.
2. Actual measurement of the disturbance field. This includes the identification of the disturbance modes, an investigation of their distribution along the nozzle centerline as well as an analysis of their spectral distribution.

The next chapter introduces the main characteristics of the SWK and discuss the possible free stream disturbances using available data from the literature. Chapter 3 describes the experimental method and chapter 4 presents the results of free stream disturbance measurements.

⁴Later on, it is intended to extend this range up to $R = 50 \cdot 10^6/m$.

Chapter 2

The Shock Wind Tunnel

This chapter briefly describes the Shock Wind Tunnel with a special emphasis on the elements affecting the flow quality. A more comprehensive description can be found in references [101], [51] and [78]. The chapter will end with a discussion of the expected free stream disturbances and their possible cause.

2.1 Presentation

The IAG's Shock Wind Tunnel (German: *Stoßwindkanal*, *SWK*) is a large short duration supersonic facility designed for nominal Mach numbers ranging from 1.76 to 4.52. Because of its large rectangular test section (nozzle exit: $1.2\text{ m} \times 0.8\text{ m}$), Reynolds numbers close to original flight conditions can be simulated on large models. The driver tube supports a maximal loading pressure of 6 bar which corresponds to a maximal unit Reynolds number ranging from $R = 20 \cdot 10^6/\text{m}$ to $R = 80 \cdot 10^6/\text{m}$, depending on the Mach number.

Figure 2.1 shows a side view of the SWK. The tunnel's function principle is similar to a Ludwieg tube but a long tubing (which diameter is equal to the driver tube's one) is used on the low pressure side instead of a dump tank, in order to maximize and optimize the measuring time for different Mach numbers. After destruction of the diaphragm, the air in the driver tube is accelerated by an expansion fan and flows through the Laval nozzle, where supersonic velocity is reached. In the mean time, a shock wave travels through the low pressure part and flows back in the test section after reflexion at the tunnel wall, thus terminating the quasi steady flow. With the established ratio of pipe length, the traveling time of the waves is synchronised to allow two reflexions of the expansion fan for one reflection of the shock wave, thus

tube arrangement on high/low pressure side
for submitted experimental results

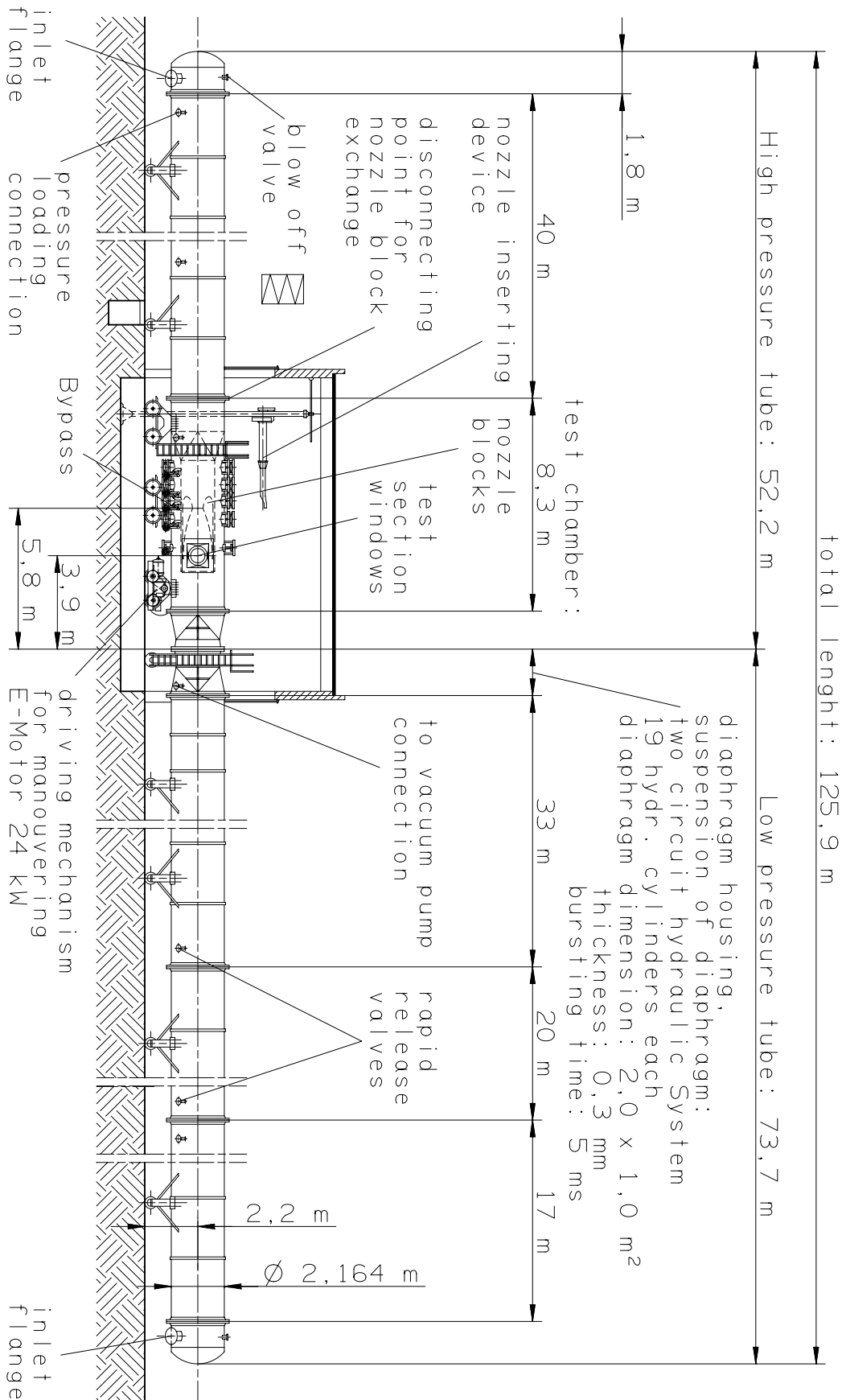


Figure 2.1: Side view of the SWK

leading to two quasi steady states of supersonic flow in the test section (Z1 and Z2), each of them during approximately 120ms. The steady flow breakdown results in very harsh flow conditions with a complicated pattern of shock reflexions in the test section. Figure 2.2 shows an example of pressure time traces in the tunnel test section and driver tube.

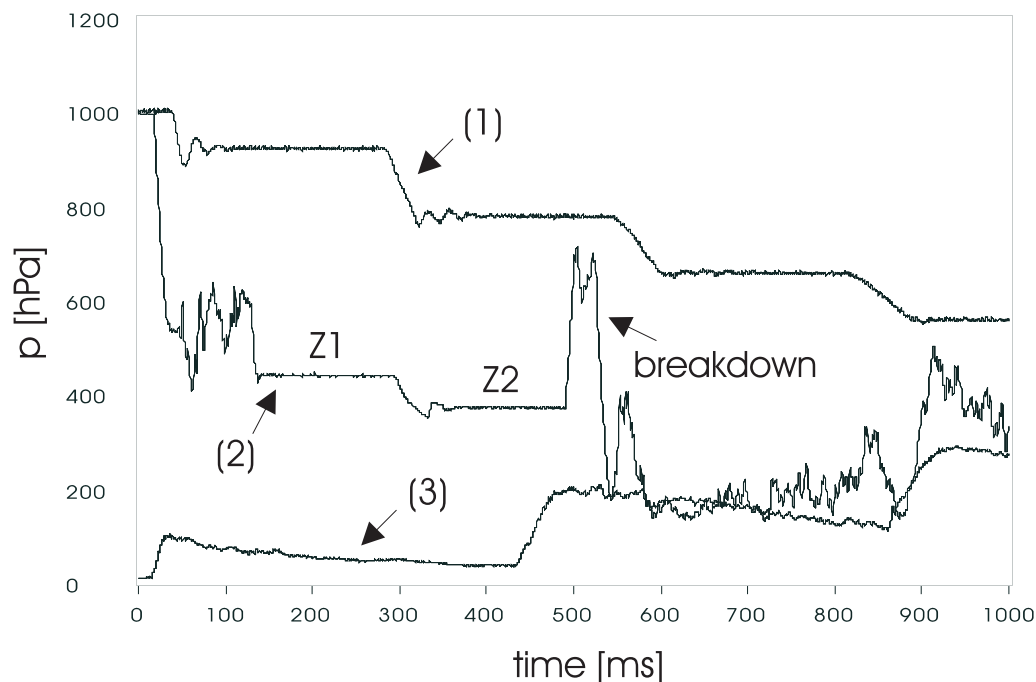


Figure 2.2: Pressure time traces in the SWK's test section for $Ma = 2.54$ and $R \simeq 10 \cdot 10^6/m$; (1) stagnation pressure in driver tube, (2) Pitot pressure in test section, (3) pressure in low pressure tube

The stagnation conditions are closely related to the loading pressure and temperature in the driver tube. Table 2.1 summarizes these relations for the four nominal Mach numbers. They are used to determine the stagnation conditions and unit Reynolds number by measurement of the loading pressure p_L and temperature T_L . The accuracy of this method has been discussed by Riedel [78].

Stationarity of the supersonic flow is very good, due to the large diameter of the driver tube, which has been designed to ensure a stagnation pressure drop of less than 1% during the whole testing time [51]. Recent hot-wire measurements showed moreover that the stagnation temperature variation within the first quasi steady state remains constant within a range of 1% [74].

Under normal operation, the loading temperature is very close to the atmosphere

Ma	A_{tube}/A_{throat}	First Steady state: Z1			Second steady state: Z2		
		$(T_0)_1/T_L$	$(p_0)_1/p_L$	$(\rho_0)_1/\rho_L$	$(T_0)_2/T_L$	$(p_0)_2/p_L$	$(\rho_0)_2/\rho_L$
1.76	5.3	0.9553	0.8532	0.8931	0.8654	0.6056	0.6998
2.54	10.0	0.9761	0.9196	0.9421	0.9283	0.7726	0.8323
3.59	28.7	0.9908	0.9685	0.9775	0.9724	0.9076	0.9333
4.52	65.0	0.9959	0.9857	0.9898	0.9876	0.9576	0.9697

Table 2.1: Contraction ratio for different Mach numbers, and relation between stagnation and loading conditions for the two quasi steady states [78]

temperature since the air in the driver tube cannot be heated. However, the filling process results in a temporary heating of the air up to over $50^\circ C$ [78]. After a cooling time of approximately 10 minutes due to heat exchanges through the tube walls, the air recovers atmosphere temperature. It is consequently possible to generate a higher stagnation temperature by performing the test just after the filling of the driver tube. In this case, an accurate control of the loading temperature is impossible and temperature stratification in the driver tube may lead to non-stationarity of the stagnation temperature. Additionally, vorticity type disturbances may be strong, due to the mechanical turbulence produced during the filling process.

To ensure a high flow quality and the absence of ice, dust and particles which may disturb the measurements or destroy fragile sensors, a high quality filter is used to fill the driver tube with dry air (according to the filter data sheet, 99.9% of particles larger than $5\mu m$ are filtered). In addition, the inner surface of the tube was recently covered with a special paint designed to support high pressure differences [42]. These measures dramatically reduced dust emission during wind tunnel runs and enabled hot-wire measurements up a unit Reynolds number of at least 25 million per meter.

Four exchangeable Laval nozzles corresponding to Mach numbers of 1.76, 2.54, 3.59, and 4.52 can be mounted in the driver tube upstream of the diaphragm housing. The two dimensional "rapid expansion nozzles" were designed by G. Schwarz in the framework of his PhD thesis [85]. Their conception includes a sharp edge, defining the throat and fixing the footpoint of the sonic line when the nozzle blocks are slightly twisted to allow a small change of the nominal Mach number, and a convex contour just downstream of the throat to erase incoming compression waves from the sonic line (see figure 2.3).

Figure 2.4 illustrates the suspension of the nozzle blocks which creates a bypass

channel between the blocks and the tunnel walls. The unsteady growing boundary layer of the driver tube is therefore peeled off and a new laminar boundary layer originates at the nozzle head. This is not the case on the sidewalls, where no bypass is present.

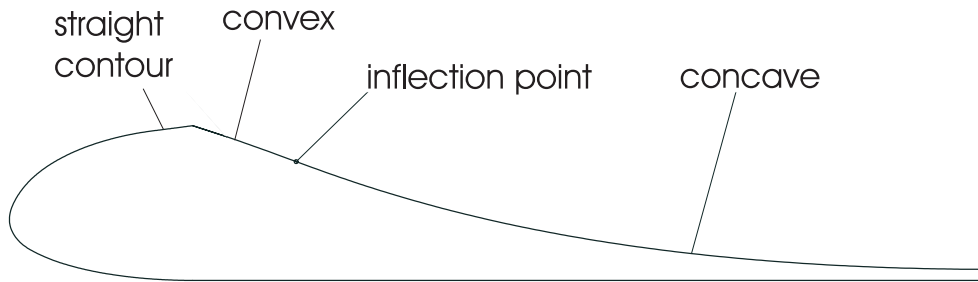


Figure 2.3: Mach 2.54 nozzle contour

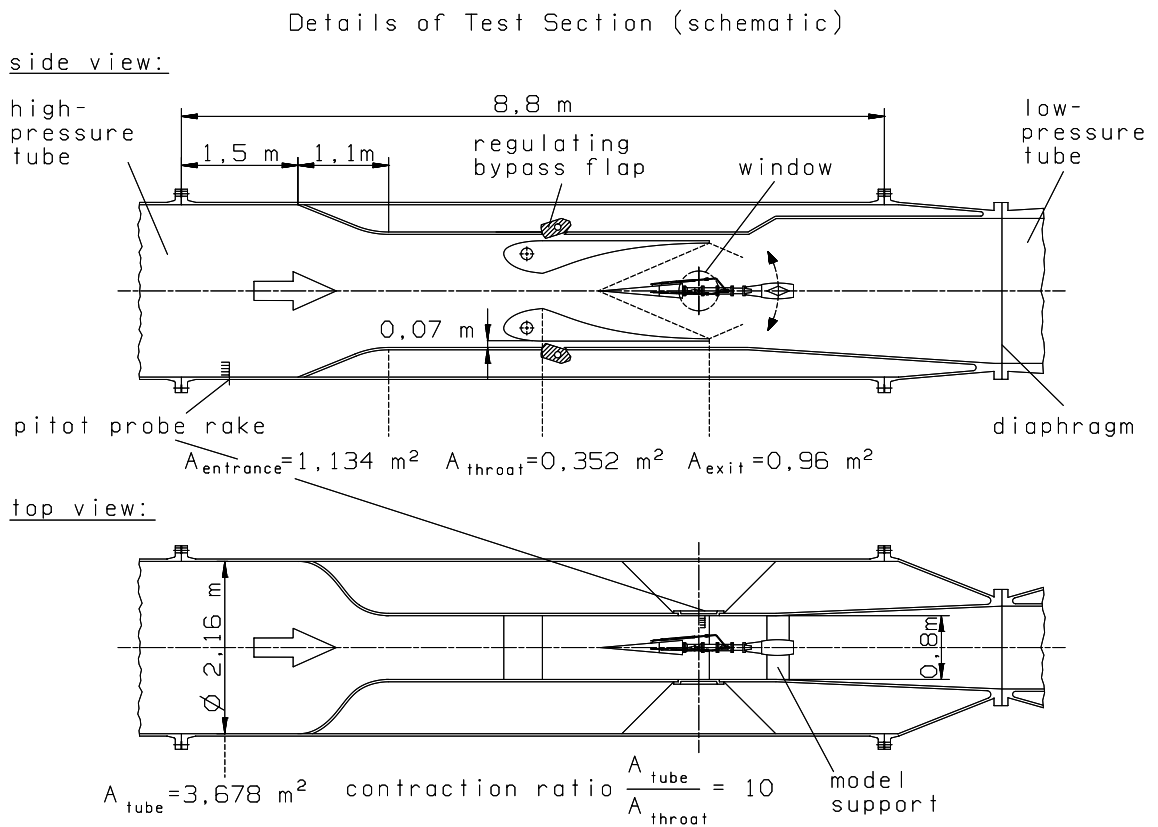


Figure 2.4: SWK test section, Mach 2.54

2.2 Expected free stream disturbances in the SWK

2.2.1 Steady pressure gradients and shivering Mach waves

Mean flow non-uniformities may be caused by imperfections of the nozzle contour as well as unsatisfactory surface quality of the nozzle and sidewalls. These imperfections result in steady compression and expansion waves running through the tunnel's test section which can be "shivered" by the wall's turbulent boundary layer.

Furthermore, some expansion waves starting at the throat cross the curved sonic line and are reflected as compression waves traveling back in the direction of the nozzle [85]. These waves are normally erased by the slightly convex contour situated just downstream of the throat, but the contour can only be designed for one Mach number, so that a slight misalignment of the nozzle can result in undesired compression waves reflected in the direction of the Mach rhombus. These waves can then converge into a weak shock at the beginning of the test section (see figure 4 of reference [85]).

2.2.2 Vorticity and entropy mode

The supersonic flow in the test section is generated by unsteady expansion in the driver tube. This is a pure isentropic process which doesn't produce any kind of disturbance. The unsteady growing boundary layer in the driver tube reaches only 2% of the diameter at the end of the quasi-steady flow, so that the core flow remains laminar during the whole testing time. As a consequence, vorticity and entropy type disturbances are reminiscent of the filling process of the driver tube, and can be minimized by allowing the air to equilibrate before each test.

A perfectly settled state of quiescence is however improbable. Irregularities in the temperature distribution may be caused by thermal convection and finite vorticity produced by the influx of compressed air may not be totally dissipated. The order of magnitude of these disturbances is unknown but data from the literature suggest that they are small compared to the acoustic field in the test section. Large scale temperature non-uniformities should scale with the driver tube diameter whereas vorticity type disturbances should have a smaller length scale, comparable to the diameter of the compressed air tubing. Additionally, high frequency entropy disturbances resulting from the turbulence dissipation process may be present.

2.2.3 Fluctuating Mach waves

Since fluctuating Mach waves of both types are mainly caused by a turbulent boundary layer on the nozzle and sidewalls, the disturbance level in the SWK strongly depends on the nature of this boundary layer (laminar or turbulent).

Boundary layer profiles at the rear part of the nozzle and the sidewalls were measured by Riedel [78] and showed a turbulent character. It remains however unclear whether these boundary layers are turbulent on the whole supersonic part of the flow, or only on a limited length, that is, whether a quiet core can be found in the test section or not. Indeed, the suspension of the nozzle blocks (figure 2.4) allows a new laminar boundary layer to start on the nozzle head and it benefits from a strong favorable pressure gradient up to the supersonic part. It can therefore be assumed to stay laminar until the nozzle throat. How long the boundary layer stays laminar on the supersonic part of the nozzle is however hard to predict, and since the boundary layer on the tunnel sidewalls is not peeled off, it is certainly turbulent in the whole test section.

The bulk of published papers on theoretical and experimental investigations on the design of quiet tunnels reveals that the laminar boundary layer on supersonic nozzles faces different instabilities, which character depends on the nozzle geometry. Whereas Tollmien-Schlichting waves are always present in the laminar boundary layer, transition on rectangular and square nozzles appears to be mainly due to crossflow instability. Alcenius *et al.* [1] showed that this type of geometry induces a crossflow in the nozzle boundary layer, due to an uneven expansion between the corners and the centerplane of the sidewalls. Görtler instabilities have also been found to be the cause of transition on concave nozzles [8], and since the boundary layer just after the throat is extremely thin, bypass transition can relative easily be caused by nozzle roughness. As already pointed out in the previous section, the SWK's nozzle is convex just downstream of the throat, but becomes concave further downstream. A portion of the nozzle is therefore free of Görtler vortices and a laminar boundary layer can possibly be found until the inflexion point. Numerical investigations of Smorodsky [90] showed indeed that transition in the boundary layer of the SWK's Mach 2.54 nozzle should be caused by Görtler vortices rather than Tollmien-Schlichting instabilities. This analysis is however only two-dimensional and doesn't take any crossflow phenomenon nor roughness elements into account. As will be shown in chapter 4, measurements performed in this work showed on the contrary that the boundary layer on the nozzle and sidewalls of the SWK is turbulent very shortly downstream of the throat.

If a turbulent boundary layer exists on the nozzle and sidewalls, an estimation of the noise level in the free stream can be made by comparison with existing data. Laufer [56] reports a normalized pressure fluctuation of approximately 0.3% in the JPL supersonic wind tunnel for $Ma = 2.5$ and $R = 13 \cdot 10^6/m$. More recently, Beckwith *et al.* [7] found a value of 0.5% in the Mach 3.5 two-dimensional pilot nozzle at NASA Langley (for $R = 31 \cdot 10^6/m$) when the boundary layer suction at the throat was not active, and Kosinov *et al.* [53] measured a normalized pressure fluctuation of 0.15% in the ITAM's T-325 wind tunnel for $Ma = 2$ and $R = 12 \cdot 10^6/m$. As will be shown in chapter 4, the noise level measured in the SWK is indeed of the same order of magnitude.

Yet an advantage of the SWK in terms of acoustic emission is its short expansion nozzle, which is better than a conventional nozzle when a turbulent boundary layer is present on its surface. According to Anders *et al.* [3], eddy Mach wave radiation is smaller in a short expansion nozzle because the Mach number and the boundary layer thickness are respectively smaller at the acoustic origin corresponding to the

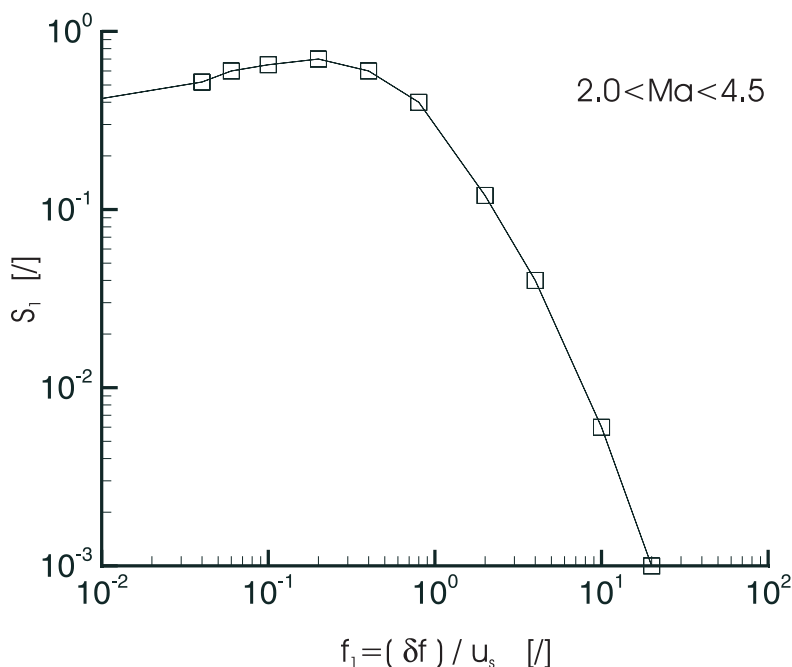


Figure 2.5: Non-dimensional power spectrum of eddy Mach wave radiation, taken from reference [57]

upstream part of the Mach rhombus.

Information about the frequency content of the eddy Mach waves can be obtained using the data of Laufer, who found a similarity of the acoustic disturbance spectrum throughout a Mach number ranging from $Ma = 2.0$ to $Ma = 4.5$ when building a normalized frequency using the nozzle boundary layer thickness δ and the source velocity \overline{u}_s of the waves [57]. This result is reproduced in figure 2.5 and shows a rapid decrease of the spectral distribution after a maximum normalized frequency of $f_1 = 2 \cdot 10^{-1}$. Using Laufer's value of $\overline{u}_s = 0.36 \cdot \overline{u_\infty}$ and a typical boundary layer thickness of $\delta = 10^{-2}m$ on the SWK's nozzle [90, 51], one finds a value of approximately $f = 4kHz$ for the peak frequency in the test section of the SWK at $Ma=2.54$.

Chapter 3

Experimental method

As already explained in the general introduction, the measurement technique chosen in the framework of this thesis is hot-wire anemometry, on the one hand because it is a relatively well known method, and on the other hand because there is up to now no other sufficiently well documented method which offers an easier mode of operation for the same precision. As will be shown in this chapter, an extension of the usual method of operation to allow measurements in a short duration wind tunnel is however necessary.

The basic results of hot-wire anemometry in supersonic flows will be reviewed in the present chapter. The "fluctuation diagram" technique will be described with regard to its use in supersonic test section flows. Since this work had to be performed with a specially designed hot-wire anemometer, a thorough description of the system and its mode of operation will follow. In particular, a method will be proposed to deal with the impossibility of *in situ* optimization of its frequency response. Finally, the last section will deal with the anemometer's calibration, with a special emphasis on low overheat ratios.

3.1 Introduction

According to the comprehensive bibliography of Freymuth [35], hot-wire anemometers have been used in the investigation of turbulent flows since the 19th century. However, it was not until the beginning of the 50ties that a successful application of this technique was made at supersonic velocities, mainly due to progress realized in the domain of electronic amplifiers [54, 19].

The heat loss law for a heated fine wire placed in a supersonic flow was first considered by Kovásznay [54] and Morkovin [65] at the John Hopkins University, and

a similar analysis was made in 1956 by Laufer & McClellan in the 20in. JPL supersonic wind tunnel [59]. Their measurements showed that for Mach numbers greater than 1.3, the Nusselt number based on the wire diameter and the flow conditions downstream of the detached shock is independent of the Mach number. In addition, for Reynolds number (based on the same conditions) greater than 20, the recovery temperature of the wire has a constant value. For $Ma \geq 1.3$ and $Re_2 \geq 20$, one can write :

$$\begin{aligned} Nu_2 &= Nu(Re_2, \tau), \\ \eta &= \text{constant}, \end{aligned} \tag{3.1}$$

where the subscript 2 refers to the stagnation conditions behind the detached shock and τ is the wire overheat parameter.

Taking into account that the wire itself is only a part of the whole anemometer, it means that for a given wire temperature, the output voltage e of a hot-wire anemometer is a function only of the mass flow ρu and the total temperature T_0 :

$$e = e(\rho u, T_0). \tag{3.2}$$

In other words, the anemometer sensitivity for density fluctuations is the same as for velocity fluctuations and it is *a priori* not possible to separate them. As will be shown in the next section, a decomposition of the anemometer fluctuating output voltage into vorticity, entropy, and acoustic modes is however possible using several assumptions. This is made using the so-called "fluctuation diagram" technique, where the hot-wire is operated successively at different temperatures.

It should be noted that the hot-wires used in this work were placed *normal* to the mean flow direction so that ρu refers to the mass flow rate *along the wind tunnel axis*. Other components of the velocity vector \mathbf{u} (which can only be measured with an inclined wire [88]) are not considered.

Different types of hot-wire anemometers are generally used by experimentalists [17, 20]. The oldest one is certainly the constant current anemometer (CCA), where the hot-wire is operated at a constant electrical current. This type of anemometer is of very simple design but requires an in-line frequency compensation module since the cut-off frequency of a heated wire reaches only several hundred Hertz, which is far too low for practical applications. Details concerning the use of CCA in supersonic turbulent flows can be found in [44], [43], and [4]. In subsonic flows, the CCA is still preferred for measuring temperature fluctuations but has been largely superseded by the constant temperature anemometer (CTA) for velocity fluctuations, mainly because of its easier method of operation. In a CTA, the wire is maintained at

a constant temperature by the use of a feedback loop. The frequency response is therefore automatically compensated by the feedback circuit and can reach several hundred kilohertz [28]. In supersonic flows, the two systems are still widely used, due to a major drawback of the CTA: its non-linearity to temperature fluctuations at low wire temperature [86, 87]. A third type of anemometer, the constant voltage anemometer (CVA), has recently emerged [81], although a first discussion of this operating mode dates back to 1966 [29]. In this system, the hot-wire is maintained at a constant voltage in the feedback loop of an operational amplifier. This method was recently compared to a CTA [47, 48] and showed promising results when tested in supersonic flows [82, 21]. A comparison of sensitivity coefficients for the three type of anemometers can be found in [61].

For measurements in a short duration wind tunnel, both CCA and CVA have a major drawback: their operating point (*ie* the hot-wire temperature) depends on the flow conditions. It means that an accurate *in situ* adjustment of the wire overheat parameter is impossible because of too short a testing time. The in-line frequency compensation module (which is necessary for both type of anemometers) cannot be perfectly adjusted because its cut-off frequency should match the wire thermal frequency, which itself depends on the wire temperature. Moreover, the usual calibration procedure, which requires a variation of mass flow at a constant overheat, cannot be performed.

For those reasons, measurements performed within this work were made with a specially designed CTA. With such a system, the wire temperature can be adjusted before the test and remains approximately constant when the wire is placed in the flow. It remained however necessary to cope with problems of non-optimized frequency response (section 3.3.3) and low-overheat non-linearity (section 3.5.3) before this anemometer could be used quantitatively in the SWK, given the inherent limitations of the wind tunnel regarding the available testing time.

3.2 Data reduction : the fluctuation diagram technique

This section introduces the "fluctuation diagram" technique which was originally developed by Kováshay [55] and Morkovin [65] to determine experimentally the amplitude of the different turbulence modes in compressible flows. The following analysis is restricted to supersonic flows ($Ma > 1.3$) where equation 3.2 is valid.

A more general review of the method including recent references can be found in [43, 92].

As already explained in the last section, at sufficiently high Mach and Reynolds numbers, the output voltage e of a hot-wire anemometer is only a function of the mass flow ρu and the total temperature T_0 of the flow: $e = e(\rho u, T_0)$. Performing the logarithmic differentiation of this equation leads to:

$$\frac{de}{e} = F \frac{d(\rho u)}{\rho u} + G \frac{d(T_0)}{T_0}, \quad (3.3)$$

where $F = d(\ln(e))/d(\ln(\rho u))$ and $G = d(\ln(e))/d(\ln(T_0))$.

Kovácsznay [55] and Morkovin [65] performed the so-called "local linearization method" and identified each differential as the instantaneous deviation of a fluctuating quantity with reference to its temporal mean value ¹. Writing

$$\begin{aligned} e &= \bar{e} + e', \\ \rho u &= \overline{\rho u} + (\rho u)', \\ T_0 &= \overline{T_0} + T_0', \end{aligned} \quad (3.4)$$

equation 3.3 is then equivalent to

$$\frac{e'}{\bar{e}} = F \frac{(\rho u)'}{\overline{\rho u}} + G \frac{T_0'}{\overline{T_0}}, \quad (3.5)$$

where F and G are respectively the mass flow and total temperature sensitivities of the anemometer and have to be obtained by calibration. F and G are function of the overheat parameter τ of the wire.

In practice, equation 3.5 has to be squared and averaged to correspond to the experimental situation. This gives:

$$\boxed{\Theta^2 = \langle \rho u \rangle^2 r^2 - 2R_{\rho u, T_0} \langle \rho u \rangle \langle T_0 \rangle r + \langle T_0 \rangle^2}, \quad (3.6)$$

where the following quantities were introduced:

$$\Theta = - \langle e \rangle / G, \quad \langle e \rangle = \frac{e'_{rms}}{\bar{e}}, \quad \langle \rho u \rangle = \frac{(\rho u)'_{rms}}{\overline{\rho u}}, \quad \langle T_0 \rangle = \frac{(T_0)'_{rms}}{\overline{T_0}}, \quad r = -F/G,$$

$$\text{and } R_{\rho u, T_0} = \frac{\overline{(\rho u)' T_0'}}{(\rho u)'_{rms} (T_0)'_{rms}}.$$

Hence, if the sensitivities F and G are known, then for each measurement of $\langle e \rangle$ there are three unknown quantities: $\langle \rho u \rangle$, $\langle T_0 \rangle$, and $R_{\rho u, T_0}$. Theoretically, since F and G are functions of τ , these quantities can be determined by measuring

¹The turbulent flow under investigation is modeled as a *stationary* random process.

$\langle e \rangle$ at three different wire overheat and solving the three simultaneous equations for the unknowns. In practice, however, accurate results are difficult to obtain because of experimental uncertainties and it is preferred to plot Θ for many values of r . The unknown quantities are then obtained by a numerical curve fitting of the corresponding diagram.

In the general case, the function $\Theta(r)$ is a hyperbola which coefficients are functions of the three unknowns. In practice, the unknowns can be easily obtained by fitting $\Theta^2(r)$ with a second order polynomial function and by taking the resulting positive square root to draw $\Theta(r)$. If the uncertainty of the measured values of Θ is estimated, the fitting algorithm (general least squares method) also provides an uncertainty estimate for $\langle \rho u \rangle$, $\langle T_0 \rangle$ and $R_{\rho u, T_0}$ [91].

It is important to notice that a usual fluctuation diagram enables only the evaluation of the normalized mass flow fluctuation $\langle \rho u \rangle$, the normalized total temperature fluctuation $\langle T_0 \rangle$, and their correlation coefficient $R_{\rho u, T_0}$. A further splitting of the data to obtain the magnitude of the three turbulence modes (vorticity, entropy, and acoustic mode) requires new assumptions which depend on the flow conditions. For example, in supersonic boundary layers, the contribution of the acoustic mode is often neglected and the "strong Reynolds analogy" is invoked [43]. For the flow in the free stream of supersonic wind tunnels, two other special cases are of interest and should now be introduced in more details.

3.2.1 Special case I: dominant acoustic mode

When the disturbance field is a pure acoustic field, Laufer [56] showed that the correlation coefficient $R_{\rho u, T_0}$ is equal to -1 . In this case, equation 3.6 simplifies to

$$\Theta = \langle \rho u \rangle r + \langle T_0 \rangle, \quad (3.7)$$

and the fluctuation diagram $\Theta(r)$ reduces to a straight line. Moreover, the following relations between the normalized pressure and velocity fluctuations are valid ²:

$$\begin{aligned} \langle \rho u \rangle &= \frac{1}{\gamma} \langle p \rangle - \langle u \rangle, \\ \langle T_0 \rangle &= \alpha(\gamma - 1) \left(Ma^2 \langle u \rangle - \frac{1}{\gamma} \langle p \rangle \right). \end{aligned} \quad (3.8)$$

In practice, when a linear fluctuation diagram is obtained by measurements, $\langle \rho u \rangle$ and $\langle T_0 \rangle$ can easily be obtained by fitting the data to a straight line and $\langle p \rangle$ can

²In this case of a pure acoustic field, $\langle u \rangle$ and $\langle T_0 \rangle$ are respectively equal to the irrotational velocity fluctuation $\langle (u)_{irr} \rangle$ and the isentropic total temperature fluctuation $\langle (T_0)_{is} \rangle$ since both vorticity and entropy modes are neglected.

then be computed using 3.8. When the acoustic sources are stationary with respect to the wind tunnel (shivering Mach waves), $\langle T_0 \rangle = 0$ and the straight line passes through the origin. On the other hand, when the acoustic sources are convected downstream, $\langle T_0 \rangle \neq 0$ and it is possible to calculate the mean propagation velocity $\overline{u_s}$ of the sources and the most probable wave orientation θ using the following relation³:

$$\frac{\overline{u_s}}{u_\infty} = 1 + \frac{1}{Ma \cdot \cos\theta} = 1 - \frac{\langle p \rangle}{\gamma Ma^2 \langle u \rangle}. \quad (3.9)$$

3.2.2 Special case II: uncorrelated modes

As pointed out by Morkovin [67], the fluctuation field in the free stream of supersonic wind tunnels is *a priori* composed of comparable contributions of the three turbulence modes so that the assumption of a dominant sound field is not always possible. If one assumes that the three different modes are uncorrelated, it is however possible to extract their magnitude from the fluctuation diagram. Kovásznyai [55] proposed this assumption to measure the residual fluctuations in supersonic wind tunnels and derived a relation between Θ^2 , r and the three turbulence modes for the case of fluctuating Mach waves with stationary sources. As shown in Appendix A, this relation can easily be extended to Mach waves with arbitrary orientation provided that the source velocity $\overline{u_s}$ is known. This extended relation reads:

$$\Theta^2 = (L_1 r + L_2) \langle p \rangle^2 + (\beta - r)^2 \langle u_{rot} \rangle^2 + \left(1 + \frac{r}{\alpha}\right)^2 \langle (T_0)_s \rangle^2, \quad (3.10)$$

where $\langle u_{rot} \rangle$ refers to the rotational velocity fluctuations and $\langle (T_0)_s \rangle$ to the non-isentropic total temperature fluctuations. L_1 and L_2 are function of the source velocity $\overline{u_s}$ and are defined in Appendix A.

In practice, a set of N measured values of $(\Theta^2, r)_{i,1 \leq i \leq N}$ can be fitted to a second order polynomial function of the following type:

$$\Theta^2 = a_0 + a_1 r + a_2 r^2, \quad (3.11)$$

where a_0 , a_1 , and a_2 are the results of the general least squares algorithm. The positive square root of 3.11 is then a representation of the fluctuation diagram.

The three unknowns $\langle p \rangle$, $\langle u_{rot} \rangle$, and $\langle (T_0)_s \rangle$ are solution of the following

³When entropy spottiness is the dominant disturbance mode, the fluctuation diagram is also linear. In this case the straight line has to go trough the point $(-\alpha, 0)$ so that it is in practice easy to discriminate between dominant acoustic and entropy mode [55].

system, which can be obtained by writing the equivalence of equations 3.10 and 3.11:

$$\begin{pmatrix} a_2 \\ a_1 \\ a_0 \end{pmatrix} = A \begin{pmatrix} \langle p \rangle^2 \\ \langle u_{rot} \rangle^2 \\ \langle (T_0)_s \rangle^2 \end{pmatrix}, \quad (3.12)$$

where

$$A = (a_{ij}) = \begin{pmatrix} L_1^2 & 1 & 1/\alpha^2 \\ 2L_1L_2 & -2\beta & 2/\alpha \\ L_2^2 & \beta^2 & 1 \end{pmatrix}. \quad (3.13)$$

When an uncertainty estimate of the N measured values of $(\Theta)_i$ in the form of a standard deviation $(\sigma(\Theta))_i$ is known, the least squares algorithm provides the uncertainty $\sigma(a_0)$, $\sigma(a_1)$, and $\sigma(a_2)$ of the three parameters. The uncertainties $\sigma(\langle p \rangle)$, $\sigma(\langle u_{rot} \rangle)$, and $\sigma(\langle (T_0)_s \rangle)$ of the three unknowns can then be computed using the following relation, which was derived using the usual law of random error propagation [75]:

$$\begin{pmatrix} \sigma^2(\langle p \rangle^2) \\ \sigma^2(\langle u_{rot} \rangle^2) \\ \sigma^2(\langle (T_0)_s \rangle^2) \end{pmatrix} = B \begin{pmatrix} \sigma^2(a_2) \\ \sigma^2(a_1) \\ \sigma^2(a_0) \end{pmatrix}, \quad (3.14)$$

where $B = (b_{ij}) = (c_{ij}^2)$, and $(c_{ij}) = C = A^{-1}$.

3.3 The Cosytec CTA Scanning System

This section describes the CTA which was specially designed for measuring the disturbance field in the SWK's test section. After a general presentation, the method used to determine the bridge operating point will be presented. In particular, it will be shown that the bridge offset current, which is often neglected, is an important parameter for an accurate estimation of the wire overheat parameter. The next section will deal with the anemometer's frequency response and a very fast method to compute the anemometer's transfer function will be presented. A consideration of the system's signal to noise ratio will follow.

3.3.1 Presentation

Figure 3.1 shows a schematic diagram of the anemometer, which was built in a cooperation between IAG, ITAM, and the German company *Cosytec Elektronik GmbH*. It

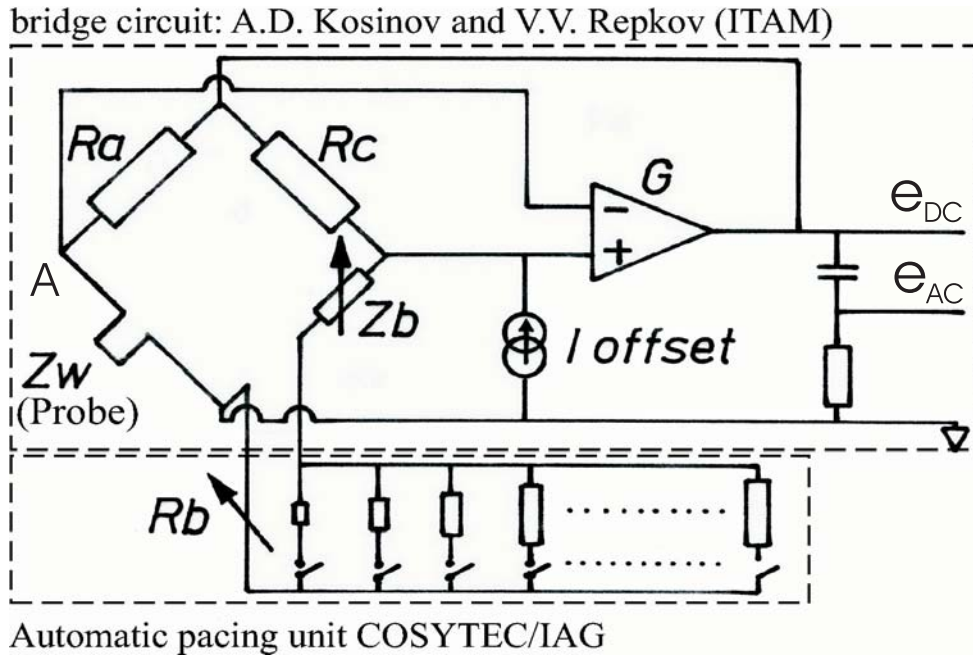


Figure 3.1: Cosytec CTA Scanning System (schematic)

consists of two units: a CTA feedback circuit (originally designed by A. D. Kosinov and V. V. Repkov [52]), and an automatic scanning unit (Cosytec). The CTA circuit is a 1:10 bridge that enables a 3-parameter optimization of the frequency response: impedance Z_b in the passive arm of the bridge, offset current I_{offset} , and amplifier gain G ⁴. The wire temperature can be adjusted by varying the resistance R_b in the passive arm of the bridge, which consists of a series of resistances connected together with reed relays and forming the automatic scanning unit. It enables a rapid change of overheat in a very short time. The logic of the system allows the setting of maximum 10 wire temperatures in one test sequence. The maximum overall time of a sequence is 2.5s and the temporal resolution of the system for the time adjustment is 1ms per step [40, 103].

To ensure that its fluctuating part is measured with enough accuracy, the output voltage is AC-coupled with a high pass filter of 1kHz cut-off frequency. Figure 3.2 shows a typical time trace of the bridge output. Six overheat ratios ranging from $a = 0.9$ to $a = 0.4$ are scanned in a total time of 120ms. A critical point connected with the use of such a bridge is the time needed to attain equilibrium after a change

⁴It should be noted that although 3 electrical parameters can be varied in the anemometer, it corresponds in reality to a two parameters optimization of the feedback system since it can be described by a third order function [38].

of wire temperature. This time delay is *a priori* function of the thermal capacity of the sensor, the system's frequency response and the rapidity of the electrical connections in the scanning device. Investigations showed that the equilibrium type depends mainly on the electrical connections and is approximately $2 - 3ms$ for a typical $5\mu m$ hot-wire. However, a strong electrical oscillation has sometimes been observed for several overheat combinations and demands a longer settling time. This phenomenon is caused by very fast oscillations of the electrical connections in the passive arm of the bridge when the resistance ratio is changed (see reference [103]).

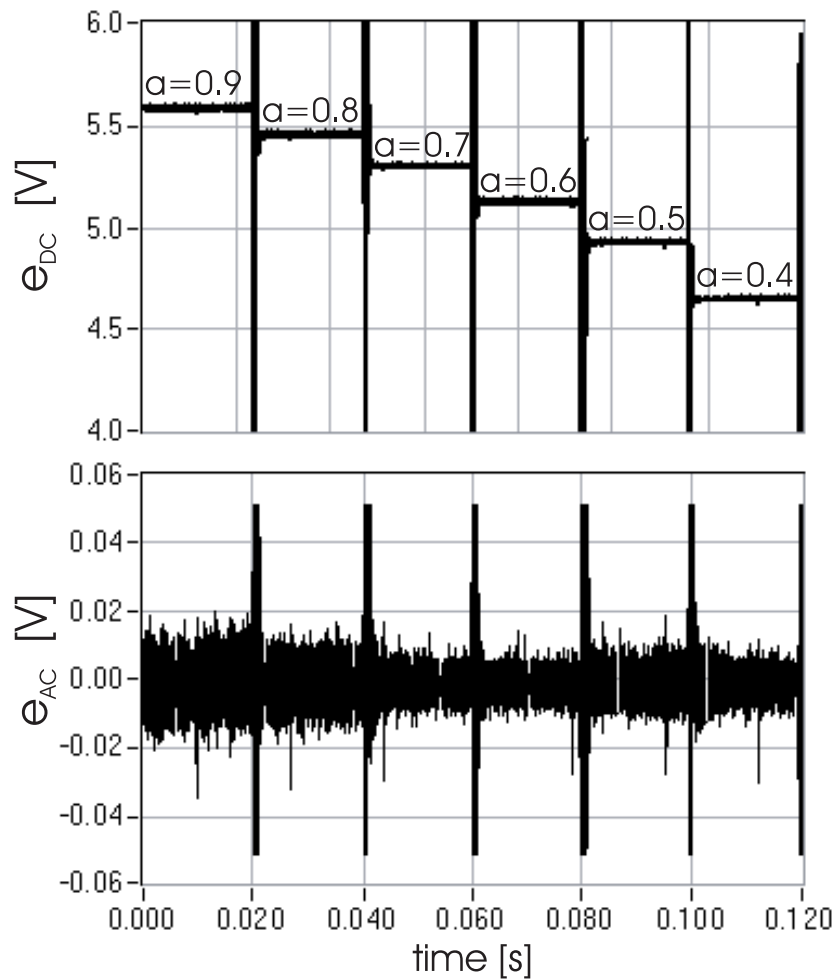


Figure 3.2: Typical time trace of the CTA scanning system: sequence of 6 wire temperatures

For each overheat step, the fluctuating output voltage $e'(t)$ is measured at the AC output and the mean value $\overline{e(t)}$ at the DC output. With the help of the calibration coefficients F and G , a whole fluctuation diagram can then be obtained within one run of the SWK. The time delay per temperature step, and therefore the number

of points in the fluctuation diagram, plays an important role in the measurement accuracy and should be chosen with regard to the flow conditions. A discussion of this parameter will be made in chapter 4.

3.3.2 Overheat determination

The usual way of adjusting the wire overheat in a CTA is to set the resistance R_b on the passive arm of the bridge at a desired value. The wire resistance (hence its temperature) is then only determined by the bridge ratio since the Wheatstone bridge is automatically balanced by the feedback amplifier when the anemometer is turned on. Therefore, a wire overheat ("balanced overheat") corresponds to each value of R_b [17].

This is only a simplified approach: although it is often neglected, the Wheatstone bridge is never perfectly balanced because of the amplifier offset, which is necessary for a stable operation. The effective wire temperature is therefore slightly different than the one which would occur for a perfectly balanced bridge. In some commercial anemometers (DANTEC) the amplifier offset voltage is fixed and results in a small fixed systematic error in the wire temperature. In other systems (A.A Lab and TSI Inc. anemometers for example), the offset voltage can be varied to control the anemometer's dynamic performance and the error is even variable. For most applications, the exact determination of the wire temperature is not of principal importance if the measurements are performed at the same settings as during the calibration, but when the fluctuation diagram technique is used, the wire temperature becomes an important parameter and its determination should be made accurately. This is especially the case when the anemometer allows an offset variation for frequency optimization purposes, as in the Cosytec CTA.

The influence of the amplifier offset on wire overheat can be computed following the method of Perry & Morisson [70]. For the present case, it is however necessary to modify their equations for an adjustable offset current instead of an offset voltage. These modifications are presented in Appendix B.

The static response of a hot-wire of length l placed in a flow may be written as [89]:

$$\overline{I_1}^2 = \left(\frac{1}{R_r} - \frac{1}{R_w} \right) \frac{\pi l k_g Nu}{\alpha_R}, \quad (3.15)$$

where R_w is the wire resistance at the operating temperature, R_r is the wire resistance at the recovery temperature, k_g is the thermal conductivity of the fluid, and α_R is the wire temperature coefficient of resistivity. The current I_1 through the wire corresponds to a Nusselt number Nu .

I_1 can also be expressed in terms of bridge electrical parameters:

$$\bar{I}_1 \simeq \frac{KR_bR_c}{\Pi + K\hat{R}} I_{offset} , \quad (3.16)$$

where I_{offset} is the offset current. The other bridge parameters are defined in Appendix B.

The static operating point of the bridge corresponds to the point where equation 3.15 and 3.16 are simultaneously valid and can best be represented graphically: the operating point for a typical $5\mu m$ wire placed in a supersonic flow of $10 \cdot 10^6/m$ unit Reynolds number is represented in Figure 3.3 for two extreme values of the offset current. The overheat ratio adjusted by balancing the bridge is $a_{balance} = 0.8$ and corresponds to a wire resistance of $R_w = 5.4\Omega$. For the minimum adjustable offset current value of $I_{offset} = 2.88 \cdot 10^{-5} A$ (operating point OP1 in figure 3.3), the effective overheat is $a_{effective} = 0.806$ ($R_w = 5.42\Omega$), which is less than 1% difference.

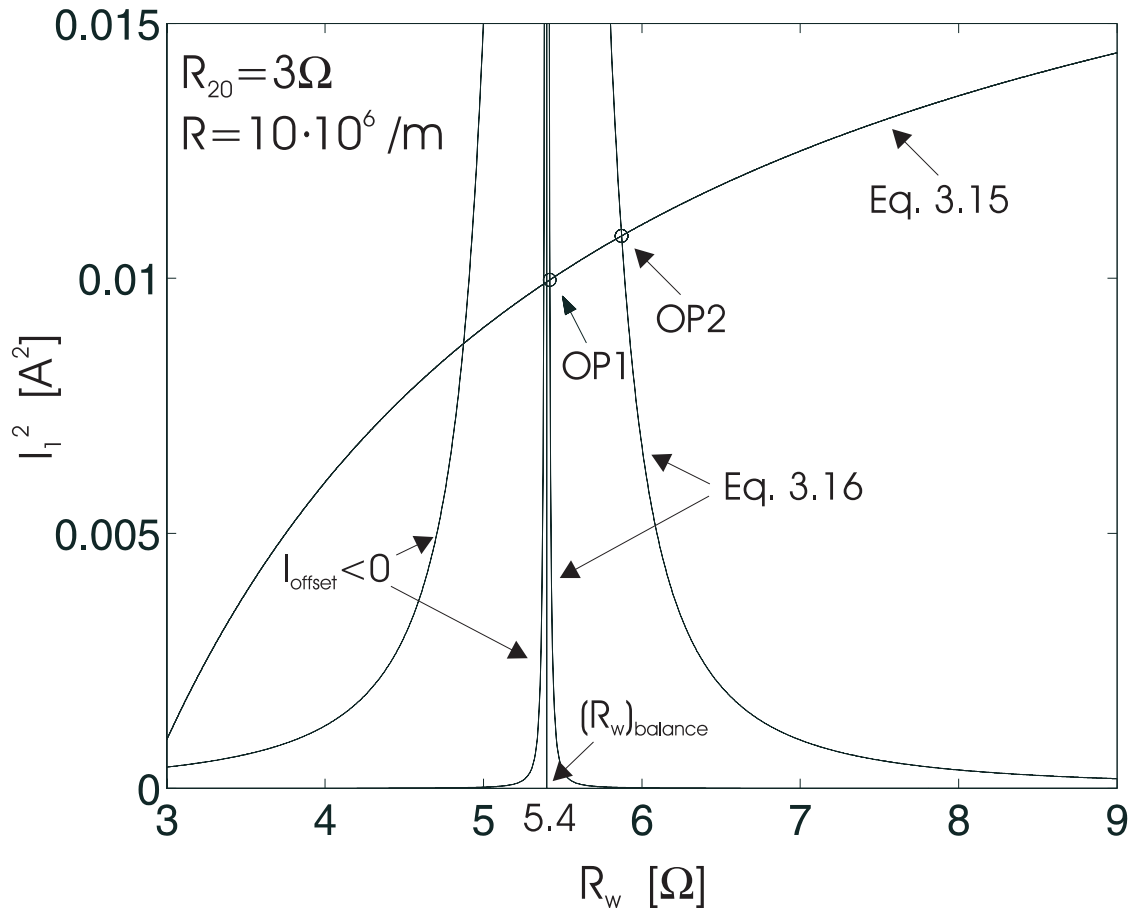


Figure 3.3: CTA operating point

On the other hand, for the maximum value of the offset current ($I_{offset} = 7.5 \cdot 10^{-4} A$, point OP2), the effective overhear reaches $a_{effective} = 0.956$ ($R_w = 5.87\Omega$), which corresponds to a real value underestimated by 20%!

The offset current is usually situated between these two extreme values. A very low offset often leads to an unstable bridge behaviour where very strong electrical oscillation can destroy the wire. In this case, a higher offset current would act like a stronger damping. Moreover, it can sometimes be of interest to work with a high offset to minimize non-linearities in temperature sensitivity [89]. Since the offset current cannot be maintained as low as desired, neglecting its effect can lead to large uncertainties in the overhear determination and hence in the whole data analysis. The underestimation of wire overhear reaches huge values at low overhear as shown in figure 3.4, where the normalized difference between "effective" and "balanced" overhear ($\Delta a = a_{effective} - a_{balance}$) is plotted as a function of $a_{balance}$. The validity of the present computation is confirmed by the work of Weidman & Browand [100], who report a difference of 50% for a balanced overhear of $a = 0.02$. Although they didn't specify the offset voltage for this special case, an order of magnitude of $2mV$ could be estimated from their electrical scheme. This value is of the same order of

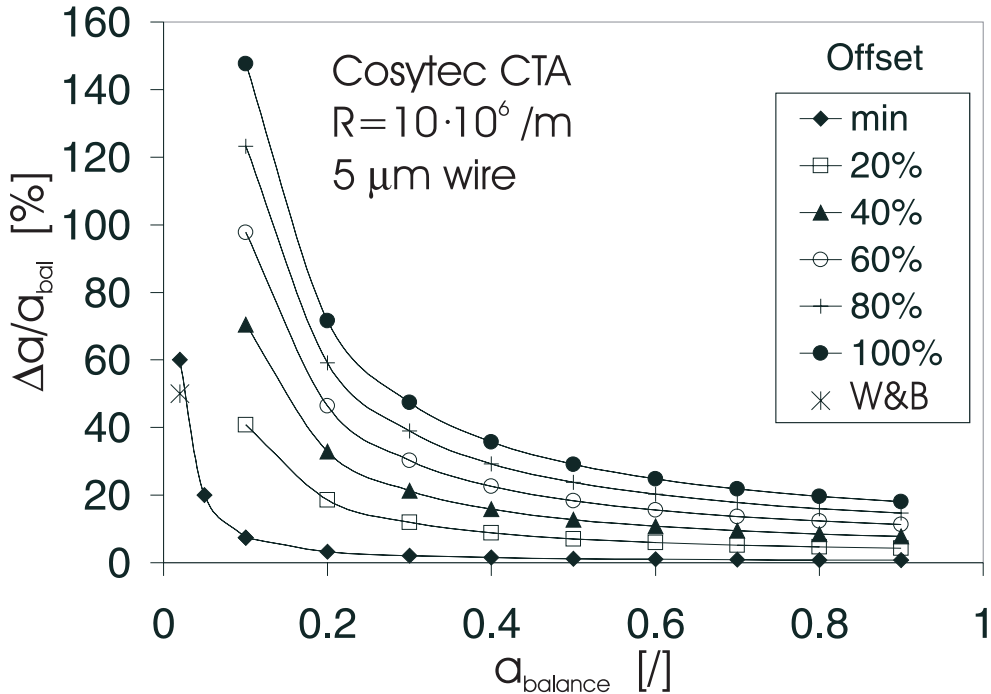


Figure 3.4: Underestimation of wire overhear for different offset currents; W&B refers to reference [100].

magnitude as the minimum offset in the present bridge and fits well in figure 3.4. Direct measurements of the effective overheat were also performed in a small wind tunnel for $R = 10 \cdot 10^6/m$, and showed a perfect agreement with the present results.

It is interesting to notice that the present analysis is in contradiction with the work of Wood [106], who argued that a very high DC gain would force the bridge into balance and annihilate the effect of offset voltage. Although the DC gain of the Cosytec CTA ($K = 1.8 \cdot 10^6$) is much higher than in the anemometer of Wood ($K = 45000$), the effect of amplifier offset is far from negligible. Wood's result can however be rationalized by noticing that he considered a much smaller domain of offset voltage: $30\mu V \leq E_{qi} \leq 100\mu V$. In this case, its influence on the operating point is very small.

In practice, the effective wire overheat can be measured by recording the voltage in the middle of the active arm of the bridge (point A in figure 3.1) simultaneously to the anemometer output voltage.

3.3.3 Dynamic behaviour

Introduction

The dynamic behaviour of hot-wire anemometers is of great importance at supersonic velocities, due to the high frequency of the flow fluctuations. A typical example was proposed by Kistler [49], who argued that measuring the velocity fluctuation $\langle u \rangle$ in a boundary layer within 10% accuracy would require an anemometer upper frequency response $f_{cut-off}$ greater than $5U_e/\delta$. For a boundary layer thickness of $\delta = 1cm$ in the SWK at $R = 10 \cdot 10^6/m$, it would require that $f_{cut-off} \geq 300kHz$. In a constant temperature anemometer, although the wire thermal lag is adjusted automatically by the feedback loop, achieving such a high frequency is far from trivial. After studying the dynamic behaviour of several CTAs at the Gas Dynamic Laboratory at Princeton University, Watmuff [99] concluded that *"with extremely careful tuning of the system controls, by the most highly skilled operators and under the most favorable of circumstances, a barely adequate frequency response of around 250kHz can be obtained with commercially available equipment"*.

Fortunately, as explained in the previous chapter, the free stream disturbances in the SWK are expected at a much lower frequency and an optimally tuned anemometer should have a sufficient bandwidth for the present investigation. The problem in this case lies in the short measurement time which does not permit a manual adjustment of the bridge. In addition, the automatic rapid scanning of wire temperature

inherently limits the tuning possibilities: even if one had time to perfectly adjust the bridge for the flow conditions, the adjustment would only be optimum for one overheat and not for the whole sequence.

Smits *et al.* [87] showed that the cut-off frequency of a CTA decreases proportionally with the overheat ratio. When considering a scanning sequence like the one presented in figure 3.2, even if the bandwidth is sufficient at the first overheat ($a = 0.9$), it is certainly much lower at the last one ($a=0.4$). An alternative would be to adjust the anemometer at a low overheat, but in this case, the system would become unstable at higher wire temperatures. To overcome this problem, the only solution is to measure the frequency response of the anemometer for every overheat constituting the sequence to ensure that the bandwidth is sufficient, or to perform a post-correction of the data if it is not the case. Since the measurement should be performed when the sensor is in the flow, this is a difficult issue in the case of the SWK, where the measurement time is limited to $120ms$!

Determination of a CTA's frequency response is usually made using an electrical test [16]. In the so-called "square-wave test", a voltage step is injected through a resistance on one side of the bridge, and the anemometer parameters are adjusted until the system response reaches a well defined shape. In this case, the system is said to be well adjusted and the anemometer's cut-off frequency can be estimated by a specific criterion. Bonnet & Alziary de Roquefort [15] tested the method in supersonic flow and compared the result with direct laser heating of the wire. Good agreement was obtained provided that the overheat ratio of the wire was not too low. The relative time consuming adjustment of the anemometer, which is necessary for an accurate cut-off frequency estimation, prevents however the use of this test in a short duration facility.

Better knowledge of the system's frequency response can be obtained with the "sine-wave test". In this case, instead of a voltage step, a sine function is injected into the bridge and the complete transfer function of the anemometer can be obtained by varying the frequency of the input and recording the amplitude and phase of the output signal. This represents a striking advantage compared to the square wave test since it enables post-anemometer compensation if the frequency of the fluctuations is higher than the cut-off frequency of the system. Although the method can be automated [98], it is even more time consuming than the square-wave test and therefore unsuitable in a short duration facility like the SWK.

An improvement of the original square-wave test to estimate the transfer function of a CTA bridge in several milliseconds has been developed in the framework of

this thesis [102]. It enables direct measurement of the Cosytec bridge's frequency response in the SWK and is now described in more details.

Cosytec bridge frequency response determination in the SWK

The dynamic behaviour of constant temperature anemometers has been investigated by numerous authors. Freymuth [29, 30, 32] derived a third order theory which enables a two-parameter optimization of the frequency response. Another approach was followed by Perry & Morisson [70] and Wood [106], who argued that a second order model would suffice to capture the basic characteristics of a real system. Higher order effects were considered by Watmuff [99], who showed that these could lead to a misinterpretation of the anemometer's square wave response. In two recent contributions, Freymuth [36, 37] concluded from a critical review of the literature that his third order theory is the best suited to account for the behaviour of a properly designed and adjusted anemometer. Measurements performed in the framework of the present thesis tend to confirm this conclusion since a third order behaviour was experimentally found for the case of a DANTEC 55M10 bridge [102] and the Cosytec Scanning system [103].

Figure 3.1 shows the electrical scheme of the Cosytec CTA. Zw is the combined impedance of the hot-wire and the probe's cable, which is compensated on the right side of the Wheatstone bridge by Zb . The amplifier's transfer function is $G(s)$, where s is the Laplace variable. Let $H_B(s)$ be the transfer function of the bridge to an input in wire heat transfer:

$$H_B(s) = \frac{e'(s)/\bar{e}}{h'(s)/\bar{h}}, \quad (3.17)$$

where \bar{h} (resp. \bar{e}) is the mean value of the wire heat transfer coefficient (resp. the anemometer output voltage) and h' (resp. e') its fluctuating part.

To perform an electrical test of the system, a voltage perturbation $e'_g(s)$ is injected at point A (see figure 3.1) through a resistance R_s which is much larger than the total bridge resistance. $H_E(s)$ is the corresponding transfer function:

$$H_E(s) = \frac{e'(s)}{e'_g(s)}. \quad (3.18)$$

A general result of the aforementioned theoretical works is that both transfer functions H_B and H_E have the same poles. Moreover, one additional zero in the transfer function for electrical perturbations is always a simple zero with a time constant

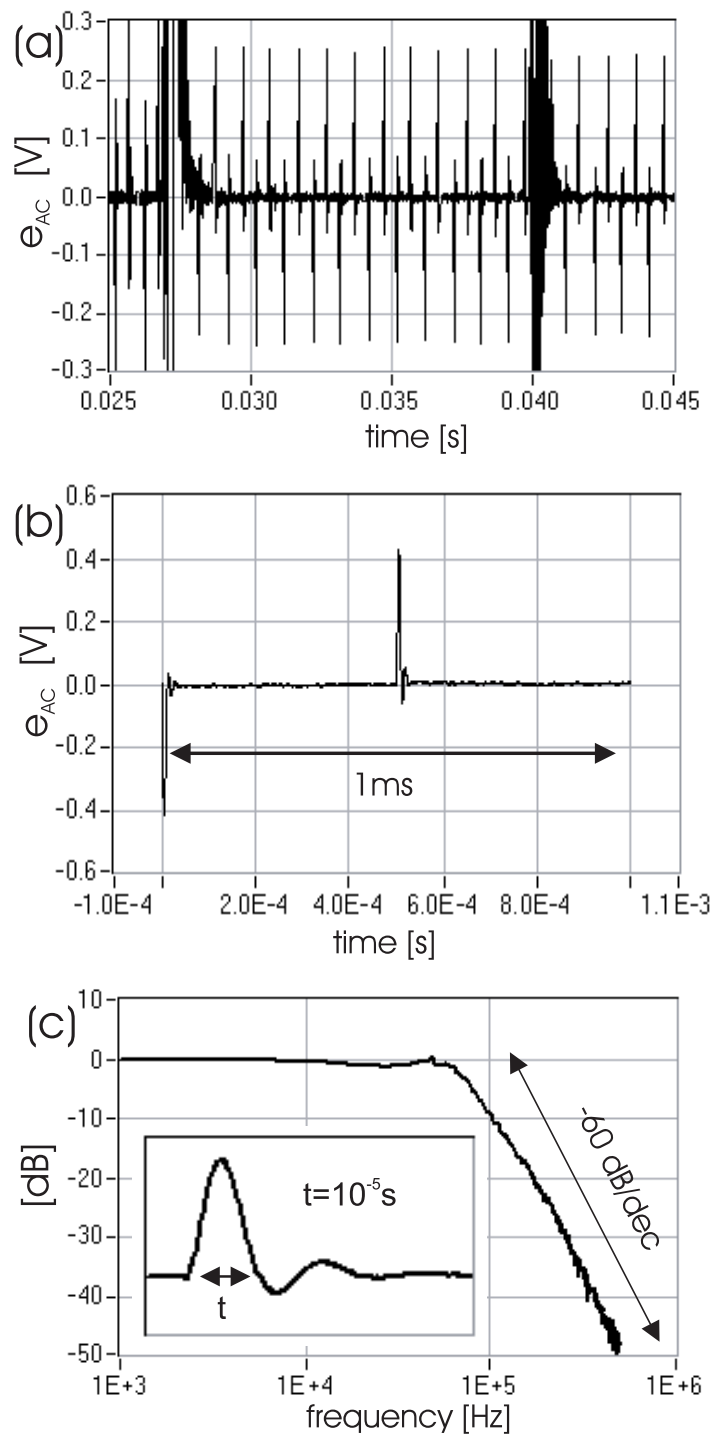


Figure 3.5: Frequency response determination: (a) AC output voltage with electrical square-wave input; (b) AC response to one square-wave period (phase averaged from (a)); (c) bridge frequency response (FFT from (b)), inset: conventional square-wave response

close to that of the wire filament [99]. This simple zero is responsible for causing the electronic square-wave response to have an appearance resembling that expected from a delta function impulse of velocity [30]. In other words, H_B can be approximated by:

$$H_B(s) \simeq \frac{K_1}{s\tau_w + 1} H_E(s), \quad (3.19)$$

where τ_w is the thermal time constant of the wire and K_1 is constant. When an electrical square-wave signal $e'_g(t)$ (which Laplace transform $e'_g(s)$ is the single pole $1/s$) is injected in the bridge, equation 3.19 leads to:

$$H_B(s) = K_1 \frac{s}{s\tau_w + 1} L[e'(t)], \quad (3.20)$$

where $L[e'(t)] = e'(s)$ is the Laplace transform of the corresponding bridge output signal. For an harmonic analysis, the Laplace variable s is replaced by $j\omega$ and the Laplace transform by the Fourier transform. Equation 3.20 can be rewritten:

$$H_B(j\omega) = \frac{jK_1\omega}{j\omega\tau_w + 1} F[e'(t)], \quad (3.21)$$

where F is the operator of the Fourier transform. If only frequencies higher than the thermal frequency $1/\tau_w$ are considered, equation 3.21 simplifies to:

$$H_B(j\omega) \simeq \frac{K_1}{\tau_w} F[e'(t)]. \quad (3.22)$$

At frequencies higher than the thermal frequency of the wire, the transfer function of a CTA can be approximated by the normalized Fourier transform of the response of the bridge to a step input in voltage. This result was used in reference [102] to determine the frequency response of a DANTEC 55M10 CTA for different bridge settings. The same method can be used to determine the frequency response of the Cosytec scanning system for every overheat constituting a sequence: an electrical square-wave is injected on the active arm of the bridge when the sensor is in the flow and for each overheat step, a Fourier transform is computed, as illustrated in figure 3.5. The AC coupled part of a scanning sequence containing one full overheat step is shown in figure 3.5a, where the electrical perturbations can be seen superimposed to the small flow fluctuations. To get a clean signal, 5 square wave periods are phase averaged (figure 3.5b) and a fast Fourier transform (FFT) is then computed to obtain the anemometer's frequency response. This result, as well as the traditional square-wave response, is shown in figure 3.5c.

Figure 3.6 compares the transfer function obtained by the present method and a traditional sine wave test in the free stream of a suck down wind tunnel at

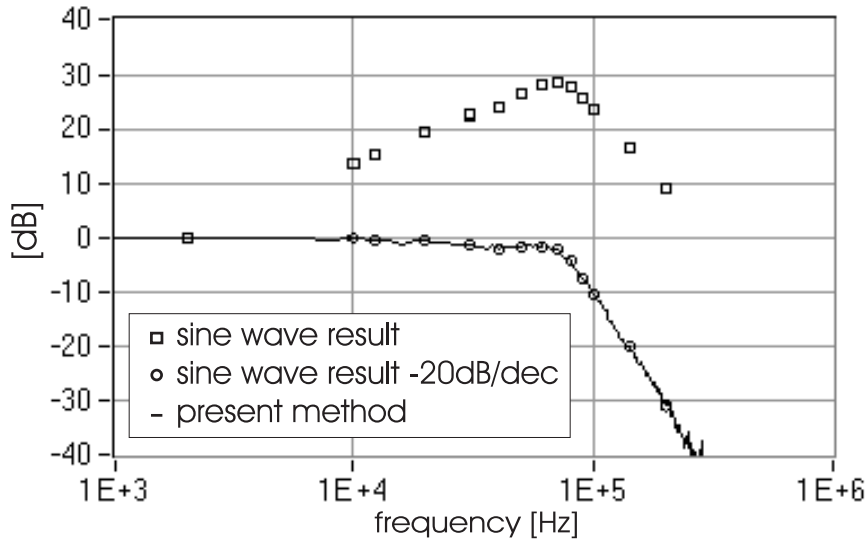


Figure 3.6: Comparison between a sine wave test and the present method of frequency response determination

$Ma = 2.54$. As expected the agreement between the two methods is excellent, but plotting the sine wave results required 14 adjustments of the frequency generator and 14 time trace measurements, whereas the present method required only 1 of each. The time gained using the present method is therefore evident. In any event, using the sine wave test in a short duration wind tunnel would be impossible.

The use of this new method enables therefore a very fast determination of the anemometer's frequency response for every wire temperature, but there is no guarantee that the bandwidth is sufficient to perform an accurate measurement of the flow fluctuations. Indeed, as explained above, the dynamic behaviour of the Cosytec scanning system cannot be optimized for every overheat step. It is however possible to use the measured frequency response to perform a post-processing of the data.

Data post-processing

"Post-processing" of hot-wire results is not a new technique. It has been performed since hot-wire anemometers have been used to measure flow fluctuations. In essence, it consists in correcting the output voltage of the anemometer to account for its too small bandwidth. For a CCA, this is usually made by an in-line analog high-pass filter that is tuned to match the wire thermal frequency (compensator). The painstaking process of determining the wire thermal frequency even led to the development of CTA systems, where compensation is done automatically by the feedback

loop. The bandwidth of CTA systems is however not infinite, and measuring turbulent fluctuations at frequencies higher than their cut-off frequency requires the same type of compensation. Due to progress in digital data acquisition equipments, this can now be done numerically, after the signal has been memorized (hence the term "post-processing") [98]. As for CCA compensation, it requires that the frequency response of the anemometer is known.

It is noteworthy that digital data post-processing was successfully used by Comte-Bellot & Sarma [21] when measuring turbulent fluctuations at supersonic speeds with a CVA. In this work, signals were acquired with the CVA compensated with a fixed time constant at all test points and the *in situ* hot-wire time constant was also measured to perform a post-processing of the data. This method, which could in principle also be used for a CCA, showed a larger bandwidth than in the case of full hardware compensation.

For a CTA, the problem is further complicated by the shape of the frequency response, which cannot be accounted for by a simple first order model like in the CCA and CVA. Measurement of the whole frequency response is therefore necessary instead of the lone time-constant⁵. A method like the one presented in the last section is therefore of great advantage since it enables a very fast determination of the system's frequency response.

Figure 3.7 illustrates the post-processing technique for a hot-wire placed in a supersonic test section and connected to a DANTEC 55M10 CTA bridge [102]. The flow fluctuations were measured with two different bridge adjustments (adj. (a) and (b)), corresponding to the two transfer functions showed in the inset. The large difference in the bridge's frequency response account for a large difference in the power spectra (curves (a) and (b)). However, when spectra (a) and (b) are corrected using the corresponding transfer functions, the resulting curves (c) and (d) show a very good agreement.

Knowing the frequency response of a CTA therefore enables measurements of turbulent fluctuations when the bridge adjustment is not optimal. This is especially helpful in short duration facilities, where no manual adjustment is possible. The method presented in this section enables free stream disturbance measurements in the SWK with the Cosytec scanning CTA. For each unit Reynolds number and bridge

⁵The cut-off frequency of the system is theoretically enough information for data post-processing if a third order model is assumed and if the bridge is perfectly tuned (*ie* the system behaves like a Butterworth filter of order three [36]). Since it is generally not the case, the whole frequency response is needed.

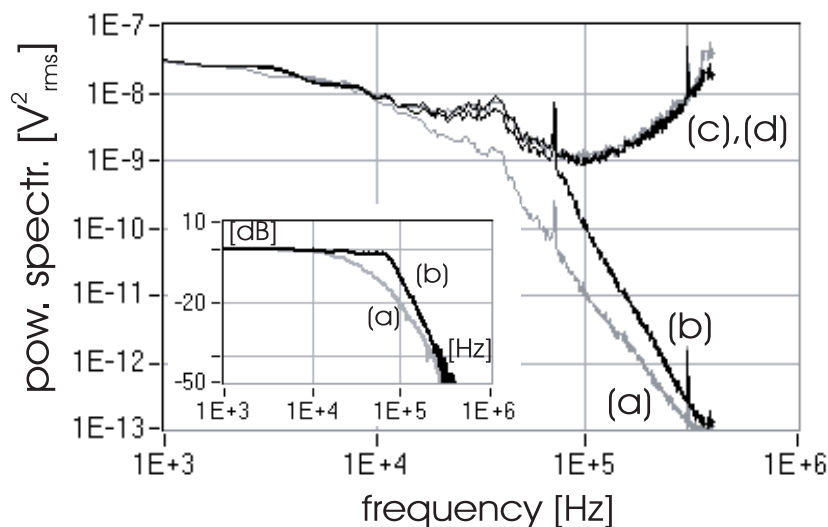


Figure 3.7: (a), (b) free stream disturbance power spectra for two different bridge adjustments; (c), (d) corresponding corrected spectra; inset: bridge frequency response corresponding to the adjustments in (a) and (b)

settings where fluctuation measurements are performed, the transfer function of the whole scanning sequence is measured to be able to correct the AC output.

3.3.4 Signal to noise ratio

The corrected spectra presented in figure 3.7 show an unexpected rise in frequency beyond 100kHz . This rise is attributed to the electronic noise of the system and confirms the theoretical work of Freymuth [31] and the experiments of Saddoughi & Veeravalli [80], who proved that the electronic noise power spectrum of a CTA rises like the square of the frequency. This increase in frequency, which is usually limited by the cut-off frequency of the system, is present here at a higher frequency because of the signal post-processing. Indeed, correcting the signal power spectrum is equivalent to simulating a bridge with infinite frequency response. In this hypothetical case, the power spectrum of the electronic noise would increase indefinitely with the frequency and there would always be a limit in the usable frequency range where the electronic noise becomes greater than the turbulent signal. The data post-processing technique allows therefore an accurate estimation of the system's signal to noise ratio (SNR), as illustrated in figure 3.8.

While processing the experimental data, care should always be taken to separate

the part of the signal which is due to fluctuations from the flow ($f < f_{max}$), from the part which is caused by electrical noise ($f > f_{max}$).

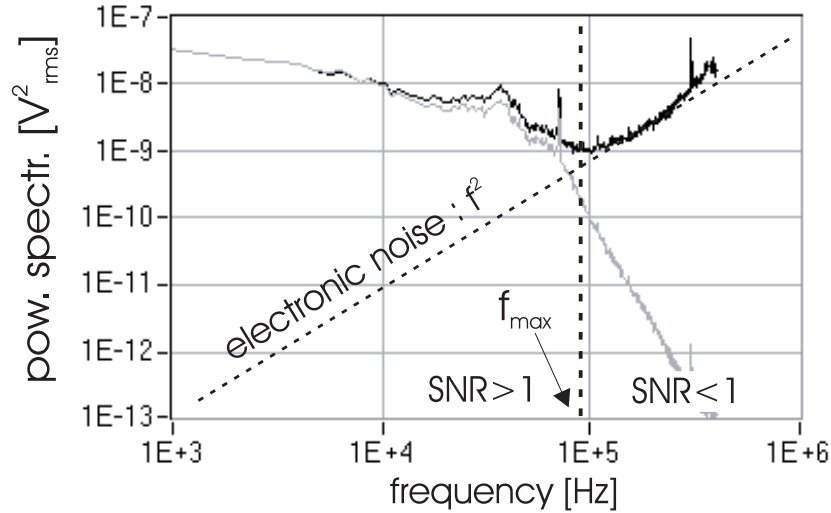


Figure 3.8: Estimate of the signal to noise ratio (SNR)

3.4 Hot-wire sensor

3.4.1 Generalities

The hot-wire sensor used in the present work was a commercial DANTEC 55P11 probe. A tungsten wire of $5\mu m$ diameter and $1.2mm$ length was spot welded to its prongs. This diameter resulted in a Reynolds number Re_2 greater than 20 for a unit Reynolds number greater than $10 \cdot 10^6$ (necessary condition for equation 3.1 to be valid). Experimental investigations revealed a recovery factor of $\eta = 0.955$ for the present probe design.

It is assumed that the finite length of the hot-wire doesn't induce any spatial filtering effect for the present measurements since the frequency of the fluctuations is rather small. It will be shown in the next chapter that the measured spectrum is dominated by electronic noise at frequencies above $30kHz$. If one considers a typical free stream velocity of $575m/s$ (for $R = 10 \cdot 10^6/m$), this frequency corresponds to a wavelength of approximately $2 \cdot 10^{-2}m$ which is much larger than the wire length.

To avoid strain-gaging, the wire filament was slightly slackened and the prongs were glued together to reduce their eigen-oscillations. Figure 3.9 shows a picture of the

sensor. Since wire slackening is not a 100% reliable procedure [86], each new wire was tested before a measurement set and re-soldered if strain-gaging effect was present. Wires were considered reliable if the characteristic high-frequency oscillations were either not present at all, or present at a frequency dominated by electronic noise.

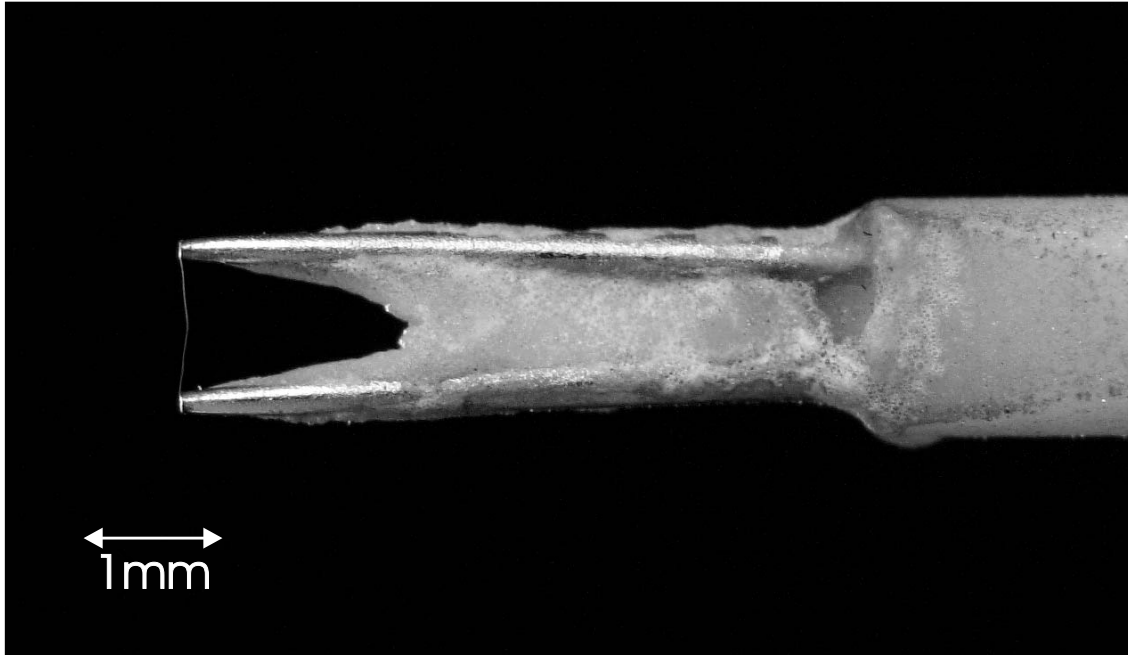


Figure 3.9: Hot-wire sensor

For $R \leq 25 \cdot 10^6/m$, wire breakage in the SWK is not a serious problem anymore since a new painting was applied in the driver tube to reduce dust emission (see chapter 2 and reference [78]). During the whole measurements performed within this work, the hot-wire broke only three times.

3.4.2 End-conduction effects

The effect of wire end-conduction on the anemometer's dynamic performance has been taken into account using the methods proposed by Freymuth [33]. Basically, dynamic end-loss effects can be interpreted as an attenuation in heat transfer fluctuations from a reference level $A(f \rightarrow 0) = 1$ at very low frequency (quasi-static response) to another level $A(f \gg f_l) = \epsilon' \leq 1$ where f_l is a transition frequency. In other words, the anemometer static sensitivity should be corrected by the factor ϵ' whenever frequencies higher than f_l are considered. In compressible flows, two

specific attenuation factors for mass flow and total temperature should be estimated to be able to correct the sensitivity coefficients F and G .

Mass flow fluctuations

The attenuation factor ϵ_F for mass flow fluctuations is related to the attenuation of heat waves traveling on the filament. According to Freymuth [33], it is a function of the hot-wire Biot number B_i . The transition frequency after which this attenuation should be taken into account is $f_l = 40D_w/(2\pi l^2)$ where l is the wire length and D_w is the thermal diffusivity of the wire material. For small overheats, the wire Biot number can be approximated by [33]:

$$B_i = \frac{l}{d} \left(\frac{k_g}{k_w} Nu \right)^{1/2}, \quad (3.23)$$

where l/d is the wire aspect ratio, k_w (resp. k_g) is the thermal conductivity of the wire material (resp. of the fluid) and Nu is the Nusselt number.

The present hot-wire and flow conditions:

$$\begin{aligned} l/d &= 240, \\ k_g/k_w &= 1.61 \cdot 10^{-4}, \\ D_w &= 6.3 \cdot 10^{-5} m^2/s, \\ Nu &\sim 2.5, \end{aligned} \quad (3.24)$$

lead to a transition frequency $f_l = 280Hz$ and a Biot number $B_i = 4.8$. According to the charts of reference [33], the attenuation is then $\epsilon_F = 0.9$. As will be shown in chapter 4, only frequencies higher than f_l will be considered in the data processing and the mass flow sensitivity should therefore always be corrected by ϵ_F . In other words, the modal analysis should be performed using the dynamic sensitivity $F_{AC} = \epsilon_F F$.

It should be noted that reference [33] enables an accurate calculation of ϵ_F for every overheat and flow conditions rather than the low overheat estimate of equation 3.23. This analysis is however restricted to the simplified case of a straight wire. As shown by Perry *et al.* [71] and Smits & Dussauge [86], wire end-conduction effects can be much more complicated and depend on aeroelastic deflexions of the wire and non-uniform cooling. The slackening of the filament, which is necessary to avoid strain gaging, is certainly another important parameter. The present estimation is therefore preferred for its simplicity.

Total temperature fluctuations

At very low frequency, a variation in stagnation temperature produces a change in the wire support's temperature, which has an influence on the heat transfer from the wire to the support. Due to the relative large heat capacity of the probe support, the corresponding conduction fluctuations are attenuated at higher frequencies. As a result, the total temperature sensitivity G of the system is attenuated by a factor ϵ_G after a transition frequency of the order of $1Hz$. Therefore, data processing in the modal analysis will be performed with a dynamic sensitivity $G_{AC} = \epsilon_G G$, where $\epsilon_G = 0.8$, according to reference [33].

3.5 Calibration

3.5.1 Generalities

Processing of hot-wire's data require the experimental determination of the two calibration coefficients F and G defined as:

$$F = \frac{d(\ln(e))}{d(\ln(\rho u))}, \quad G = \frac{d(\ln(e))}{d(\ln(T_0))}. \quad (3.25)$$

For a constant temperature anemometer, F can be easily determined by recording the output voltage e while varying the wind tunnel mass flux at a constant stagnation temperature. This procedure should be repeated for different overheat parameters and gives a plot of e versus ρu enabling the computation of F [86].

The direct determination of G can also be performed following the same procedure [14] but it appears that independently varying the stagnation temperature at a constant mass flux usually presents practical difficulties, so that a semi-empirical relation between the Nusselt and the Reynolds number of the hot-wire is usually used instead. In the SWK, the total temperature cannot be varied, so that such an indirect method has to be used.

According to Smits *et al.* [87], the heat transfer from a heated fine wire in supersonic flow is best described by the following semi-empirical relation:

$$Nu = Af(\tau) + Bg(\tau)Re^n, \quad (3.26)$$

where A and B are constant for a given wire and $f(0) = g(0) = 1$. The exponent n is chosen to minimize the error in the least squares fit of $Nu(Re^n)$ and varies usually between 0.4 and 0.55.

Nu can be related to the anemometer's output voltage e , so that once a plot of e versus ρu is obtained for a given stagnation temperature, the quantities A , B , $f(\tau)$, and $g(\tau)$ can be determined. Equation 3.26 can be written in the dimensional form $e^2 = L + N(\rho u)^n$, and F and G can then be obtained using the following relations, which are directly deduced from equation 3.26 [53]:

$$\begin{aligned} F &= \frac{n}{2} \left(1 - \frac{L}{e^2} \right), \\ G &= \frac{1}{2} \left(a_k - \frac{\eta}{\tau} - 2b_\mu F - \frac{\tau + \eta}{n} \left[(n - 2F) \frac{f'(\tau)}{f(\tau)} + 2F \frac{g'(\tau)}{g(\tau)} \right] \right). \end{aligned} \quad (3.27)$$

In these relations, a_k and b_μ are constants in the power laws relating the air thermal conductivity and viscosity with the temperature: $k_g(T) = k_g(T_1)(T/T_1)^{a_k}$, $\mu_g(T) = \mu_g(T_1)(T/T_1)^{b_\mu}$, and η is the wire recovery factor. The values proposed by Kovásznyai [54] were used in the present work: $a_k = b_\mu = 0.768$.

It should be noted that the two calibration coefficients F and G are only valid for the stagnation temperature $(T_0)_c$ at which the calibration was performed. Extrapolation for another stagnation temperature can be made using the methods of reference [87], provided that the temperature difference is not too high. However, since L is usually small, it is often assumed that F is approximately constant and it follows from equation 3.27 that G is only a function of τ .

The use of the Cosytec CTA scanning system enables a relative fast calibration procedure since the wire overheat is automatically scanned within a sequence. This enabled an *in situ* calibration of the system in the Shock Wind Tunnel simultaneously to the fluctuation measurements⁶. In practice, the same sequence of overheats was scanned within several runs of the SWK at different stagnation pressures, so that a plot of Nu versus Re^n was obtained. The stagnation temperature only varied of a few degrees between the runs and the calibration stagnation temperature $(T_0)_c$ was defined as its average. Figure 3.10 shows an example of the resulting plots for an overheat parameter $\tau = 0.45$. It appeared that the exponent $n = 0.59$ is the best suited to fit the experimental data. This value is a little higher than usual but should be used with confidence since n is strongly dependent on the probe design.

In practice, figure 3.10 was obtained by performing 6 tests for every of the 4 following values of the unit Reynolds number R : $10 \cdot 10^6/m$, $15 \cdot 10^6/m$, $20 \cdot 10^6/m$, and $25 \cdot 10^6/m$. This redundancy in the measurements was necessary to reduce the

⁶It should be noted that there is at present no other supersonic facility at IAG where the stagnation pressure can be varied, so that the calibration procedure *had* to take place in the SWK, although the short measurement time resulted in a more complicated procedure.

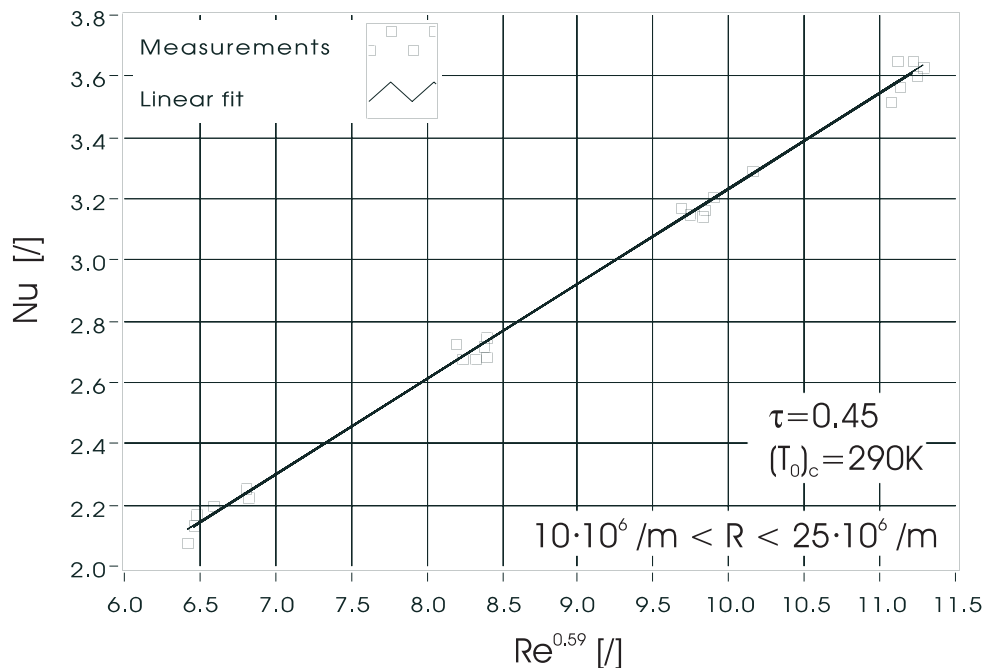


Figure 3.10: Calibration in the SWK: plot of Nu versus Re^n

uncertainties, especially at low overheat parameter. The 4 values of R were chosen for the purpose of fluctuation measurements (see chapter 4), which were performed simultaneously by analyzing the AC output of the bridge.

Once a plot like figure 3.10 is obtained for different overheat parameters τ , the functions $f(\tau)$ and $g(\tau)$ can be determined. Figure 3.11 shows the corresponding result for 12 different overheat parameters ranging from 0.04 to 0.89. These data were obtained in two measurements sets of 24 tests where six overheats were scanned within each wind tunnel run.

For $\tau > 0.1$ the functions $f(\tau)$ and $g(\tau)$ show a linear decreasing character which has been obtained by many researchers [87, 54, 59, 53]. For the current probe design, the following relations are obtained:

$$\begin{aligned} f(\tau) &= 1 - 0.72\tau, \\ g(\tau) &= 1 - 0.18\tau. \end{aligned} \quad (3.28)$$

For overheat parameters lower than 0.1, the present data doesn't fit in the straight line. This can be due to the very large sensitivity of the anemometer to uncertainties in the stagnation temperature during the calibration (see sections 3.5.2 and 3.5.3).

Once $f(\tau)$ and $g(\tau)$ are fitted to the experimental data, the non-dimensional mass flow and total temperature sensitivities F and G can be determined using equations

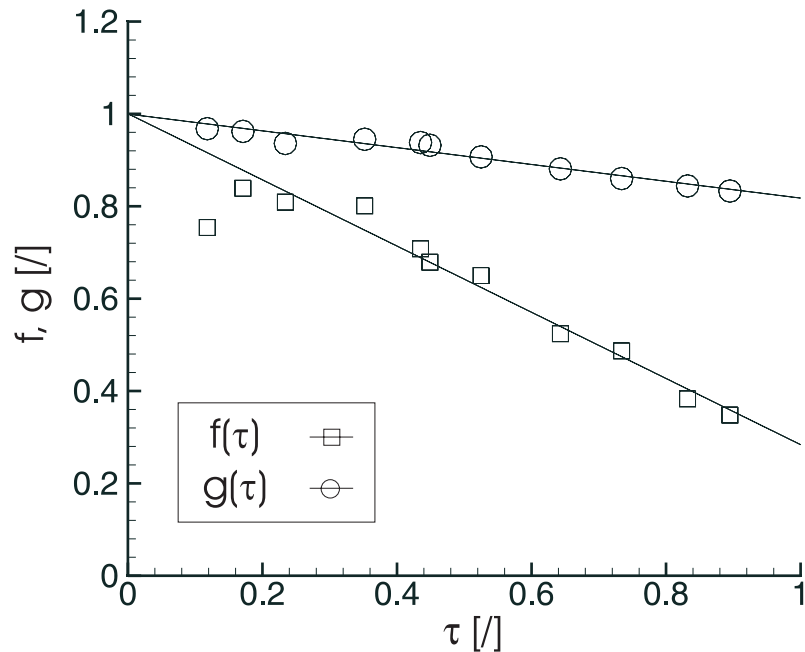


Figure 3.11: Calibration in the SWK: plots of $f(\tau)$ and $g(\tau)$

3.27. As can be shown in figure 3.12, F is slightly increasing with the overheat ratio, a result which is consistent with the calibration of Kosinov *et al.* [53]. For small overheat parameter (say $\tau < 0.4$), $|G| \gg F$ and the CTA is more sensitive to total temperature fluctuations than mass flow fluctuations.

3.5.2 Accuracy

An uncertainty estimate of the calibration factors F and G seems necessary since they are obtained in a rather indirect way involving several numerical curve fitting procedures. Moreover, the result of the modal analysis, and thus its accuracy, directly depends on F and G .

The largest source of uncertainty in the calibration lies in the small change of the stagnation temperature T_0 between each run of the SWK. As already explained in chapter 2, the filling process of the driver tube results in an uncontrolled temperature rise, so that a perfect adjustment of the loading temperature T_L (from which T_0 is deduced) is impossible. This effect results in a small scattering of the stagnation temperature between different wind tunnel runs, which may reach several degrees. As a consequence, the anemometer output voltage records are also scattered, and it becomes especially critical at low overheat ratio, where the bridge is very sensitive

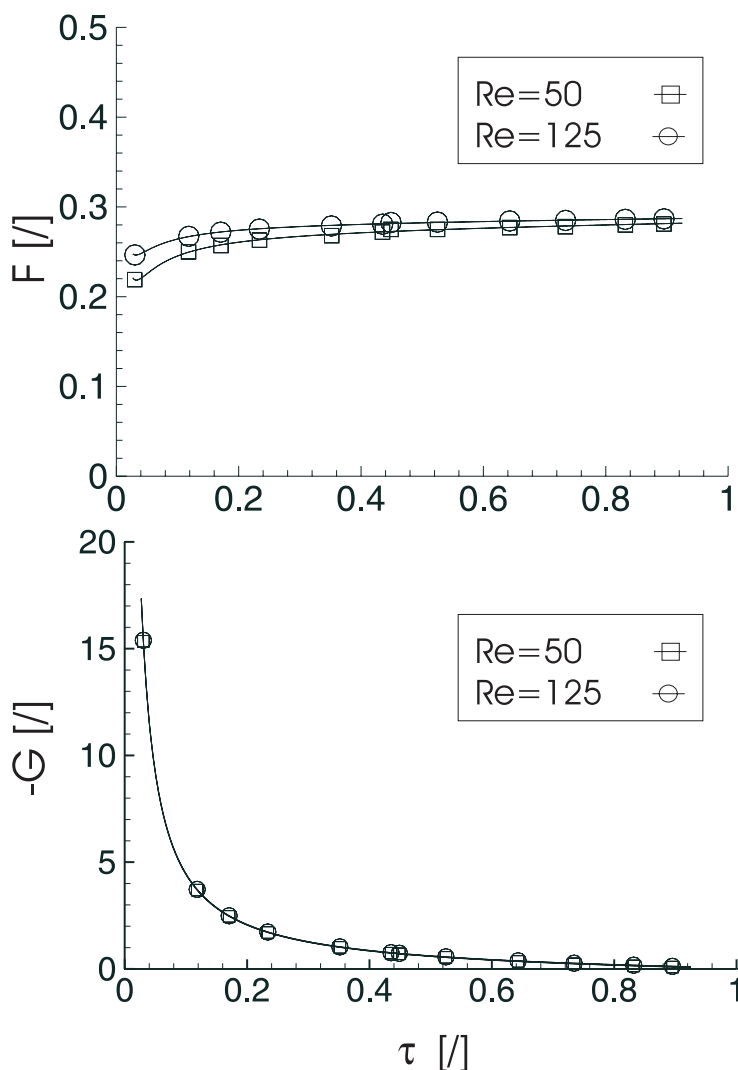
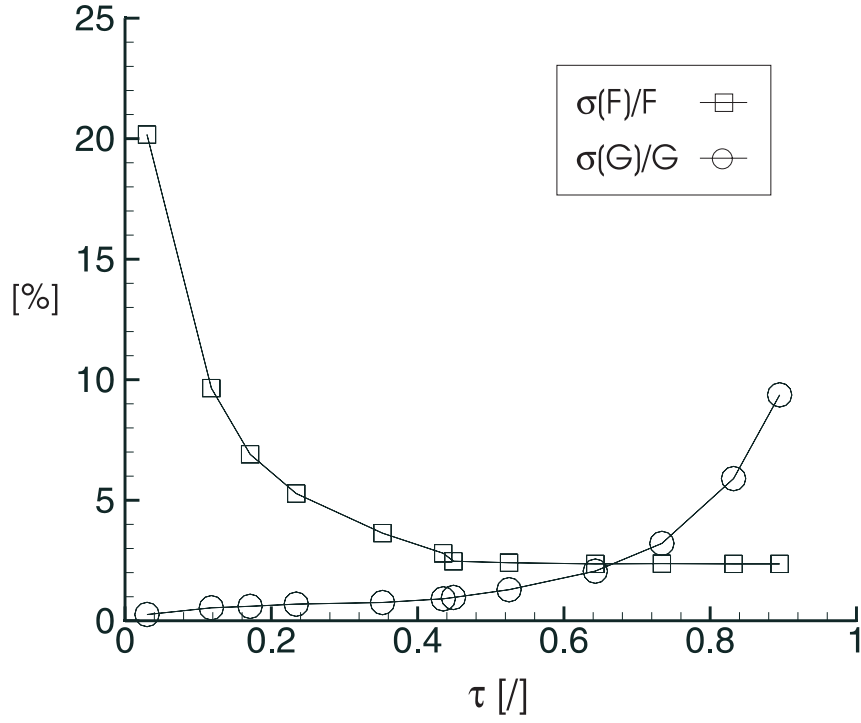


Figure 3.12: Calibration in the SWK: plots of F and G upon τ (Reynolds number based on wire diameter and free stream conditions)

to total temperature variations.

F can be approximatively estimated by plotting $\ln(e)$ as a function of $\ln(\rho u)$ and fitting the data to a straight line. In the dimensional relation $e^2 = L + N(\rho u)^n$, L is much lower than $N(\rho u)^n$, so that $F = \frac{d(\ln(e))}{d(\ln(\rho u))} \approx \frac{n}{2}$. The uncertainty in F is therefore calculated by the linear least squares algorithm if an uncertainty in $\ln(e)$ is known. Now the standard deviation $\sigma(\ln(e))$ can easily be estimated by performing redundant measurements as shown in figure 3.10, so that $\sigma(F)$ is directly obtained.

The uncertainty in G can be calculated from equation 3.27. If one assumes that

Figure 3.13: Relative uncertainty of calibration coefficients F and G

$F \approx n/2$, 3.27 becomes:

$$G = \frac{1}{2} \left(a - \frac{\eta}{\tau} - 2bF - (\tau + \eta) \frac{g'(\tau)}{g(\tau)} \right). \quad (3.29)$$

From the usual law of random error propagation, it follows that:

$$\sigma(G) = \sqrt{(b\sigma(F))^2 + \left(\frac{\tau + \eta}{2} \sigma(g'/g) \right)^2}. \quad (3.30)$$

Moreover, assuming $\sigma(g')/g' \sim \sigma(g)/g$ yields:

$$\begin{aligned} \sigma(g'/g) &= \sqrt{(-g'/g^2)^2 \sigma^2(g) + \sigma^2(g')/g^2} \\ &= \sqrt{\frac{2g'^2}{g^2} \frac{\sigma(g)}{g}}. \end{aligned} \quad (3.31)$$

$\sigma(g)$ can be obtained by the linear fit of $Nu(Re^n)$ and the relative uncertainties $\sigma(F)/F$ and $\sigma(G)/G$ are plotted in figure 3.13 as a function of τ . The relative uncertainty of F is constant at high overheat (approximately 2.5%) but increases in a drastic way at low overheat, due to a greater sensitivity of the anemometer DC

output voltage to small variations of the total temperature. The relative uncertainty in G is small when τ is low but increases at high overheat. This is due to the fact that G decreases with increasing τ although the absolute uncertainty tends to be constant, thus resulting in an increasing relative uncertainty.

The present *in situ* calibration of the anemometer in the SWK resulted in a quite high uncertainty in the calibration coefficients, mainly due to an inaccurate adjustment of the total temperature between the wind tunnel runs. The accurate calibration of a CTA at supersonic velocity is a rather tricky procedure which should be made in a specially designed calibration wind tunnel whenever possible. But it will be shown in the next chapter that these uncertainties in F and G don't have any unacceptable influence on the modal analysis results.

3.5.3 Non-linearity at low overheat ratio

The problem of CTA's non-linear response to temperature fluctuations at low overheat ratio was first pointed out by Smits & Perry [89] and Smits *et al.* [87]. Since $\tau = \frac{T_w - \eta T_0}{T_0}$, a small variation of T_0 produces a relative large variation of τ when T_w is maintained constant ($\frac{d\tau}{\tau} = \left(\frac{\tau + \eta}{\tau}\right) \frac{dT_0}{T_0} \xrightarrow{\tau \rightarrow 0} \infty$). Moreover, since G is a strong function of τ at low overheat, the instantaneous sensitivity can differ significantly from its value at the average gas temperature, thus precluding the use of the linear based modal analysis (equation 3.3). Smits *et al.* [87] estimated the error arising from this non-linear behaviour and showed that it is function of the anemometer's offset voltage. This behaviour even led Smits & Dussauge [86] to preclude the use of CTAs for overheat ratios lower than 0.4.

On the other hand, Bestion *et al.* [12] showed good agreement between CTA and CCA measurements in the free stream of a supersonic wind tunnel at $Ma = 2.3$. This can be explained by a very low level of total temperature fluctuations for this special case. Indeed, it is intuitively obvious that there is always a fluctuation level under which linearization is still possible, as long as the sensitivity is finite.

An estimation of the non-linearity for total temperature fluctuations can be made by a second order development of the output voltage $e(T_0)$. Since we are only interested in total temperature fluctuations, the mass flow over the wire is supposed constant and for a small variation T_0' resulting in a small variation e' of the output voltage, one can write:

$$e' = k_\theta T_0' + \frac{1}{2} \frac{dk_\theta}{dT_0} (T_0')^2 + o(T_0'^2), \quad (3.32)$$

where $k_\theta = \frac{de}{dT_0}$ is the anemometer's total temperature sensitivity.

Linearization of $e(T_0)$ is only allowed if the first term on the right hand side of equation 3.32 is at least an order of magnitude greater than the second one, that is:

$$|T'_0| \ll \frac{|2k_\theta|}{\left|\frac{dk_\theta}{dT_0}\right|}. \quad (3.33)$$

Recalling that $G = \frac{d(\ln(e))}{d(\ln(\rho u))} = \frac{k_\theta T_0}{e}$, equation 3.33 can be written in the following non-dimensional form:

$$\frac{|T'_0|}{T_0} \ll \frac{|2G|}{\left|T_0 \frac{dG}{dT_0} + G(G-1)\right|}. \quad (3.34)$$

Assuming that F is not a strong function of T_0 , it follows from the definition of τ that $\frac{dG}{dT_0} = -\left(\frac{\tau + \eta}{T_0}\right) \frac{dG}{d\tau}$, and inserting this last relation in 3.34 yields:

$$\boxed{\frac{|T'_0|}{T_0} \ll \frac{2|G|}{\left|G(G-1) - (\tau + \eta) \frac{dG}{d\tau}\right|}}. \quad (3.35)$$

According to equation 3.35, linearization of $e(T_0)$ is allowed whenever

$$\frac{|T'_0|}{T_0} \ll D(\tau), \quad (3.36)$$

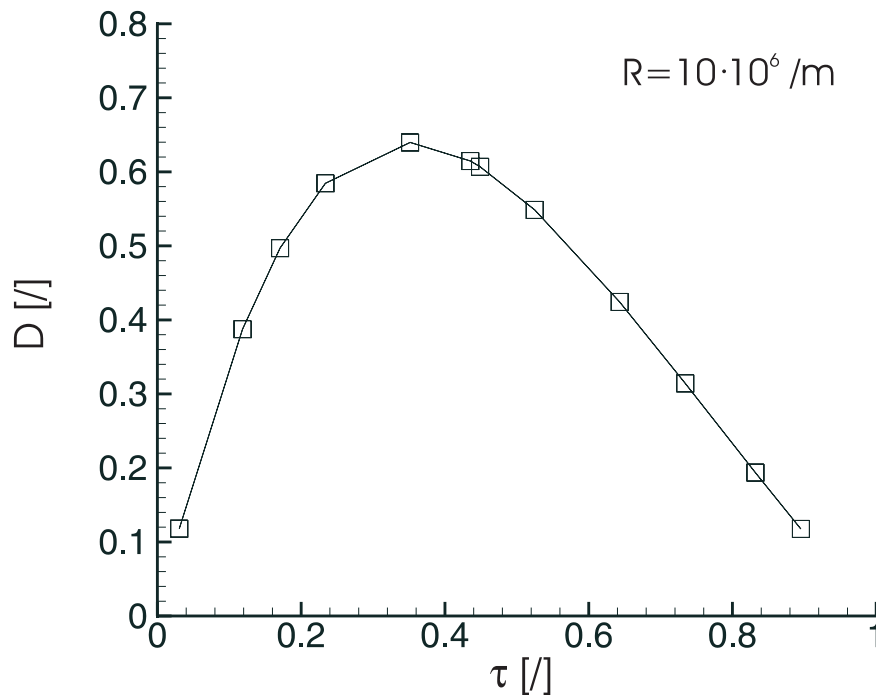
where:

$$D(\tau) = \frac{2|G|}{\left|G(G-1) - (\tau + \eta) \frac{dG}{d\tau}\right|}. \quad (3.37)$$

Now $D(\tau)$ can directly be deduced from equation 3.27 if F is assumed constant. Figure 3.14 shows a plot of $D(\tau)$ for the present calibration at a unit Reynolds number $R = 10 \cdot 10^6/m$. It was checked that $D(\tau)$ is quite independent on R .

The first interesting remark that arises from the observation of figure 3.14 is that non-linearity in the response to temperature fluctuations is not restricted to low overheat ratios. Instead of increasing monotonously, $D(\tau)$ decreases at high overheat because $G(\tau)$ tends to become smaller than its derivative. This means that if temperature fluctuations are not negligible, not only can their contribution to the anemometer output voltage be significant, even at high overheat [89], but it can even be non-linear! A check of the system's linearity appears therefore to be recommendable in any case.

Fortunately, in the case of free stream disturbances, linearity appears to be sufficient in the whole overheat domain, since we expect $\langle T_0 \rangle$ to be smaller than $0.1\mathcal{V}$. In

Figure 3.14: Plot of $D(\tau)$

this case, D is at least two orders of magnitude higher than $|T'_0|/\overline{T}_0$ and equation 3.36 is verified for $0.05 < \tau < 1.0$. Using the modal analysis down to overheat parameters as low as $\tau = 0.05$ appears therefore to be justified, as suggested by the results of Bestion *et al.* [12].

It should be noted that the present analysis supposes that the wire temperature is held constant by the feedback system. Smits & Perry [89] showed that a CTA can introduce further non-linearities at low overheat because the operating point is very sensible to changes in the stagnation temperature. This results in a decrease of total temperature sensitivity which is not taken into account in the present calibration. The data of Smits & Perry showed however that this effect is only noticeable at a very low overheat parameter (lower than 0.01) so that it is negligible in the present case.

Chapter 4

Free stream disturbances in the SWK

The results of free stream disturbance measurements performed in the SWK with the Cosytec CTA scanning system are presented in this chapter. The first section introduces important practical details related to the measurement accuracy, and the second one deals with the identification of the different disturbance modes present in the Mach rhombus. It is shown that the acoustic mode is dominant if a wind tunnel run is performed several minutes after the filling of the driver tube. The evolution of the acoustic disturbance level on the test section center line is presented in the third section and a spectral analysis of the data follows. Eventually, a possible method to reduce the noise level is proposed.

4.1 Introduction

This section introduces important concepts for a successful use of the Cosytec CTA scanning system in the SWK. In particular, the number of overheat steps, their respective length and important factors influencing the overall measurement accuracy are discussed.

4.1.1 Coordinate system

The coordinate system used in the present work is defined in figure 4.1. Hot-wire measurements were only performed on the test section center line ($y = z = 0$) between $x = 711mm$ (Mach rhombus tip) and $x = 2036mm$ (maximal x position due

to the model support). The nominal Mach number was $Ma = 2.54$ and the unit Reynolds number was varied between $R = 10 \cdot 10^6/m$ and $R = 25 \cdot 10^6/m$. Measurements were restricted to the first quasi-steady state of supersonic flow (testing time: $\sim 120ms$).

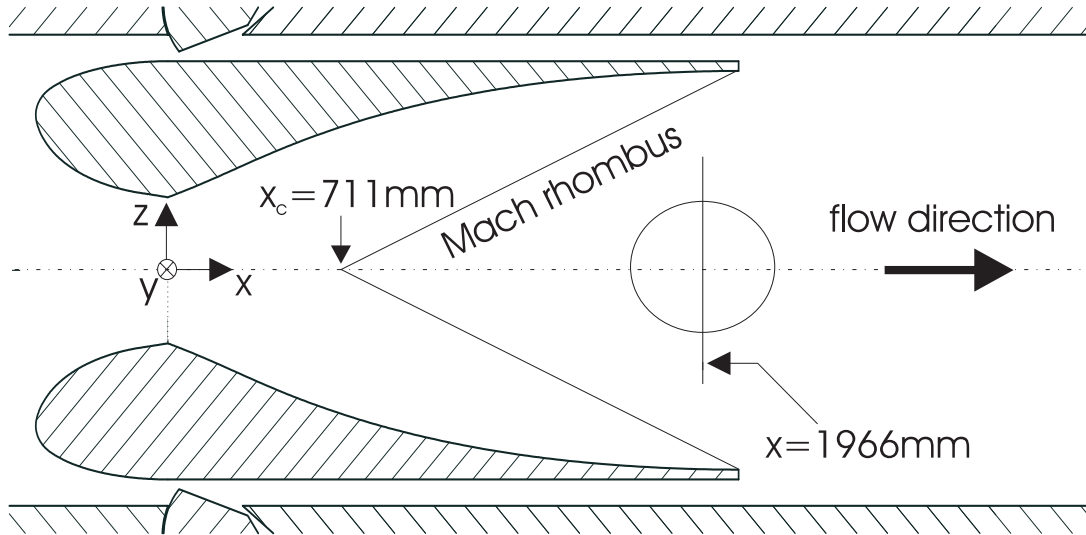


Figure 4.1: Coordinate system, $Ma = 2.54$ nozzle

4.1.2 Overheat steps

The first important parameter to choose to perform a modal analysis in one run of the SWK is the number of overheat steps in one scanning sequence. Of course, the accuracy of the modal analysis (section 3.2) is directly proportional to the number of points available for the regression, *i.e.* to the number of overheat steps. But the measurement time in the SWK is limited to $120ms$ so that a large number of steps implies a small time span per step! Now the time span per overheat step greatly influences the accuracy of the estimation of the normalized root mean square $\langle e \rangle$. Indeed, the fluctuating output voltage $e(t)$ is assumed to be a stationary random process so that a finite integration time is needed to estimate $\langle e \rangle$ statistically [9]. In general, one can say that the larger the integration time, the better the accuracy. Moreover, as will be shown in the next paragraphs, only a small part of the measured spectrum can be analysed because of the finite signal to noise ratio, thus making the issue of integration time even more critical. Another factor that should be taken into account is the finite time needed by the anemometer to reach equilibrium after a switch of overheat. As shown in the preceding chapter, equilibrium is usually

attained after $3ms$ but a residual oscillation may be present a little longer. After taking all these effects into account, the following compromise has been chosen: measurements were performed using 6 overheat steps of $20ms$ each, but only the last $15ms$ were used for the data processing.

The next step after choosing the number of wire overheats per wind tunnel run is to choose the overheat parameters themselves. This depends on the type of measurements to be performed. When an accurate determination of the three turbulence modes is to be obtained, a relative low value of $r = -F/G$ is necessary. This corresponds to a low value of the overheat parameter, as shown in figure 4.2. But fluctuation measurements at low overheat aren't free of drawback: the electronic noise is higher [31] and the frequency response lower [34] than for a high wire temperature. Consequently, if it is known that the fluctuation field is dominated by acoustic waves, it can be of interest to use higher values of the overheat parameter and to extrapolate the fluctuation diagram down to lower values of r since it is linear.

This is the approach that was followed within this work. The first measurements were performed using 6 overheat parameters ranging from $\tau = 0.05$ to $\tau = 0.5$ to evaluate the respective level of the three disturbances modes (see section 4.2.1). As it

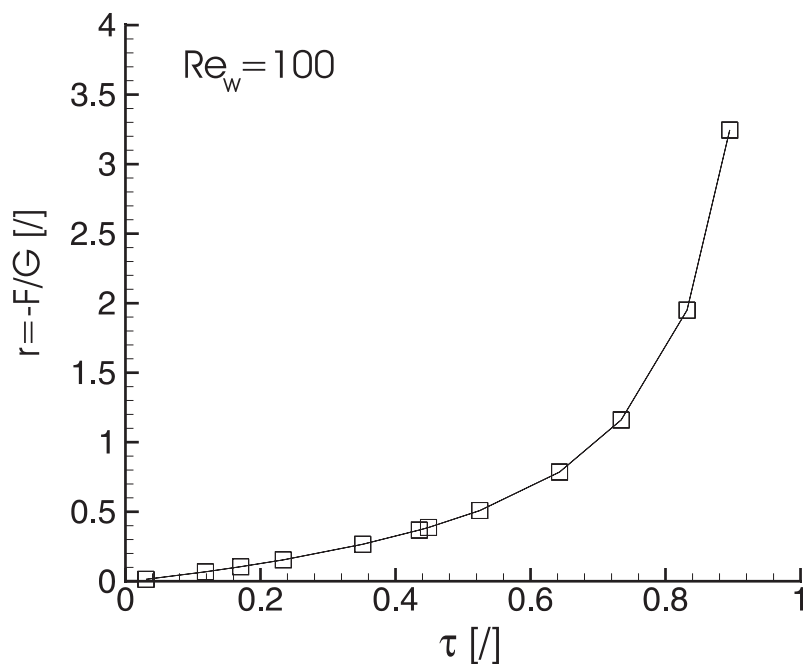


Figure 4.2: $r = -F/G$ as a function of τ

appeared that the acoustic mode was largely dominant, the following measurements were performed with $0.4 < \tau < 0.9$ to benefit from a better signal to noise ratio (see section 4.3).

4.1.3 Usable frequency range

The drawing of a fluctuation diagram requires the determination of Θ and thus a statistical evaluation of the root mean square e'_{rms} . Now e'_{rms} can be directly estimated from the time trace $e'(t)$ using the relation:

$$(e'_{rms})^2 = \frac{1}{T} \int_0^T e'(t)^2 dt. \quad (4.1)$$

Since $e'(t)$ is acquired digitally, equation 4.1 is expressed in the following discrete form:

$$(e'_{rms})^2 = \frac{1}{N} \sum_{i=0}^N e'(i\Delta t)^2, \quad (4.2)$$

where $N = T/\Delta t$ is the total number of samples and Δt the sampling period.

If e'_{rms} is estimated with equations 4.1 or 4.2, it represents a measure of the fluctuation energy in the whole frequency domain. In practice, the usable frequency range is restricted between a minimum value f_{min} and a maximum value f_{max} . In this case, using the discrete form of Parseval's relation [11], equation 4.2 becomes:

$$(e'_{rms}(f_{min}, f_{max}))^2 = \frac{1}{N^2} \sum_{i=N_{min}}^{N_{max}} \hat{G}_{e'}(i\Delta f), \quad (4.3)$$

where $\Delta f = T^{-1}$, $N_{min} = f_{min}/\Delta f$ and $N_{max} = f_{max}/\Delta f$. $\hat{G}_{e'}(f)$ refers to the power spectral density of $e'(t)$ and is estimated using a discrete Fourier transform (DFT).

The minimum frequency depends only on the integration time T during which $e'(t)$ is recorded and on the fluctuating signal. It is intuitive that any event the period of which is equal or greater than the integration time cannot be correctly estimated with one sample record. Since the AC output of the Cosytex CTA is filtered with a first order high pass filter of $1kHz$ cut-off frequency, and since low frequency fluctuations are not of primary interest, the minimum frequency was usually set to $f_{min} = 1kHz$ ¹.

¹The power spectral density near $1kHz$ was corrected to account for the $-3dB/dec$ fall of the AC output first order high pass filter.

The maximum usable frequency f_{max} is a function of the system's electronic noise. Since the electronic noise of a constant temperature anemometer is rising with the frequency, there is always a frequency after which it becomes dominant, and data processing above this frequency is therefore irrelevant [102]. Fortunately, this frequency f_{max} can be estimated from the signal's power spectrum since the electronic noise rises with the square of the frequency. This is illustrated in figure 3.8, page 55.

For a given frequency, the signal to noise ratio of a CTA increases with the wire temperature [39]. This means that measurements at a low overheat ratio lead to a relative low f_{max} , whereas a higher usable bandwidth can be obtained using a high overheat. For the analysis of a scanning sequence with different overheats, the maximum frequency f_{max} should be chosen considering the lowest overheat of the sequence and each overheat step should be analysed with the same bandwidth.

An underlying assumption for the use of the Cosytec scanning CTA is that the turbulent flow can be assumed to be a stationary random process. The hot-wire should "feel" the same flow conditions at different wire temperatures to extract information about the disturbance modes. Fortunately enough, the instationary pressure drop in the SWK is extremely low due to the large diameter of the driver tube and the nozzle suspension (see chapter 2), so that this assumption is usually verified. But some quasi-stationary fluctuating compression waves (with very low frequency) have been localized in the Mach rhombus. These waves will be investigated in a further section but an example of the corresponding time traces, obtained with a high wire temperature, is presented in figure 4.3. It is clear that such a process cannot be

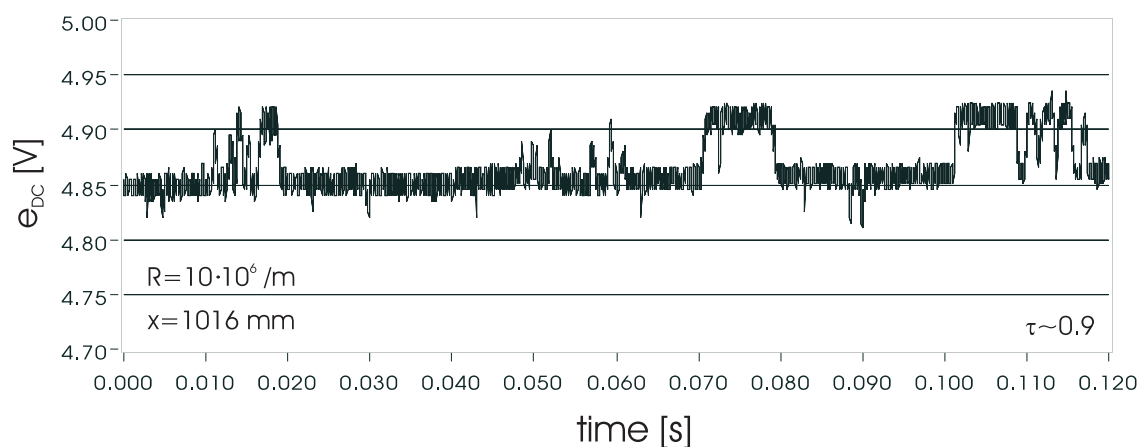


Figure 4.3: Fluctuating compression waves near Mach rhombus tip

investigated using a scanning sequence.

4.1.4 Measurement accuracy

It was shown in section 3.2 that the accuracy of the modal analysis directly depends on the position accuracy of the points $(r, \Theta)_i$ in the fluctuation diagram. When an uncertainty $\sigma(\Theta)$ and $\sigma(r)$ is known for each points, the accuracy of the result is an output of the regression algorithm ². An investigation of the measurement accuracy requires therefore an uncertainty estimate of these two parameters.

There are three main uncertainty sources for the present measurements:

- uncertainty in the stagnation conditions,
- uncertainty in the calibration coefficients,
- uncertainty in the measurement of $\langle e \rangle$ itself.

The uncertainty in the stagnation conditions doesn't play an important role for the fluctuation measurements since only relative fluctuating quantities $\langle x \rangle = x'_{rms}/\bar{x}$ are measured. A small error in the stagnation conditions results only in a small error in the estimation of the calibration coefficients F and G which is in any case smaller than their inherent uncertainty (section 3.5.2).

The uncertainty in F and G plays a role for the estimation of $\Theta = -\langle e \rangle / G$ and of course $r = -F/G$, but it refers to a *systematic* error and therefore should not be taken into account in $\sigma(\Theta)$ and $\sigma(r)$, which concern only *random* errors. In other words, $\sigma(\Theta)$ is only function of $\sigma(\langle e \rangle)$ and $\sigma(r) = 0$. To check the influence of the uncertainty in F and G , different fluctuation diagrams are plotted with their minimum and maximum values (from figure 3.13) and the results are compared (see section 4.2.2).

The uncertainty in the determination of $\langle e \rangle$ is by far the highest and is inherent in the nature of the measurements: $e'(t)$ is a stochastic process which properties are to be estimated statistically. However, as already pointed out in section 4.1.2, an accurate statistical estimation requires a long integration time, and this condition cannot be obtained in a short duration wind tunnel! In addition, due to a relative small signal to noise ratio, the usable bandwidth for the present measurements is quite small, and this makes the statistical estimation of $\langle e \rangle$ even more critical.

²Such an algorithm is comparatively easy to implement only if $\sigma(r)/r \ll \sigma(\Theta)/\Theta$. It will be shown that this is the case for the present measurements.

The statistical error in the estimation of $\langle e \rangle$ can be computed using the following simplified analysis, which is adapted from reference [9]. First of all, recall from equation 4.3 that e'_{rms} is computed as a sum of $n = N_{max} - N_{min}$ components of the estimated power spectral density function $\hat{G}_{e'}(f)$. Now $\hat{G}_{e'}(f)$ is defined as $\hat{G}_{e'}(f) = 2 | \hat{S}_{e'}(f) |^2$ where $\hat{S}_{e'}(f)$ refers to the discrete Fourier transform of $e'(t)$, which is a discrete form of the finite Fourier transform defined as:

$$S_{e'}(f, T) = \int_0^T e'(t) e^{-j2\pi ft} dt. \quad (4.4)$$

The true power spectral density function is defined as:

$$G_{e'}(f) = 2 \lim_{T \rightarrow \infty} \frac{1}{T} E[|S_{e'}(f, T)|^2], \quad (4.5)$$

where $E[...]$ refers to the mathematical expectation.

According to Bendat & Piersol [9], $\hat{G}_{e'}(f)$ is an inconsistent estimate of the power spectral density function $G_{e'}(f)$. Moreover, each frequency component $\hat{G}_{e'}(f)/G_{e'}(f)$ is a random variable which sampling distribution is equal to $\chi_2^2/2$, where χ_2 is the chi-square variable with 2 degrees of freedom. Now if one assumes that $G_{e'}(f)$ is approximately constant in the usable frequency range, the sampling distribution for the sum of n components of $\hat{G}_{e'}(f)$ and thus for e'_{rms} is equal to $\chi_{2n}^2/2$, since $\chi_a^2 + \chi_b^2 = \chi_{a+b}^2$. Recalling that the mean and variance of the chi-square variable with m degrees of freedom are m and $2m$ respectively, the normalized error for e'_{rms} can be written:

$$\epsilon(e'_{rms}) = \frac{\sigma(e'_{rms})}{e'_{rms}} = \frac{1}{\sqrt{n}}, \quad (4.6)$$

where $n = N_{max} - N_{min}$.

Since the integration time is much more critical for the estimation of e'_{rms} than for the mean value \bar{e} , it can be assumed that $\epsilon(\langle e \rangle) \sim \epsilon(e'_{rms})$. It can also be easily shown that $n = B_e T$, where T is the integration time and B_e the usable bandwidth. The relative uncertainty in $\langle e \rangle$ is then given by:

$$\epsilon(\langle e \rangle) = \frac{\sigma(\langle e \rangle)}{\langle e \rangle} = \frac{1}{\sqrt{B_e T}}. \quad (4.7)$$

This value can be substantial: for example, the usable frequency range for the measurements at low overheat ratio (see next section) is $B_e = [1kHz, 10kHz]$. For $T = 15ms$, it corresponds to $\epsilon(\langle e \rangle) = 8.6\%$.

Since $\Theta = - \langle e \rangle / G$ and since the uncertainty in G refers to a systematic error, $\sigma(\Theta)$ is given by:

$$\sigma(\Theta) = \epsilon(\langle e \rangle) \Theta. \quad (4.8)$$

4.2 Disturbance modes in the SWK

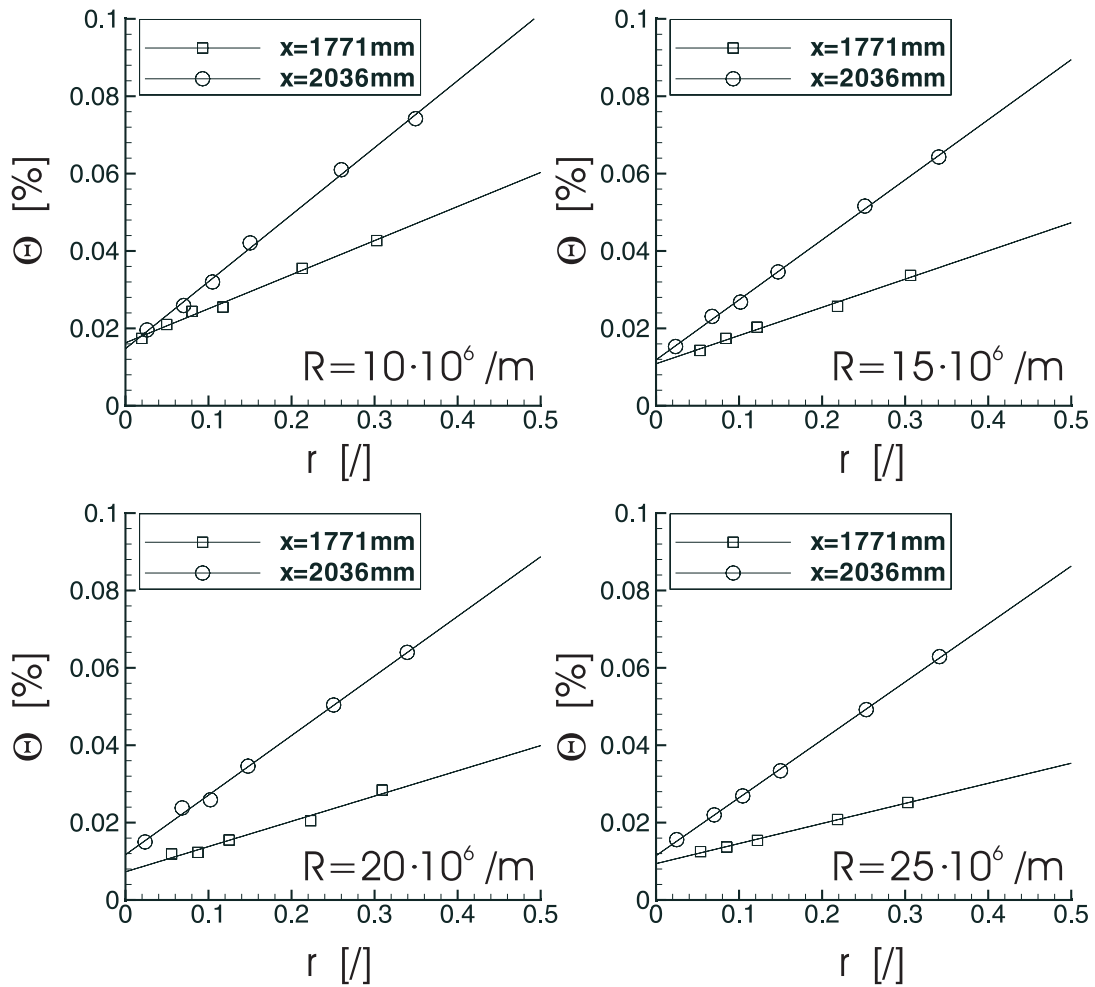
4.2.1 Experimental results

The disturbance modes in the SWK are identified by using the fluctuation diagram technique with an overheat parameter ranging from $\tau = 0.05$ to $\tau = 0.5$. Measurements were carried out at two positions near the middle of the Mach rhombus ($x = 1771mm$ and $x = 2036mm$, respectively), and at four different values of the unit Reynolds number (10, 15, 20 and 25 million per meter, respectively). The resulting fluctuation diagrams are presented in figure 4.4. For $x = 1771mm$ and $R \geq 15 \cdot 10^6/m$, the lowest overheat step of the scanning sequence couldn't be used in the data processing because of a strong electrical oscillation (see section 3.3.1 and ref. [103]).

Each wind tunnel run was performed at least 15 minutes after the filling of the driver tube, so that the loading conditions were as calm as possible. Examination of the signal to noise ratio allowed data analysis in the bandwidth $B_e = [1kHz, 10kHz]$.

The fluctuation diagrams in figure 4.4 seem to be well fitted by a straight line, thus demonstrating the dominance of acoustic disturbances in the free stream of the SWK, as showed in section 3.2.1. It is of course only an approximation: vorticity and entropy fluctuations generated during the driver tube's filling process are certainly present in the flow. Therefore, fitting the fluctuation diagram to a straight line simply ignores these residual disturbances. A less restrictive approach would be to assume that the three disturbance modes are uncorrelated and to fit the data to a hyperbola, as presented in section 3.2.2. When such a fit is performed, it appears that the mean squares error is sometimes even lower than for the straight line, a result that could at first be interpreted as a "better fit". This is not true: by fitting the data to a hyperbola, one degree of freedom is lost and the "fit's quality" cannot be tested so easily [68]. Moreover, the hyperbolic fit often leads to unrealistic results such as negative vorticity or entropy fluctuations, and even when the hyperbolic fit supplies plausible results for $\langle u_{rot} \rangle$ and $\langle (T_0)_s \rangle$, they are at least an order of magnitude lower than $\langle p \rangle$.

Consequently, the fluctuation diagrams presented in figure 4.4 can definitely be fitted to a straight line. The resulting disturbance field in the test section of the SWK is therefore largely dominated by acoustic waves, as in common conventional supersonic wind tunnels. The absence of well defined conditions upstream of the nozzle after the filling process of the driver tube doesn't induce any measurable

Figure 4.4: Fluctuation diagrams, $0.05 < \tau < 0.5$

vorticity or entropy fluctuation as long as the air in the driver tube is allowed to equilibrate. The fluctuation diagram's results are summarized in table 4.1

R [1/m]	x=1771mm		x=2036mm	
	$\langle \rho u \rangle$ [‰]	$\langle T_0 \rangle$ [‰]	$\langle \rho u \rangle$ [‰]	$\langle T_0 \rangle$ [‰]
$10 \cdot 10^6$	0.089	0.016	0.173	0.015
$15 \cdot 10^6$	0.073	0.011	0.156	0.012
$20 \cdot 10^6$	0.062	0.008	0.154	0.012
$25 \cdot 10^6$	0.051	0.010	0.147	0.012

Table 4.1: Summary of the fluctuation diagram's results, acoustic mode

4.2.2 Accuracy and repeatability

To check the measurement's repeatability, 10 identical wind tunnel runs were performed for $x = 1771\text{mm}$ and $R = 10 \cdot 10^6/m$. The normalized standard deviation of the mass flow and total temperature results for the 10 different runs were $\sigma_{exp}(\langle \rho u \rangle) / \langle \rho u \rangle = 7.5\%$ and $\sigma_{exp}(\langle T_0 \rangle) / \langle T_0 \rangle = 5.1\%$, whereas the calculated uncertainty was $\sigma(\langle \rho u \rangle) / \langle \rho u \rangle \sim 12\%$ and $\sigma(\langle T_0 \rangle) / \langle T_0 \rangle \sim 7\%$ respectively. The results appear therefore to be repeatable within the accuracy of the measurements, and the calculated uncertainty seems even to be slightly conservative.

The influence of small errors in the determination of the calibration coefficients was taken into account by performing a modal analysis with different values of F and G , corresponding to the minima and maxima defined in figure 3.13. In any case, the influence on the results was much smaller than the uncertainty reported above. At a first glance, it is rather surprising that relative large uncertainties in F and G have only a very small influence on the fluctuation diagram. This can however be rationalized by considering the definition of $\Theta = - \langle e \rangle / G$ and $r = -F/G$: G appears in the denominator of both Θ and r so that it doesn't have any large influence on the slope $d\Theta/dr$. F , however, only appears in r but its uncertainty is large only at low overheat ratio, so that its influence is restricted to the first points in the fluctuation diagram, where a large relative uncertainty results in a small absolute one. The corresponding influence on the linear fit is therefore very small ³.

4.2.3 Acoustic field properties

Once the dominance of acoustic disturbances in the fluctuation field has been established, some properties of the acoustic waves can be deduced following the method of Laufer [56]. Using equations 3.8 and 3.9, the pressure fluctuations and convection velocities of the waves can be calculated. They are plotted in figure 4.5.

According to figure 4.5, the sound intensity is decreasing with increasing unit Reynolds number, in accordance with the hypothesis of sound production by the turbulent boundary layer on the nozzle and sidewalls [3]. What is rather surprising is the large difference in fluctuation level between $x = 1771\text{mm}$ and $x = 2036\text{mm}$. Neither the local Mach number difference at the acoustic origin, nor the boundary

³It should be noted that the small influence of G on the results is emphasized by the linear character of the fit. A hyperbolic fit (measurement in a boundary layer, for example) would presumably be more sensitive.

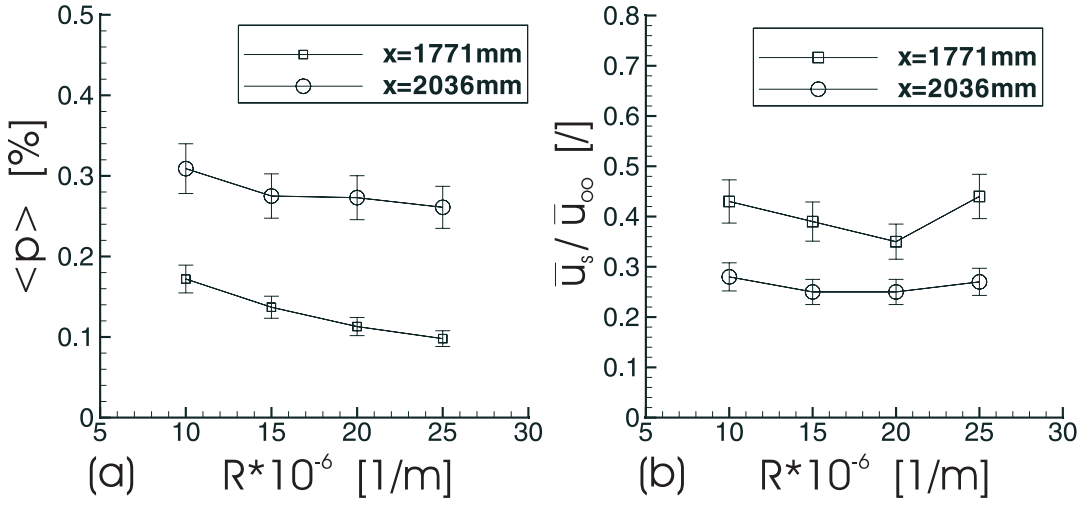


Figure 4.5: Acoustic fluctuations: (a) level, (b) source velocity

layer growth on the nozzle could account for such a difference, which is more than a factor 2 (*ie* a factor 4 in sound intensity). It is therefore believed that shivering Mach waves are superimposed to the eddy Mach waves for $x = 2036\text{mm}$. This hypothesis is supported by the character of the fluctuation diagrams in figure 4.4, where it can be seen that the intercept is approximately constant for the two positions. This is consistent with the work of Laufer [56], who showed that shivering Mach waves have a vanishing contribution to the fluctuation diagrams when r approaches 0.

Of course, it doesn't rule out the possibility of shivering Mach waves being already present at $x = 1771\text{mm}$, but a glance at the source velocity gives a further insight on the acoustic field characteristics. The experiments of Laufer [58] showed that the relative source velocity of eddy Mach waves should be approximately $\overline{u}_s / \overline{u}_\infty = 0.36$ at $Ma = 2.5$ (or even slightly higher). Any lower value of the measured source velocity imply that shivering Mach waves are present in the acoustic field. In the present case, the average value of the source velocity is $\overline{u}_s / \overline{u}_\infty = 0.40$ for $x = 1771\text{mm}$ and $\overline{u}_s / \overline{u}_\infty = 0.26$ for $x = 2036\text{mm}$. Since the value at $x = 1771\text{mm}$ is slightly higher than Laufer's value, it can be assumed that the corresponding fluctuation field is largely dominated by eddy Mach waves, whereas shivering Mach waves cannot be neglected at $x = 2036\text{mm}$.

The proportion of shivering Mach waves in the disturbance field at $x = 2036\text{mm}$ can be estimated by recalling that the second part of equation 3.8 yields a finite value of $\langle T_0 \rangle$ only when eddy Mach waves are present. Indeed, as shown by

Laufer [56], shivering Mach waves don't induce any total temperature fluctuation since their mean position is stationary with reference to the wind tunnel ⁴. Using equation 3.9, equation 3.8 can therefore be rewritten:

$$\langle p \rangle_{EMW} = \frac{1 - (\overline{u_s}/\overline{u_\infty})_{EMW}}{(\overline{u_s}/\overline{u_\infty})_{EMW}} \frac{\gamma}{\alpha(\gamma - 1)} \langle T_0 \rangle, \quad (4.9)$$

where $\langle p \rangle_{EMW}$ is the normalized pressure fluctuation due to eddy Mach waves only and $(\overline{u_s}/\overline{u_\infty})_{EMW}$ is the relative source velocity of the eddy Mach wave field. Equation 4.9 enables one to compute the part of the pressure fluctuations which is due to eddy Mach waves only using an estimate of their source velocity and the measured value of $\langle T_0 \rangle$.

Assuming a local source velocity of $(\overline{u_s}/\overline{u_\infty})_{EMW} = 0.40$ for the eddy Mach waves (this is equivalent as assuming a disturbance field composed of 100% eddy Mach waves at $x = 1771mm$), and an average stagnation temperature fluctuation of $\langle T_0 \rangle = 0.013\%$ at $x = 2036mm$, equation 4.9 yields $\langle p \rangle_{EMW} = 0.155\%$. Recalling that the average static pressure fluctuation is $\langle p \rangle = 0.279\%$, it means a proportion of 44% shivering Mach waves in the whole acoustic field at $x = 2036mm$.

It should be noted that the calculated values of $\overline{u_s}/\overline{u_\infty}$ are very sensitive to the assumption of dominant acoustic disturbances. If vorticity or entropy modes were not negligible, $\overline{u_s}/\overline{u_\infty}$ would be much larger than the values predicted by Laufer. The present results are therefore another proof that entropy and vorticity disturbances are negligible compared to acoustic disturbances.

4.2.4 Necessary waiting time after the filling process

As already explained above, the fluctuation diagrams presented in section 4.2.1 were obtained after a waiting time of at least 15 minutes after the end of the filling process, and it was shown that in this case, the disturbance field in the test section is largely dominated by sound waves: incoming disturbances from the driver tube are negligible compared to acoustic waves radiated from the nozzle and walls boundary layers. An interesting question, however, would be to know how long it is necessary to wait after each filling process, to ensure settled loading conditions in the driver tube and a repeatable disturbance field in the test section. In other words: how long is it necessary to wait to be sure to deal with a repeatable acoustic disturbance field?

⁴This is a direct consequence of the energy equation, which states that the total enthalpy is constant along a streamline for a *steady* adiabatic flow [95].

To answer this question, several wind tunnel runs were performed at different time after the filling of the driver tube and the fluctuation field was measured with a hot-wire at one position near the middle of the test section. The unit Reynolds number was $R = 20 \cdot 10^6/m$ and corresponded to a loading pressure of $2bar$, so that compressed air had to be filled in the tube to account for the $1bar$ pressure difference with atmosphere conditions. This was made at a maximal tank pressure of $60bar$ to ensure maximal effects in the test section.

Position in the test section was $x = 1771mm$ and the hot-wire was operated at a single overheat of $\tau \sim 0.8$, where it is both sensible to mass flow and total temperature fluctuations. Very low frequency fluctuations and a high stagnation temperature prevented the use of the modal analysis technique. The relative long measuring time ($120ms$) and high signal to noise ratio allowed a usable bandwidth of $B_e = [100Hz, 20kHz]$. The normalized effective output voltage fluctuation is presented in figure 4.6 as a function of the waiting time and some of the corresponding DC time traces are shown in figure 4.7.

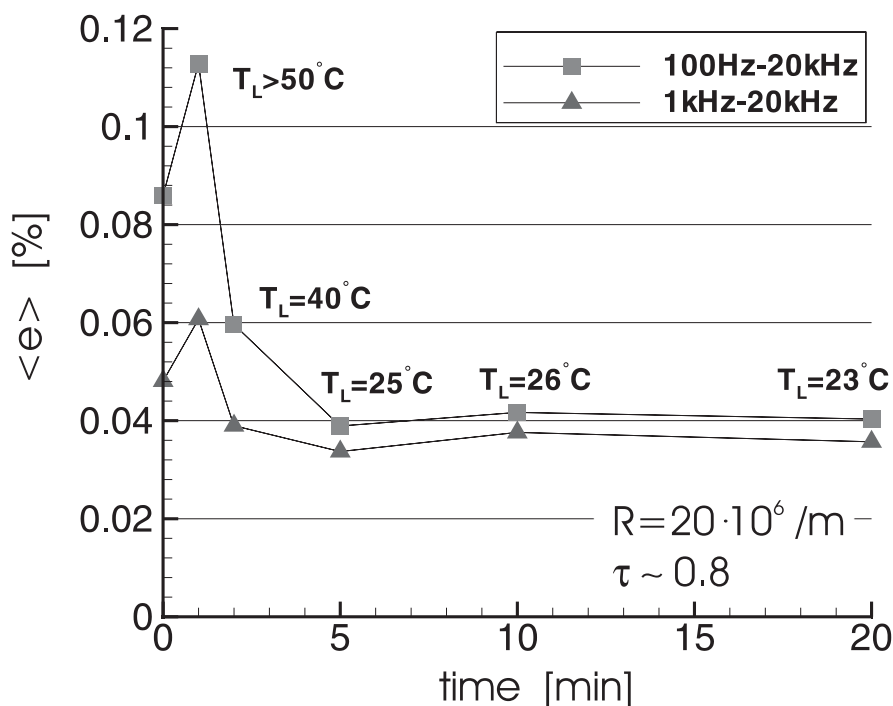


Figure 4.6: Normalized anemometer output voltage fluctuation ($t = 0$ corresponds to the end of the filling process)

It is shown in figure 4.6 that a high fluctuation level is present in the test section when

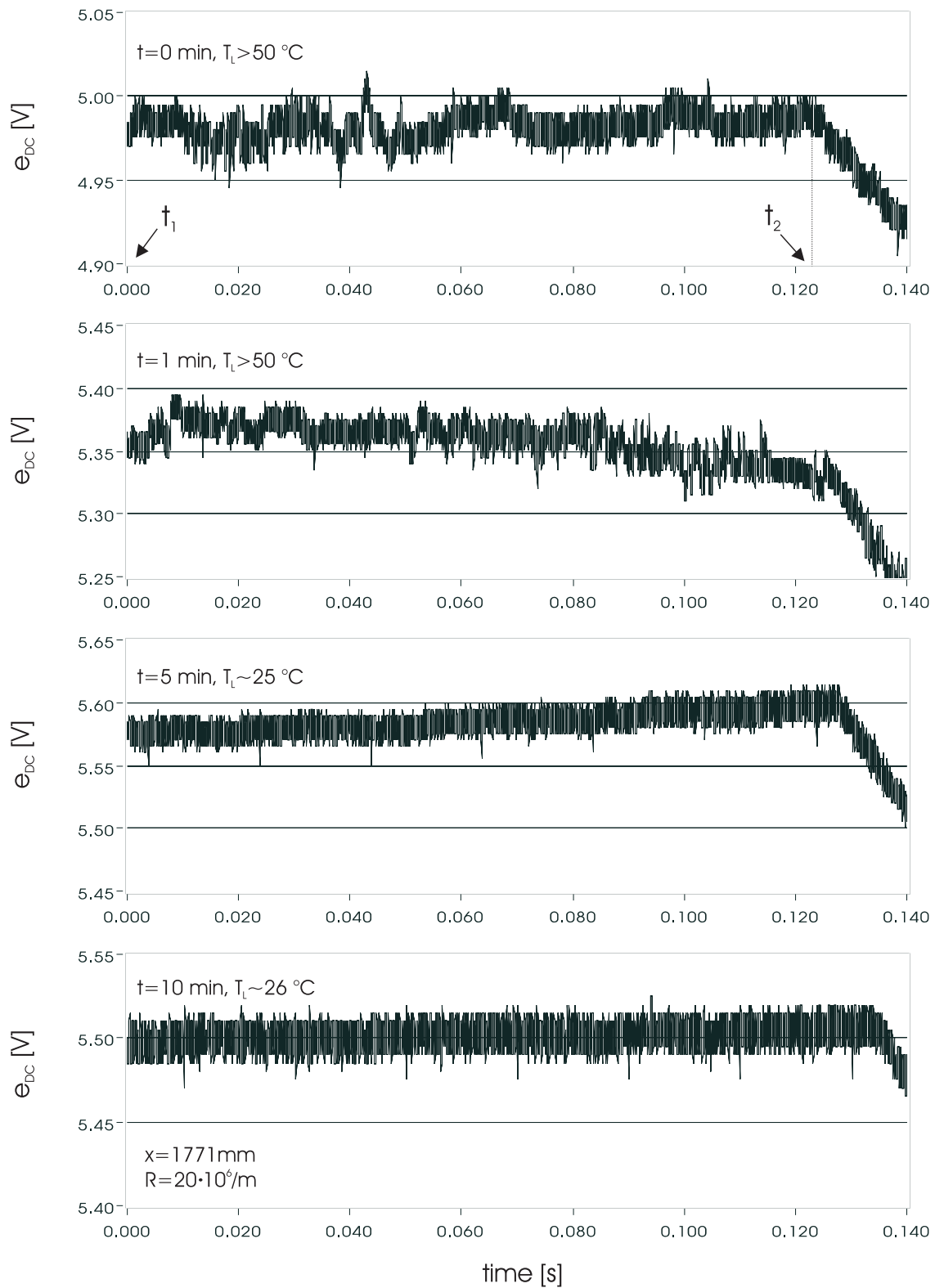


Figure 4.7: Time trace of the anemometer DC output voltage (t_1 : beginning of first quasi-steady state, t_2 : end of first quasi-steady state)

the wind tunnel run is performed just after the end of the filling process. Moreover, most of the energy is confined in the low frequency domain, an effect that can also be observed in the time traces in figure 4.7. In this case, temperature stratification in the driver tube lead to non-stationarity of the stagnation temperature. After 10 minutes waiting time, the effective voltage fluctuation can be considered as settled and it can be seen from figure 4.7 that the mean output voltage $\overline{e(t)}$ is constant during the whole quasi-steady state.

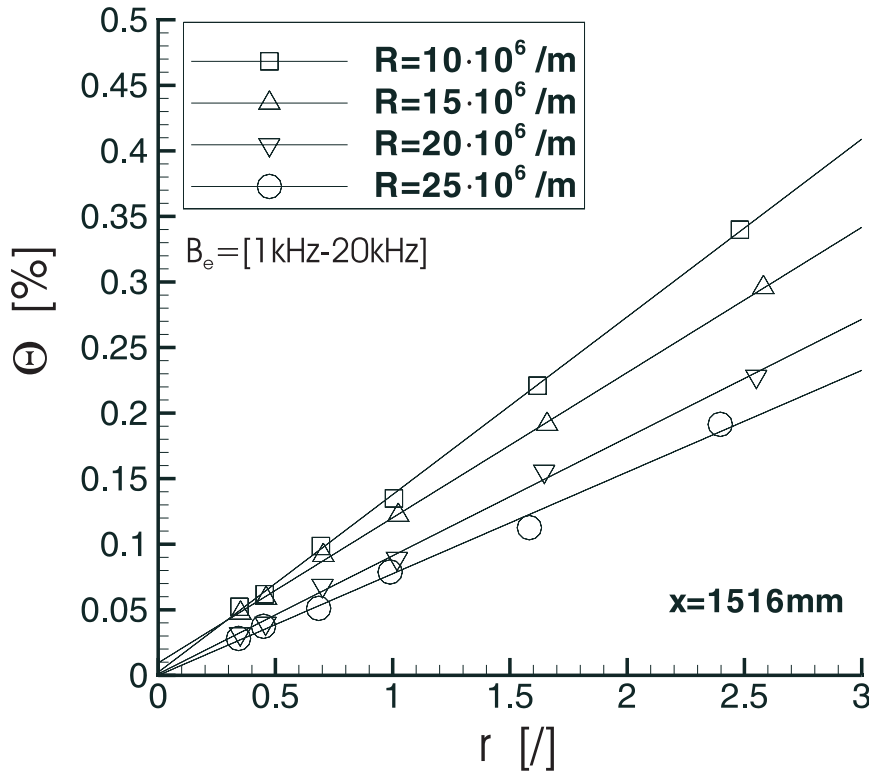
As a consequence, when the wind tunnel run is performed at least 10 minutes after the end of the filling process, a repeatable acoustic disturbance field is present in the test section.

4.3 Disturbance level along the nozzle centerline

Measurements reported in the last section have proven the dominance of acoustic disturbances in the test section of the SWK, like in conventional supersonic wind tunnels. These disturbances have their origin in the turbulent boundary layer of the nozzle and sidewalls of the test section, and are therefore highly dependent on the position in the Mach rhombus. This property has been verified by measuring a different level of pressure fluctuations at two positions near the middle of the test section. The next step for a thorough investigation of the wind tunnel's performance is a study of the disturbance level's evolution on the nozzle centerline, and is presented in this section.

Hot-wire measurements were carried out on the test section centerline for unit Reynolds numbers ranging from 10 to 25 million per meter. To benefit from a relative wide bandwidth, the modal analysis was performed with an overheat τ comprised between 0.4 and 0.9 and the resulting data was fitted to a straight line since the dominance of acoustic disturbances had already been established. Figure 4.8 shows an example of fluctuation diagrams for $x = 1516mm$.

Theoretically, such a method should allow the discrimination between eddy Mach waves and shivering Mach waves according to equation 4.9. Unfortunately, $\langle T_0 \rangle$ could not be estimated with enough precision for this purpose, because the data points in the fluctuation diagram are in this case too far from the vertical axis. Moreover, low frequency disturbances prevented the use of the fluctuation diagram technique at several positions and the anemometer had to be used without overheat scanning. In this case, the pressure fluctuations could still be estimated by choosing a high overheat ($\tau \sim 0.9$) and assuming negligible total temperature fluctuations.

Figure 4.8: Fluctuation diagrams, $0.4 < \tau < 0.9$

The normalized effective pressure fluctuation $\langle p \rangle$ along the test section axis is presented in figure 4.9. Although most of the points are situated over the "quiet" limit defined as $\langle p \rangle = 0.1\%$, some aren't far away: even as far downstream as $x = 1771\text{mm}$, the acoustic level is almost quiet for $R = 25 \cdot 10^6 / \text{m}$. What is striking, however, is the irregularity of the progression along the x-axis: both very strong peaks as well as calmer zones can be observed in the whole domain.

The general trend is a decrease of the fluctuation level with increasing unit Reynolds number, which is characteristic for a turbulent boundary layer on the nozzle and the sidewalls of the test section. No sign of laminar-turbulent transition of the nozzle boundary layer (which would induce a qualitative change in the progression $\langle p(x) \rangle$ with increasing unit Reynolds number [2, 13]) can be noticed. Although the boundary layer is turbulent, the disturbance level stays relative low because of the moderate Mach number and the short expansion nozzle [3].

The three peaks numbered (1) to (3) correspond to very low frequency disturbances superimposed to the background noise. An example of time trace obtained at peak

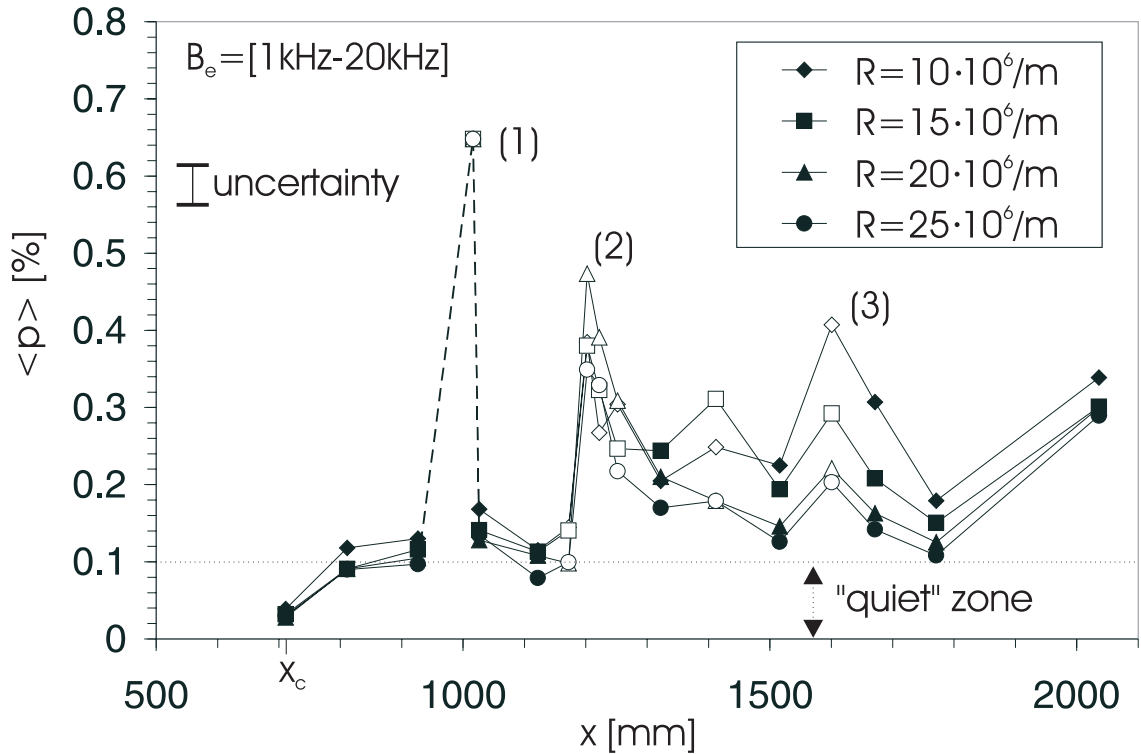


Figure 4.9: Normalized effective static pressure fluctuation in the SWK's test section, $Ma = 2.54$; filled symbols: Cosytec bridge with scanning, $0.4 < \tau < 0.9$; open symbols: Cosytec bridge without scanning, $\tau \sim 0.9$; dotted line: see text

(1) ($x = 1016\text{mm}$) was shown in figure 4.3 and suggests that a compression wave travels back and forth on the hot-wire sensor. It is evident from figure 4.3 that the effective output voltage fluctuation e'_{rms} is not a good measure of the corresponding disturbance level since this value depends largely on how many times the wave passes on the sensor during a wind tunnel run. Now the fluctuation frequency of the wave appears to be very low, so that this number of times vary from run to run and leads to non-repeatable results for e'_{rms} . Since this phenomenon appeared at each unit Reynolds number, it was decided to average the results and draw the corresponding effective pressure fluctuation in figure 4.9 in dotted line.

Interestingly, the peak No.(1), which is by far the strongest, had already been detected in previous works [78, 51], and seems to have its origin in the convex part of the nozzle contour, just downstream of the throat. Indeed, a comparable disturbance was discovered in a smaller supersonic wind tunnel at IAG (EMS), which

nozzle follows the same geometry as the SWK's (see references [46], [79], and [64]). These recent results suggest that this large quasi-stationary disturbance is more a property of the Laval nozzle than of the wind tunnel itself. It is believed to be caused by a slight disadjustment of the nozzle blocks, which induces an incomplete extinction of incoming waves from the sonic line [51].

Apart from peak No.(1), two smaller peaks have been discovered on the SWK's centerline. Examination of the corresponding time traces showed some similarity with peak No.(1), but with much smaller intensity. These peaks, as well as the general irregularity of figure 4.9 and the results presented in last section, suggest that the disturbance field is dominated by highly localized shivering Mach waves superimposed to a background of eddy Mach waves. This hypothesis can be verified by comparing figure 4.9 with the measurements of mean flow disturbances performed by Riedel [78], and reproduced in figure 4.10.

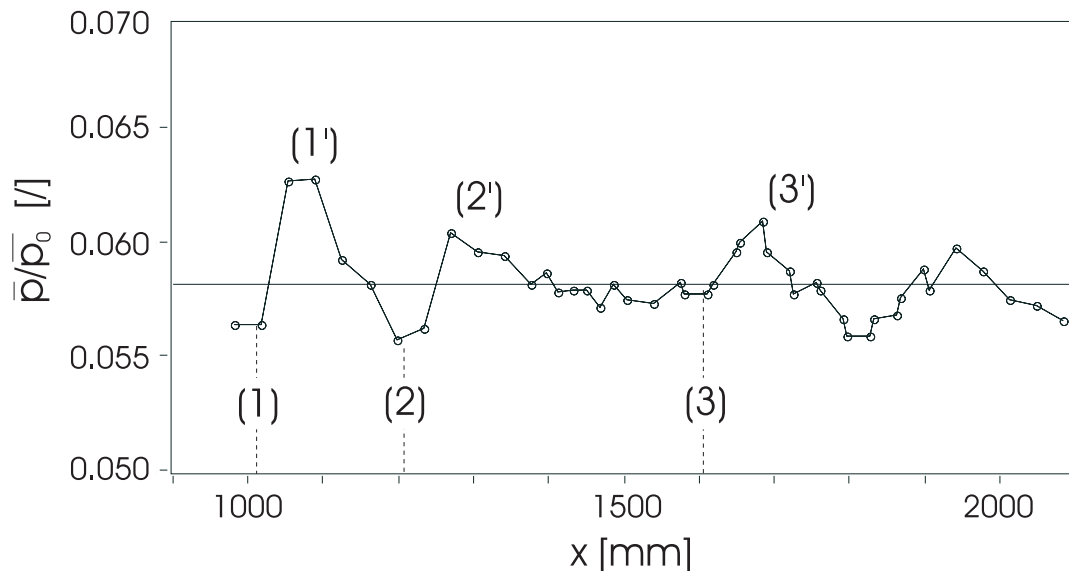


Figure 4.10: Mean static pressure disturbances in the SWK test section, taken from Riedel [78]. The numbers without prime correspond to the peaks from figure 4.9.

It appears that the mean flow disturbances follow a comparable trend, with three distinctive peaks along the x-axis (prime numbers). These peaks correspond to local excess pressure zones and are situated a little downstream of the peaks from figure 4.9, so that the strong fluctuating disturbances can be related to the beginning of a local pressure rise. This shows that a large part of the fluctuating pressure disturbances are in fact steady compression waves "shivered" by the turbulent boundary

layer on the nozzle and sidewalls. This result can be compared with the work of Anders *et al.* [2], who also found a high degree of correlation between mean flow and fluctuating disturbances in two axisymmetric Mach 5 test sections.

4.4 Power spectra

An investigation of free stream disturbances in the SWK's test section wouldn't be complete without an analysis of their spectral energy distribution, which is an important parameter influencing boundary layer transition on models.

Some representative power spectra are presented in figure 4.11. They were directly obtained by a standard FFT of the measured time trace and take into account the anemometer's frequency response and AC coupling high-pass filter (*ie* the spectra were computed after post-processing of the measured signals). The spectra are presented *without any averaging* in the frequency domain. Indeed, a measurement time of $15ms$ corresponds to a frequency resolution of $66.7Hz$, which is far too high to enable any averaging since most of the interesting features in the spectral distributions happen at a relative low frequency.

Apart from the contribution of electronic noise, the spectral distributions at $x = 1771mm$ (spectra (a) and (b)) show a trend similar to Laufer's data (see figure 2.5, page 32) and thus corroborate the previous conclusion of a sound field dominated by eddy Mach waves. The similarity is even quantitative since the frequency corresponding to maximum energy is approximately $2 - 3kHz$ in the present case, whereas a rough estimation from figure 2.5 yielded $4kHz$.

At $x = 1601mm$ (c), low frequency oscillations are superimposed to the previous spectral distribution, and at $x = 1202mm$ (d), the low frequency part of the distribution is largely dominant. These two positions correspond respectively to peaks (3) and (2) in figure 4.9 and confirm the conclusion of last section, namely that local shivering Mach waves are superimposed to the bulk of eddy Mach waves. Moreover, when shivering Mach waves are present, the total energy content is shifted to lower frequencies, as predicted by Morkovin [67].

The influence of the unit Reynolds number on eddy Mach wave radiation can be observed by comparing respectively spectra (a) with (b) and (e) with (f). With increasing R , the thickness of the nozzle boundary layer decreases, thus leading to an increase of the radiated frequency [3]. Furthermore, the boundary layer thickness is much smaller near the throat, so that the peak frequency at $x = 811mm$ is higher than at $x = 1771mm$.

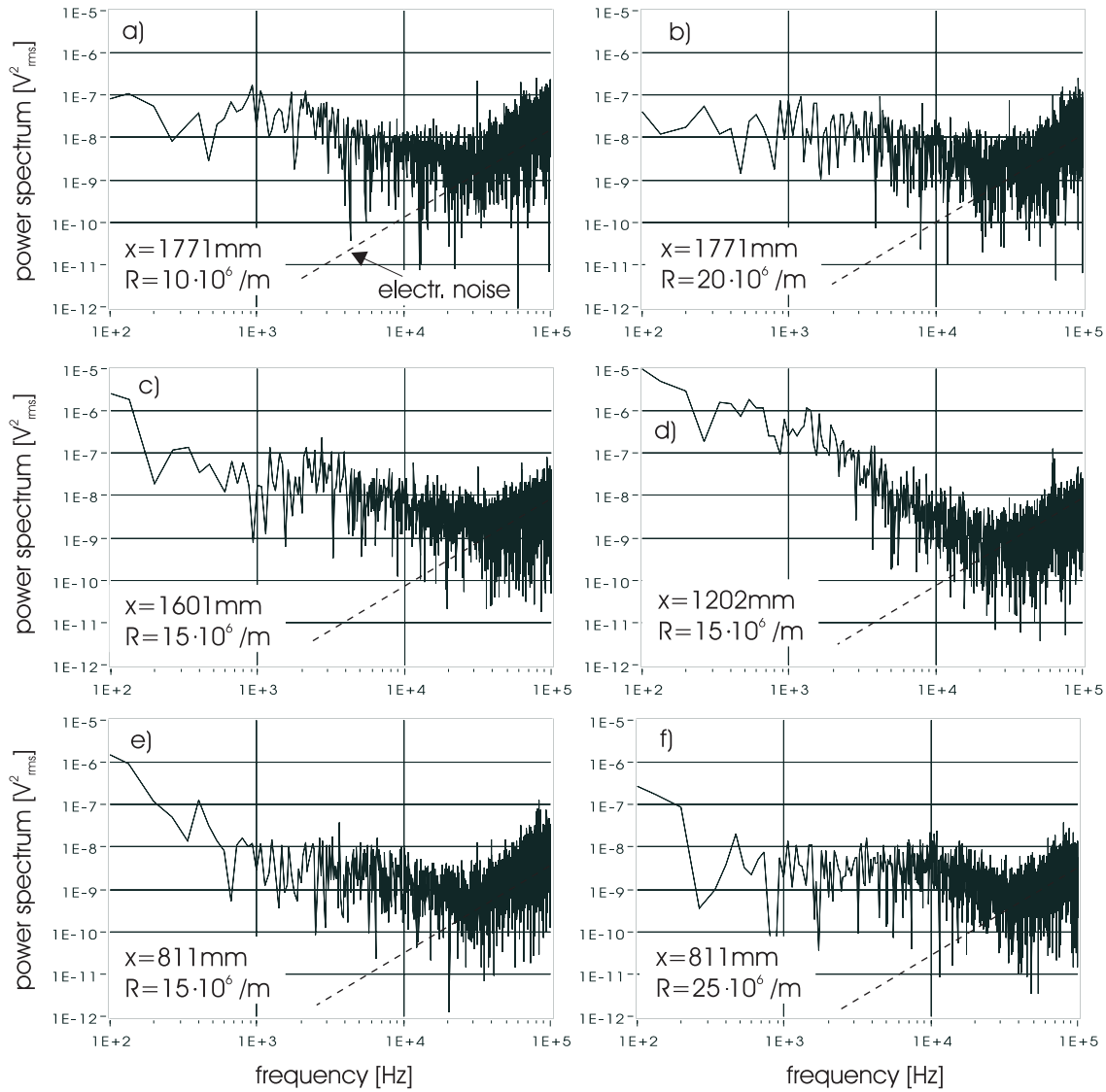


Figure 4.11: Representative power spectra, SWK's nozzle centerline

It is interesting to notice that in any case, the maximum energy of the distribution is at least an order of magnitude higher than at the frequency at which the electronic noise becomes dominant ($\sim 20 - 30\text{kHz}$). It means that although the bandwidth is inherently limited due to the anemometer's electronic noise, it is sufficient to capture the most part of the fluctuating disturbances. An estimation based on representative spectral distributions showed that at least 95% of the energy is present under 30kHz in the whole Mach rhombus. At the most downstream positions, this limit even decreases to 20kHz .

4.5 Possible improvement of the test section flow

The results presented in last sections have shown that the free stream disturbance field in the SWK is dominated by acoustic waves originating in the turbulent boundary layer on the nozzle and sidewalls. This includes the truly aerodynamic sound produced by the turbulent flow and radiated in the form of eddy Mach waves, as well as quasi-stationary pressure waves shivered by the boundary layer. The level of eddy Mach wave radiations is relatively low compared to other supersonic facilities, because of the low nominal Mach number and the rapid expansion nozzle. Moreover, the large size of the tunnel results in low frequency disturbances which are relatively independent on the unit Reynolds number. These results are in accordance with the ones of Beckwith [7] and Pate & Schueler [69], and suggest that the SWK should be particularly advantageous for laminar-turbulent transition experiments, as already pointed out by Riedel [78].

One handicap of this wind tunnel is the presence of highly localized mean flow disturbances which result in a large amount of shivering Mach waves in the whole fluctuation field and in an irregular progression of the pressure disturbances along the x-axis. These disturbances can trigger the transition process in the model boundary layer and lead to transition Reynolds number lower than expected. They can also induce the so-called unit Reynolds number effect (*ie* a variation of the transition Reynolds number with unit Reynolds number) since they don't scale with the unit Reynolds number whereas the model boundary layer does. Consequently, the elimination of these mean flow disturbances would result in a great improvement of the test section flow.

Figure 4.12 shows an estimation of how the pressure fluctuations on the nozzle centerline would look like if the shivering Mach waves were not present. It was obtained by assuming that the actual proportion of eddy Mach waves in the present measurements at $x = 1771mm$ is 100%, and that the acoustic intensity on the nozzle centerline is proportional to the fourth power of the local Mach number at the corresponding acoustic origin on the nozzle [56]. The contribution of the sidewalls and the boundary layer thickness was neglected. It seems to be a consistent approximation since the nominal Mach number is attained farther upstream on the sidewall centerline as on the nozzle, and since the fourth power law already contains a boundary layer thickness contribution [73]. The local Mach number on the nozzle was computed by Smorodsky [90] using the method developed by Schwarz [85].

The resulting curve appears to be a lower envelope of the measured pressure fluctuation level. It can be interpreted as the minimum disturbance level that is possible to

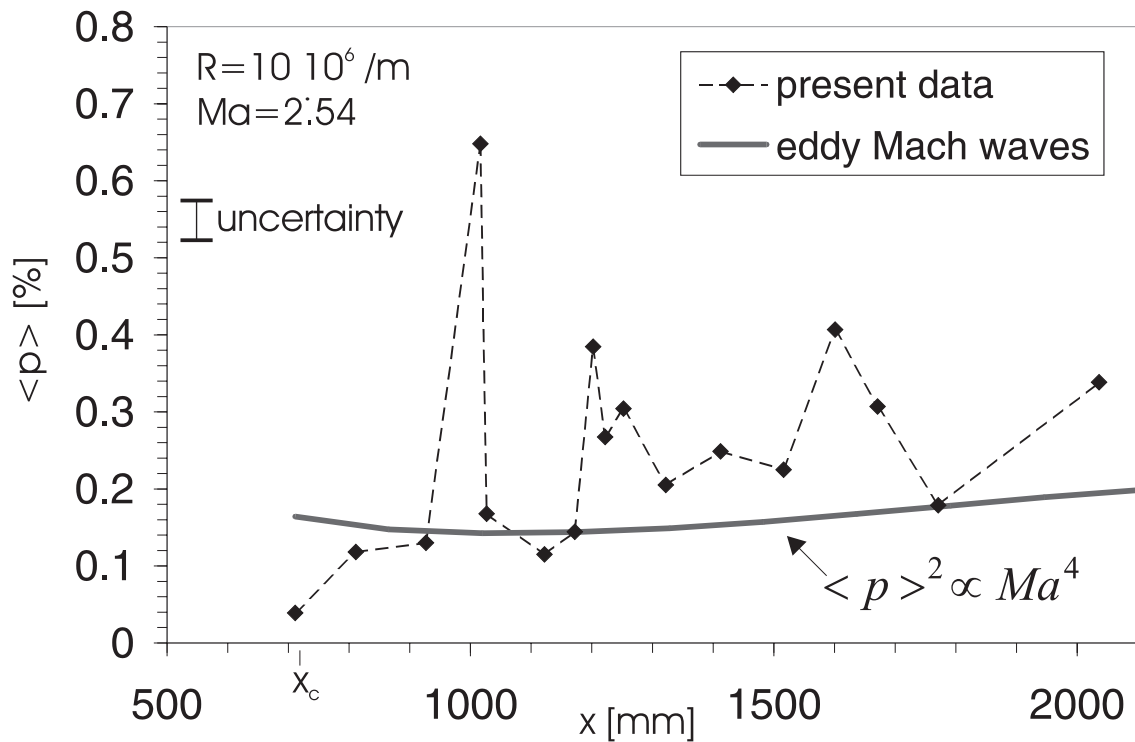


Figure 4.12: Estimation of the proportion of eddy Mach waves in the disturbance field

achieve in the SWK if the boundary layers on the nozzle and sidewalls are turbulent. The estimation is quite consistent with the experimental results since it predicts a proportion of 44% shivering Mach waves at $x = 2036\text{mm}$, which is exactly the same value as that obtained with equation 4.9. Taking into account the finite accuracy of the measurements as well as the simplicity of the present estimation, it is a rather gratifying result.

It is noteworthy that the predicted proportion of eddy Mach waves at $x = x_c = 711\text{mm}$ is much larger than the actual noise level. This could be the evidence of a very small portion of laminar boundary layer on the nozzle. This suggestion should however be taken with great care since this position corresponds to the tip of the Mach rhombus, the acoustic origin of which is at the throat and is associated with a very thin boundary layer. In any case, the resulting "quiet core" would be too small to have any practical interest.

The question if such a minimum disturbance level is achievable in practice stays open. A reduction of the stationary pressure waves traveling in the test section should possibly be obtained by improving the nozzle surface quality and/or the

contour accuracy. Recent investigations in a smaller wind tunnel (EMS) indeed revealed a clear correlation between a better surface quality and a decrease in the free stream disturbance level [64]. In any case, the improvements should be tested in a smaller wind tunnel before any modification of the SWK's nozzle.

Chapter 5

Conclusion

The present work investigates the free stream disturbance field in the test section of the SWK, a short duration supersonic wind tunnel of the *Institut für Aerodynamik und Gasdynamik* at Stuttgart University. The primary interest lies in the connection between this disturbance field and the results of laminar-turbulent transition experiments.

Measurements were performed using a specially designed constant-temperature hot-wire anemometer, which enables an automatic scanning of the wire temperature, to be able to perform a complete modal analysis within one wind tunnel run.

A new experimental procedure was developed to operate this anemometer in the SWK, and, more generally, to extend the usual CTA operation in facilities with limited testing time. It is based on digital post-processing of hot-wire results obtained with a non-optimized bridge. This is a necessary condition to use an anemometer with automatic scanning of wire temperature, and it was made possible by the development of a very fast electrical test to measure the whole anemometer transfer function within several milliseconds.

The *in situ* calibration of the anemometer was performed in the SWK, parallel to the fluctuation measurements. A particular attention was paid to the determination of the real overheat parameter, and a second order development of the anemometer response to temperature fluctuations showed that a complete modal analysis down to low overheat parameters is allowed in the present case of free stream disturbances.

Experimental results showed the dominance of acoustic disturbances in the SWK's test section. Vorticity and entropy modes are negligible compared to the acoustic field if the air in the driver tube is allowed to equilibrate at least 10 minutes after the filling process. As a consequence, the disturbance field is repeatable from run to run, and doesn't depend on the filling conditions of the driver tube.

Experiments didn't reveal any evidence of laminar-turbulent transition on the supersonic parts of the nozzle and sidewalls, so that the nozzle boundary layer is believed to become turbulent just downstream of the throat (or even upstream), for unit Reynolds numbers greater than 10 million per meter.

The large size of the test section results in the concentration of fluctuating energy in the low frequency part of the spectrum: it is estimated that at least 95% of the energy is present under $30kHz$, with a peak frequency ranging from $10kHz$ at the tip of the Mach rhombus to $3kHz$ at the most downstream position.

Beside eddy Mach wave radiation from the turbulent nozzle and sidewall boundary layers, the disturbance field is characterized by highly localized shivering Mach waves which may be caused by imperfections of the nozzle contours or roughness elements. These disturbances are also related to mean flow perturbations across the test section. Hot-wire measurements showed that the normalized pressure fluctuation due to eddy Mach waves only stays below 0.2% in the whole Mach rhombus, whereas total Mach waves fluctuations can reach 0.5% or even more in the case of quasi-steady compression waves running through the test section.

Consequently, the flow quality could be greatly improved by eliminating the mean flow disturbances, thus reducing the share of shivering Mach waves in the whole acoustic field. In this case, even with a turbulent nozzle boundary layer, the SWK should be remarkably advantageous for laminar-turbulent transition experiments, due to its relative low disturbance character, its large size, and its economic mode of operation.

Bibliography

- [1] T. J. Alcenius, S. P. Schneider, I. E. Beckwith, J. A. White, and J. J. Korte. Development of Square Nozzles for Supersonic Low-Disturbance Wind Tunnels. *Journal of Aircraft*, 33(6):1131–1138, 1996.
- [2] J. B. Anders, P. C. Stainback, and I. E. Beckwith. A New Technique for Reducing Test Section Noise in Supersonic Wind Tunnels. AIAA paper 78-817, 1978.
- [3] J. B. Anders, P. C. Stainback, and I. E. Beckwith. New Technique for Reducing Test Section Noise in Supersonic Wind Tunnels. *AIAA Journal*, 18(1):5–6, 1980.
- [4] E. Arzoumanian and J. F. Debieve. Un processus programmé en anémométrie à fil chaud en écoulement supersonique. *L'onde électrique*, 70(2):54–59, 1990.
- [5] I. E. Beckwith. Development of a High Reynolds Number Quiet Tunnel for Transition research. *AIAA Journal*, 13(3):300–306, March 1975.
- [6] I. E. Beckwith, F. J. Chen, and M. R. Malik. Design and Fabrication Requirements for Low-Noise Supersonic/Hypersonic Wind Tunnels. AIAA paper 88-0143, 1988.
- [7] I. E. Beckwith, T. R. Creel, F. J. Chen, and J. M. Kendall. Free Stream Noise and Transition Measurements in a Mach 3.5 Pilot Quiet Tunnel. AIAA paper 83-0042, 1983.
- [8] I. E. Beckwith and C. G. Miller. Aerothermodynamics and Transition in High Speed Wind Tunnels at NASA Langley. *Annual Review of Fluid Mechanics*, 22:419–439, 1990.
- [9] J. S. Bendat and A. G. Piersol. *Random Data: Analysis and Measurement Procedures*. Wiley-Interscience, 1971.

- [10] E. R. Bergstrom and S. Raghunathan. Nonstationarity in Gun Tunnel Flows. *AIAA Journal*, 15(4):1362–1364, 1977.
- [11] R. Best. *Digitale Messwertverarbeitung*. Oldenbourg, 1991.
- [12] D. Bestion, J. Gaviglio, and J. P. Bonnet. Comparison between constant-current and constant-temperature hot-wire anemometers in high-speed flows. *Review of Scientific Instruments*, 54(11):1513–1524, 1983.
- [13] A. E. Blanchard, J. T. Lachowicz, and S. P. Wilkinson. NASA Langley Mach 6 Quiet Wind-Tunnel Performance. *AIAA Journal*, 35(1):23–28, 1997.
- [14] J. P. Bonnet. *Etude théorique et expérimentale de la turbulence dans un sillage supersonique*. PhD thesis, Université de Poitiers, 1982.
- [15] J. P. Bonnet and T. Alziary de Roquefort. Determination and optimization of frequency response of constant temperature hot-wire anemometers in supersonic flows. *Review of Scientific Instruments*, 51(2):234–239, 1980.
- [16] J. A. Borgos. A Review of Electrical Testing of Hot-Wire and Hot-Film Anemometers. *TSI Quarterly*, 6(3):3–9, 1980.
- [17] H. H. Bruun. *Hot-Wire Anemometry, principles and signal analysis*. Oxford University Press, 1995.
- [18] F. J. Chen, M. R. Malik, and I. E. Beckwith. On the Design of a New Mach 3.5 Quiet Nozzle. In M. Y. Hussaini and R. G. Voigt, editors, *Instability and Transition*, volume 2 of *ICASE/NASA LaRC*, pages 246–257. Springer Verlag, 1989.
- [19] G. Comte-Bellot. Hot-Wire Anemometry. *Annual Review of Fluid Mechanics*, 8:209–231, 1976.
- [20] G. Comte-Bellot. *The Handbook of Fluid Dynamics*, chapter 34: Hot-Wire Anemometry, pages 34.1–34.29. CRC Press, 1998.
- [21] G. Comte-Bellot and G. R. Sarma. Constant Voltage Anemometer Practice in Supersonic Flows. *AIAA Journal*, 39(2):261–270, 2001.
- [22] A. Demetriades. Roughness Effects on Boundary-Layer Transition in a Nozzle Throat. *AIAA Journal*, 19(3):282–289, 1981.

- [23] A. Demetriades. Cooling and Roughness Effects on Transition on Nozzle Throats and Blunt Bodies. *Journal of Spacecrafts and Rockets*, 29(4):432–436, 1992.
- [24] A. Demetriades. Stabilization of a Nozzle Boundary Layer by Local Surface Heating. *AIAA Journal*, 34(12):2490–2495, 1996.
- [25] A. Demetriades and T. Brogan. Influence of Sidewall Transition on Measured Free Stream Noise in a Two-Dimensional Supersonic Tunnel. AIAA Paper 98-2614, 1998.
- [26] J. E. Ffowcs Williams. The noise from turbulence convected at high speed. *Philosophical Transactions of the Royal Society A*, 255(1061):469–503, 1963.
- [27] J. E. Ffowcs Williams and G. Maidanik. The Mach wave field radiated by turbulent shear flows. *Journal of Fluid Mechanics*, 21(4):641–657, 1965.
- [28] L. M. Fingerson. Thermal anemometry, current state, and future directions. *Review of Scientific Instruments*, 65(2):285–300, 1994.
- [29] P. Freymuth. Über einige spezielle Probleme der Hitzdrahtmesstechnik. DLR Forschungsbericht 66-03, 1966.
- [30] P. Freymuth. Feedback Control Theory for Constant Temperature Hot-Wire Anemometers. *Review of Scientific Instruments*, 38(5):677–681, 1967.
- [31] P. Freymuth. Noise in Hot-Wire Anemometers. *Review of Scientific Instruments*, 39(4):550–557, 1968.
- [32] P. Freymuth. Frequency response and electronic testing for constant-temperature hot-wire anemometers. *Journal of Physics E: Scientific Instruments*, 10:705–710, 1977.
- [33] P. Freymuth. Engineering Estimate of Heat Conduction Loss in Constant Temperature Thermal Sensors. *TSI Quarterly*, 5(3):3–8, 1979.
- [34] P. Freymuth. The effect of varying resistance ratio on the behaviour of constant-temperature hot-wire anemometers. *Journal of Physics E: Scientific Instruments*, 14:1373, 1981.
- [35] P. Freymuth. *A Bibliography of Thermal Anemometry*. TSI Incorporated, 1992.

- [36] P. Freymuth. Second or third order control theory for constant-temperature hot-wire anemometers. *Experiments in Fluids*, 23:175–176, 1997.
- [37] P. Freymuth. On higher order dynamics of constant-temperature hot-wire anemometers. *Measurement Science and Technology*, 9:534–535, 1998.
- [38] P. Freymuth. Private communication, 2001.
- [39] P. Freymuth and L. M. Fingerson. Hot-wire anemometry at very high frequencies: effect of electronic noise. *Measurement Science and Technology*, 8:115–116, 1997.
- [40] U. Gaisbauer, H. Knauss, S. Wagner, and J. Weiss. Measurement techniques for the detection of flow disturbances and transition localization in a short duration wind tunnel. In A. M. Kharitonov, editor, *Proceedings of the International Conference on the Methods of Aerophysical Research*, Russian Academy of Sciences, Siberian Branch, Novosibirsk, Russia, pages 54–67, 2000.
- [41] U. Gaisbauer, H. Knauss, S. Wagner, and J. Weiss. The meaning of disturbance fields in transition experiments and their detection in the test section flow of a short duration wind tunnel. In S. Wagner, U. Rist, J. Heinemann, and R. Hilbig, editors, *New Results in Numerical and Experimental Fluid Mechanics III*, volume 77 of *Notes on Numerical Fluid Mechanics*, pages 403–410. Springer, 2000.
- [42] U. Gaisbauer, H. Knauss, J. Weiss, and S. Wagner. Experimentelle Untersuchungen an Verdichtungsflächen und Triebwerkseinläufen für Hyperschallflugkörper. SFB 295, TPC5, Arbeits- und Ergebnisbericht, pages 421–456, 2001.
- [43] J. Gaviglio. Sur les méthodes de l’anémométrie par fil chaud des écoulements compressibles de gaz. *Journal de Mécanique appliquée*, 2(4):449–498, 1978.
- [44] J. Gaviglio and J. P. Dussauge. On reduction of errors arising in hot-wire anemometry of thin turbulent shear layers. In *Proceedings of the Symposium on Flows in Open Channels and Closed Conduits*, Special Publication 484, National Bureau of Standards, Gaithersburg, MD, pages 649–659, 1977.
- [45] C. Gossweiler. *Sonden und Messsystem für schnelle aerodynamische Strömungsmessung mit piezoresistiven Druckgebern*. Dissertation ETH Nr. 10253, Eidgenössische Technische Hochschule, Zürich, 1993.

- [46] C. Hoffmann. Untersuchung des Strömungsfeldes und Detektion von Störfeldern bei 2-dimensionalen Eckenlavalaldüsen für $Ma=2.5$. Studienarbeit, IAG, Universität Stuttgart, 2000.
- [47] M. A. Kegerise and E. F. Spina. A comparative study of constant-voltage and constant-temperature hot-wire anemometers. Part I : The static response. *Experiments in Fluids*, 29:154–164, 2000.
- [48] M. A. Kegerise and E. F. Spina. A comparative study of constant-voltage and constant-temperature hot-wire anemometers. Part II : The dynamic response. *Experiments in Fluids*, 29:165–177, 2000.
- [49] A. L. Kistler. Fluctuation measurements in a supersonic turbulent boundary layer. *Physics of Fluids*, 2:290–296, 1959.
- [50] H. Knauss, U. Gaisbauer, R. Riedel, and S. Wagner. Experimentelle Untersuchungen an Verdichtungsflächen und Triebwerkseinläufen für Hyperschallflugkörper. SFB 295, TPC5, Finanzierungsantrag, pages 325-348, 1998.
- [51] H. Knauss, R. Riedel, and S. Wagner. The Shock Wind Tunnel of Stuttgart University. A Facility for Testing Hypersonic Vehicles. AIAA paper 99-4959, 1999.
- [52] A. D. Kosinov and V. V. Repkov. Design and application of CTA in supersonic flow. International Conference on the Methods of Aerophysical Research, unpublished, 1998.
- [53] A. D. Kosinov, N. V. Semionov, and Yu. G. Yermolaev. Disturbances in test section of T-325 supersonic wind tunnel. ITAM preprint No. 6-99, 1999.
- [54] L. S. G. Kovásznay. The hot-wire anemometer in supersonic flow. *Journal of the Aeronautical Sciences*, 17:565–584, 1950.
- [55] L. S. G. Kovásznay. Turbulence in Supersonic Flow. *Journal of the Aeronautical Sciences*, 20(10):657–682, 1953.
- [56] J. Laufer. Aerodynamic Noise in Supersonic Wind Tunnels. *Journal of the Aeronautical Sciences*, 28(9):685–692, 1961.
- [57] J. Laufer. Sound radiation from a turbulent boundary layer. In *Mécanique de la Turbulence*, Centre National de la Recherche Scientifique, pages 381–393, 1962.

- [58] J. Laufer. Some Statistical Properties of the Pressure Field Radiated by a Turbulent Boundary Layer. *The Physics of Fluids*, 7(8):1191–1197, 1964.
- [59] J. Laufer and R. McClellan. Measurements of heat transfer from fine wires in supersonic flows. *Journal of Fluid Mechanics*, 1:276–289, 1956.
- [60] J. Laufer, J. E. Ffowcs Williams, and S. Childress. *Mechanism of Noise Generation in the Turbulent Boundary Layer*. AGARDograph 90. NATO-AGARD, 1964.
- [61] V. A. Lebiga and A. Yu. Pak. Comparison of characteristics of anemometers of different types. In *Proceedings of the International Conference on the Methods of Aerophysical Research*, Russian Academy of Sciences, Siberian Branch, Novosibirsk, Russia, pages 135–140, 1998.
- [62] J. M. Lighthill. On sound generated aerodynamically, part I. General theory. *Proceedings of the Royal Society A*, 211:564–587, 1952.
- [63] J. M. Lighthill. On sound generated aerodynamically, part II. Turbulence as a source of sound. *Proceedings of the Royal Society A*, 222:1–32, 1954.
- [64] F. Micaud. Vergleichende Untersuchungen an zwei verschiedenen Ausführungen von 2-dim. Ecken-Laval-Düsen für Ma 2.54 in Bezug auf Machzahl-Verteilung und vorhandene stationäre und instationäre Störfelder. Diplomarbeit, Institut Catholique des Arts et Métiers - IAG, Universität Stuttgart, 2001.
- [65] M. V. Morkovin. *Fluctuations and Hot-Wire Anemometry in Compressible Flows*. AGARDograph 24. NATO-AGARD, 1956.
- [66] M. V. Morkovin. On Transition Experiments at Moderate Supersonic Speeds. *Journal of the Aeronautical Sciences*, 24:480–486, 1957.
- [67] M. V. Morkovin. On Supersonic Wind Tunnels With Low Free-Stream Disturbances. *Journal of Applied Mechanics*, 26:319–323, 1959.
- [68] H. Motulsky. *Analysing Data with GraphPad Prism*. GraphPad Software, www.curvefit.com, 1999.
- [69] S. R. Pate and C. J. Schueler. Radiated Aerodynamic Noise Effects on Boundary-Layer Transition in Supersonic and Hypersonic Wind Tunnels. *AIAA Journal*, 7(3):450–457, 1969.

- [70] A. E. Perry and G. L. Morrison. A study of the constant-temperature hot-wire anemometer. *Journal of Fluid Mechanics*, 47(3):577–599, 1971.
- [71] A. E. Perry, A. J. Smits, and M. S. Chong. The effects of certain low frequency phenomena on the calibration of hot wires. *Journal of Fluid Mechanics*, 90(3):415–431, 1979.
- [72] O. M. Phillips. On the aerodynamic surface sound from a plane boundary layer. *Proceedings of the Royal Society A*, 234:327–335, 1956.
- [73] O. M. Phillips. On the generation of sound by a supersonic turbulent shear layer. *Journal of Fluid Mechanics*, 9:1–28, 1960.
- [74] T. Pleschinger. Vergleichende Untersuchungen an verschiedenen Sonden zur Bestimmung der Totaltemperatur in der Meßkammerströmung des großen Stoßwindkanals am IAG. Studienarbeit, IAG, Universität Stuttgart, 2001.
- [75] P. Profos and T. Pfeifer, editors. *Grundlagen der Meßtechnik*. Oldenbourg, 5 edition, 1997.
- [76] H. L. Reed, R. Kimmel, S. P. Schneider, and D. Arnal. Drag Prediction and Transition in Hypersonic Flow. In *Future Aerospace Technology in the Service of the Alliance*, volume 3 of *CP-600*. NATO AGARD, pages C15.1-C15.17, 1997.
- [77] E. Reshotko. A Program for Transition Research. *AIAA Journal*, 13(3):261–265, 1975.
- [78] R. Riedel. *Erprobung eines Stoßwindkanals zur Untersuchung des laminar-turbulenten Umschlags in Überschallgrenzschichten*. Dissertation, Institut für Aerodynamik und Gasdynamik, Universität Stuttgart, 2000.
- [79] G. Riegert. Untersuchung von Schallfeldern aus turbulenten Wandgrenzschichten und die Lokalisierung ihrer Entstehung in einer Modellmesskammer zum grossen Stoßwindkanal des IAG. Studienarbeit, IAG, Universität Stuttgart, 2000.
- [80] S. G. Saddoughi and S. V. Veeravalli. Hot-wire anemometry behaviour at very high frequencies. *Measurement Science and Technology*, 7:1297–1300, 1996.
- [81] G. R. Sarma. Automated constant voltage anemometer with *in situ* measurements of overheat and time constant of the hot-wire. *Review of Scientific Instruments*, 70(5):2384–2386, 1999.

- [82] G. R. Sarma, G. Comte-Bellot, and T. M. Faure. Software corrected hot wire thermal lag for the constant voltage anemometer featuring a constant bandwidth at the selected compensation setting. *Review of Scientific Instruments*, 69(9):3223–3231, 1998.
- [83] S. P. Schneider and C. E. Haven. Quiet-Flow Ludwieg Tube for High-Speed Transition Research. *AIAA Journal*, 33(4):688–693, 1995.
- [84] S.P. Schneider. Effects of High-Speed Tunnel Noise on Laminar-Turbulent Transition. *Journal of Spacecrafts and Rockets*, 38(3):323–333, 2001.
- [85] G. Schwarz. *Berechnung und Untersuchung von Eckenlavalldüsen mit gerader Unterschallkontur*. Dissertation, Institut für Aerodynamik und Gasdynamik, Universität Stuttgart, 1966.
- [86] A. J. Smits and J. P. Dussauge. Hot-Wire Anemometry in Supersonic Flows. In *A Survey of Measurements and Measuring Techniques in Rapidly Distorted Compressible Turbulent Boundary Layers*, AGARDograph 315, NATO AGARD, pages 5.1–5.14, 1989.
- [87] A. J. Smits, K. Hayakawa, and K. C. Muck. Constant Temperature Hot-Wire Anemometer Practice in Supersonic Flows. Part 1: The normal wire. *Experiments in Fluids*, 1:83–92, 1983.
- [88] A. J. Smits and K. C. Muck. Constant Temperature Hot-Wire Anemometer Practice in Supersonic Flows. Part 2: The inclined wire. *Experiments in Fluids*, 2:33–41, 1984.
- [89] A. J. Smits and A. E. Perry. The effect of varying resistance ratio on the behaviour of constant-temperature hot-wire anemometers. *Journal of Physics E: Scientific Instruments*, 13:451–456, 1980.
- [90] B. Smorodsky. Personal Communications, 2001.
- [91] Numerical Recipes Software. *Numerical Recipes in C: The Art of Scientific Computing*. Cambridge University Press, 1988-1992.
- [92] P. C. Stainback and K. A. Nagabushana. Review of Hot-Wire Anemometry Techniques and the Range of their Applicability. In *Thermal Anemometry*, volume 167 of *FED*, pages 93–133. ASME, 1993.

- [93] P. C. Stainback and R. D. Wagner. A Comparison of Disturbance Levels Measured in Hypersonic Tunnels Using a Hot-Wire Anemometer and a Pitot Pressure Probe. *AIAA Paper* 72-1003, 1972.
- [94] R. D. Wagner. Hot Wire Measurements of Freestream and Shock Layer Disturbances. *AIAA Journal*, 9(12):2468–2469, 1971.
- [95] S. Wagner. Strömungslehre. Skript für die Vorlesung Strömungslehre I+II. Universität Stuttgart, IAG, 3. Aufl., 1995.
- [96] S. Wagner, R. Wirtz, and R. Lösch. A Methodology for the Conceptual Aerodynamic Design of Transatmospheric Flight Vehicles. In *2nd International Conference on Aerospace Science & Technology, 6th Australian Aeronautical Conference*, volume I, pages 405–412, Melbourne, Australia, March 20–23 1995.
- [97] D. A. Walker, W. F. Ng, and M. D. Walker. Experimental Comparison of Two Hot-Wire Techniques in Supersonic Flows. *AIAA Journal*, 27(8):1074–1080, 1989.
- [98] D. A. Walker and M. D. Walker. Method for fast sine-wave calibration of hot-wire frequency response. *Review of Scientific Instruments*, 61(3):1131–1135, 1990.
- [99] J. H. Watmuff. An Investigation of the Constant-Temperature Hot-Wire Anemometer. *Experimental Thermal and Fluid Science*, 11:117–134, 1995.
- [100] P. D. Weidman and F. K. Browand. Analysis of a simple circuit for constant temperature anemometry. *Journal of Physics E: Scientific Instruments*, 8:553–560, 1975.
- [101] A. Weise and G. Schwarz. Der Stoßwindkanal des Instituts für Aerodynamik und Gasdynamik der Universität Stuttgart. *Zeitschrift für Flugwissenschaft*, 21(4):121–130, 1973.
- [102] J. Weiss, H. Knauss, and S. Wagner. Method for the determination of frequency response and signal to noise ratio for constant-temperature hot-wire anemometers. *Review of Scientific Instruments*, 72(3):1904–1909, 2001.
- [103] J. Weiss, A. D. Kosinov, H. Knauss, and S. Wagner. Constant temperature hot-wire measurements in a short duration supersonic wind tunnel. *The Aeronautical Journal*, 105(1050):435–441, 2001.

- [104] J. F. Wendt. External hypersonic aerodynamics: state-of-the-art and future perspective. In *Future Aerospace Technology in the Service of the Alliance*, volume 3 of *CP-600*. NATO AGARD, pages C10.1-C10.7, 1997.
- [105] S. W. D. Wolf and J. A. Laub. Characteristics of the NASA-Ames Laminar Flow Supersonic Wind Tunnel for Unique Mach 1.6 Transition Studies. In *Aerodynamics of Wind Tunnel Circuits and their Components*, AGARD CP-585, NATO AGARD, pages 30.1–30.16, 1997.
- [106] N. B. Wood. A method for determination and control of the frequency response of the constant-temperature hot-wire anemometer. *Journal of Fluid Mechanics*, 67(4):769–786, 1975.

Appendix A

Fluctuation diagram for uncorrelated modes

The analytic form of the fluctuation diagram for uncorrelated modes can easily be obtained using the separated contribution of the three basic modes: vorticity, sound waves and entropy spottiness. Since it is assumed that the correlation coefficient between the three modes is zero, the simple addition of the three contributions is allowed. Therefore, the fluctuation diagram form for the three separated modes, according to Kovásznyai [55], Morkovin [65], and Laufer [56], are briefly reviewed:

- vorticity mode:

$$\Theta = |\beta - r| \langle u_{rot} \rangle, \quad (\text{A.1})$$

- entropy mode:

$$\Theta = \left(1 - \frac{r}{\alpha}\right) \langle (T_0)_s \rangle, \quad (\text{A.2})$$

- acoustic mode:

$$\Theta = \left(\frac{1}{\gamma} \langle p \rangle - \langle u_{irr} \rangle\right) r + \alpha(\gamma - 1) \left(Ma^2 \langle u_{irr} \rangle - \frac{1}{\gamma} \langle p \rangle\right). \quad (\text{A.3})$$

Taking into account the source velocity \bar{u}_s defined by equation 3.9, this last equation can be rewritten in the following form:

$$\Theta = (L_1 r + L_2) \langle p \rangle, \quad (\text{A.4})$$

where

$$\begin{aligned} L_1 &= \frac{1}{\gamma} \left(1 - \frac{1}{M^2(1 - \bar{u}_s/\bar{u}_\infty)}\right), \\ L_2 &= \alpha \frac{\gamma - 1}{\gamma} \left(\frac{\bar{u}_s/\bar{u}_\infty}{1 - \bar{u}_s/\bar{u}_\infty}\right). \end{aligned} \quad (\text{A.5})$$

With the assumption of uncorrelated modes, the form of the fluctuation diagram is obtained by adding the square of the three contributions: $\Theta^2 = (\Theta^2)_{sound} + (\Theta^2)_{vorticity} + (\Theta^2)_{entropy}$, and yields:

$$\boxed{\Theta^2 = (L_1 r + L_2) \langle p \rangle^2 + (\beta - r)^2 \langle u_{rot} \rangle^2 + \left(1 + \frac{r}{\alpha}\right)^2 \langle (T_0)_s \rangle^2} . \quad (\text{A.6})$$

For $\overline{u_s} = 0$, this last form is equal to equation 87 of reference [55].

Appendix B

CTA DC analysis

A non linear static analysis of constant temperature hot-wire anemometers is necessary to determine the influence of the amplifier offset on the wire temperature, as explained in section 3.3.2. This analysis was already performed in 1971 by Perry & Morisson [70] for the case of a known offset voltage. Since the Cosystec CTA scanning system works with an offset current, a modification of Perry & Morisson's equations appeared to be necessary.

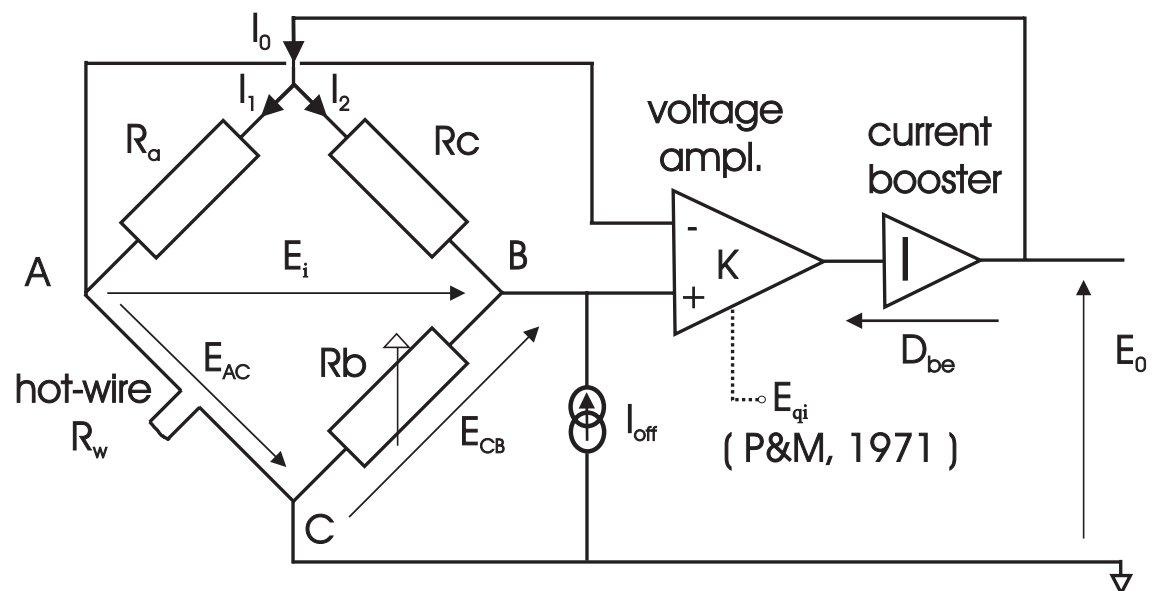


Figure B.1: CTA circuit with offset current

Figure B.1 shows a CTA circuit with offset current. The hot-wire (resistance R_w) is placed in the active arm of a Wheatstone bridge which diagonal voltage E_i is

amplified by a difference amplifier of DC gain K . The second amplifier stage is a classical power amplifier which deals as a current booster. It is modeled by a constant voltage drop D_{be} . The offset current I_{off} , which is necessary for a stable operation of the system, is injected through the lower passive arm of the bridge. In the analysis of Perry & Morisson, the offset current is replaced by an offset voltage E_{qi} injected in the feedback amplifier, and in this case the wire current I_1 is related to E_{qi} as follows [70]:

$$I_1 = \frac{K(R_b + R_c)}{(R_a + R_w)(R_b + R_c) + K\hat{R}} E_{qi}, \quad (\text{B.1})$$

where $\hat{R} = R_w R_c - R_a R_b$. In the present case, it is necessary to obtain a similar relation for an offset current.

Before proceeding further, let us define several convenient parameters:

$$\begin{aligned} \Pi &= (R_a + R_w)(R_c + R_b), \\ \Sigma &= R_a + R_b + R_c + R_w, \\ R_T &= \Pi/\Sigma, \end{aligned} \quad (\text{B.2})$$

where the parameter R_T is the total resistance of the wheatstone bridge.

The voltage E_0 at the top of the bride can be expressed as a function of I_1 : $E_0 = (R_w + R_a)I_1$, and of I_2 and I_{off} : $E_0 = R_c I_2 + R_b(I_2 + I_{off})$. Equating these two expressions, and taking into account that $I_0 = I_1 + I_2$ yields:

$$I_1 = \frac{R_c + R_b}{\Sigma} I_0 + \frac{R_b}{\Sigma} I_{off}. \quad (\text{B.3})$$

The total current I_0 is related to E_0 by Ohm's law : $I_0 = E_0/R_T$. Taking the two amplifier stages into account yields :

$$I_0 = \frac{K E_i}{R_T} - \frac{D_{be}}{R_T}. \quad (\text{B.4})$$

The next step is to relate E_i to I_0 in another way. Considering the lower bridge diagonal, one can write

$$E_i = E_{AC} + E_{CB}, \quad (\text{B.5})$$

where

$$E_{AC} = -\frac{R_w}{R_a + R_w} E_0. \quad (\text{B.6})$$

E_{CB} can be computed by applying the electrical superposition theorem on the bridge's right arm:

$$E_{CB} = \frac{R_b}{R_b + R_c} E_0 + \frac{R_b R_c}{R_b + R_c} I_{off}. \quad (\text{B.7})$$

Injecting B.7 and B.6 into B.5, and recalling that $I_0 = E_0/R_T$ yields:

$$E_i = -\frac{\hat{R}}{\Sigma R} I_0 + \frac{R_b R_c}{R_b + R_c} I_{off}. \quad (\text{B.8})$$

Injecting B.8 in B.4, and the corresponding result in B.3 yields after a little algebra:

$$I_1 = \underbrace{\frac{K R_b R_c}{\Pi + K \hat{R}} I_{off}}_A - \underbrace{\frac{R_b + R_c}{\Pi + K \hat{R}} D_{be}}_B + \underbrace{\frac{R_b}{\Sigma}}_C. \quad (\text{B.9})$$

For the present anemometer, if the following orders of magnitude are considered:

$$\begin{aligned} K &= 1.8 \cdot 10^6, \\ D_{be} &\simeq 0.7V, \\ 2.9 \cdot 10^{-5} A &\leq I_{off} \leq 7.5 \cdot 10^{-4} A, \\ R_a &= 50\Omega, R_c = 500\Omega, R_w \sim 5\Omega, R_b \sim 50\Omega, \end{aligned} \quad (\text{B.10})$$

the terms B and C in equation B.9 vanish ($B \ll A$ and $C \ll A$) and B.9 simplifies to:

$$\boxed{I_1 \simeq \frac{K R_b R_c}{\Pi + K \hat{R}} I_{off}}. \quad (\text{B.11})$$

It follows that the expression of I_1 for a bridge with offset current is the same as for an offset voltage if E_{qi} in expression B.1 is replaced by:

$$E_{qi} = \frac{R_b R_c}{R_b + R_c} I_{off}. \quad (\text{B.12})$$

In other words, the equivalent offset voltage is equal to the voltage drop produced by the offset current flowing through the two resistances of the bridge's passive arm placed in parallel. For the Cosytec scanning system, a typical value of the offset current ($I_{off} \sim 0.2mA$) would correspond to an offset voltage of $E_{qi} \sim 10mV$.